POLYMER ELECTROLYTE MEMBRANE FUEL CELLS OPERATING UNDER ULTRA-LOW STOICHIOMETRIC ANODE FLOW CONDITIONS

BY

MURAT GÖKHAN ESKİN

IN
PARTIAL FULFILLMENT OF
THE REQUIREMENTS FOR THE DEGREE
OF
DOCTOR OF PHILOSOPHY

SABANCI UNIVERSITY

SPRING 2018

POLYMER ELECTROLYTE MEMBRANE FUEL CELLS OPERATING UNDER ULTRA-LOW STOICHIOMETRIC ANODE FLOW CONDITIONS

APPROVED BY:

Prof. Dr. Serhat Yeşilyurt
(Dissertation Supervisor) .....

Prof. Dr. Selmiye Alkan Gürsel .....

Asst. Prof. Dr. Tuğçe Yüksel .....

Assoc. Prof. Dr. Osman Öztürk .....

Prof. Dr. İlker Tarı .....

DATE OF APPROVAL: 27/07/2018

© Murat Gökhan Eskin 2018

All Rights Reserved

ABSTRACT

POLYMER ELECTROLYTE MEMBRANE FUEL CELLS OPERATING UNDER ULTRA-LOW STOICHIOMETRIC ANODE FLOW CONDITIONS

Murat Gökhan Eskin

PhD Dissertation, July 2018

Supervisor: Prof. Dr. Serhat Yeşilyurt

Keywords: Polymer electrolyte membrane fuel cells, dead-ended anode, ultra-low flow, accelerated stress test, carbon corrosion, hydrogen utilization

The polymer electrolyte membrane fuel cell is a system that converts chemical energy of hydrogen directly into electrical energy. 2020 targets set by the U.S. Department of Energy for light duty vehicles are already accomplished except for the cost, durability and efficiency.

The efficiency can be improved by turning off the anode exit of the fuel cell (dead-ended anode mode) and forcing all the hydrogen to move to the cathode. Even though this maximizes the hydrogen utilization and the efficiency, the accumulated water and nitrogen causes local fuel starvation which leads to irreversible carbon support degradation and performance loss. One way to overcome this issue is to allow a very small amount of continuous purging in the anode (ultra-low flow mode) which helps evacuation of the accumulated water and nitrogen.

In this thesis, the effect of dead-ended anode and ultra-low flow modes on the performance loss was evaluated for two different types of samples. It was shown that the ultra-low flow mode damaged two times less than the dead-ended anode mode while yielding a 99.93 % hydrogen utilization.

However, the amount of carbon corrosion is still more than the normal operation mode for a commercial sample. To improve the durability, research on new materials is necessary. An accelerated stress test designed specially to promote carbon corrosion was proposed so that novel materials can be evaluated for their performance against carbon corrosion under real operation conditions quickly and easily. To be able to realize such kind of a procedure, a high precision flow control set up that can maintain ultra-low flows was designed.

ÖZET

ÇOK DÜŞÜK STOKİYOMETRİK ANOT AKIŞI KOŞULLARINDA ÇALIŞAN POLİMER ELEKTROLİT MEMBRANLI YAKIT PİLLERİ

Murat Gökhan Eskin

Doktora Tezi, Temmuz 2018

Tez Danışmanı: Prof. Dr. Serhat Yeşilyurt

Anahtar Kelimeler: Polimer elektrolit membranlı yakıt pilleri, anot çıkışı kapalı, çok düşük akış, hızlandırılmış stress testi, karbon korozyonu, hidrojen verimi

Polimer elektrolit membranlı yakıt pili hidrojendeki kimyasal enerjiyi direct olarak elektrik enerjisine çeviren bir sistemdir. Amerika Enerji Departmanı tarafından binek otomobiller için belirlenen 2020 hedeflerine, maliyet, dayanıklılık ve verim başlıkları dışında ulaşılmıştır.

Yakıt pilinin anot çıkışı kapatılarak (anot çıkışı kapalı) tüm hidrojenin katot tarafına geçmeye zorlanması sonucu verimliliğin arttırılması mümkündür. Bu durum hidrojen kullanım yüzdesini ve verimini arttırsa da, anot çıkışında biriken su ve azot bu bölgede local hidrojen yoksunluğuna ve akabinde karbon destek malzemesinin geri dönüştürülemez bir şekilde aşınmasına ve performans kaybına sebep olmaktadır. Bu olumsuzluğun giderilmesinin yollarından birisi anot çıkışının çok düşük akışlarda (çok düşük stokiyometrik anot akışı) sürekli olaral tasfiye edilmesidir. Bu tasfiye sonucu anot çıkışında biirken su ve azot tahliye edilebilmektedir.

Bu tez çalışmasında, anot çıkışı kapalı ve çok düşük stokiyometrik akış koşullarının performans kaybına olan etkileri 2 farklı numune üzerinde çalışılmıştır. Çok düşük stokiyometrik akış koşullarının anot çıkışı kapalı çalışma koşuluna göre iki kat daha az aşındırmaya sebep olduğu, buna ragmen hidrojen kullanım oranının % 99.93 olarak kaldığı gösterilmiştir.

Karbon korozyon miktarı, standard bir malzeme için hala normal çalışma koşullarına (anot çıkışı açık) göre daha fazladır. Dayanıklılığı arttırmak için yeni malzemeler araştırılmalıdır. Bu yeni malzemelerin gerçek çalışma koşulları altında karbon korozyonuna dayanıklılığını hızlı ve kolay bir şekilde test edebilmek için karbon korozyonunu öne çıkaran bir hızlandırılmış stress testi dizayn edilmiştir. Dizayn edilen bu testi gerçekleştirebilmek için çok düşük akışları yüksek hassasiyette control edebilecek bir system geliştirilmiştir.

ACKNOWLEDGEMENTS

I would like to express my gratitude to Prof. Serhat Yeşilyurt, my advisor, for giving me the opportunity to study on fuel cells. His never-ending patience and fatherly attitude will always be remembered.

I wish to extend my thanks to all of my current and former friends end colleagues; Osman, Alperen, Abdullah, Ebru, Hakan, Ali and Omid. I could not imagine a lab without them. I also thank our lab hero İlker Abi for his instant help whenever I needed, Serkan and İlker for making it possible for me to perform overnight experiments.

I would like to thank TUBITAK, The Scientific and Technological Research Council of Turkey for the financial support.

Finally, I would like to extend my sincere thanks to my wife, Elif for bearing with me and supporting me throughout the whole process and my son for helping me type whenever he saw me working in front of the computer. I also wish to thank my parents, Arife and Fehmi and my sister, Nagihan for their infinite love and support, and my parents-in-law, Ayşegül and Süleyman for their helps and support.

TABLE OF CONTENTS

1 Introduction 5
1.1 The Proton Exchange Membrane Fuel Cell 5
1.2 The Future of Fuel Cells 6
1.3 Challenges 9
1.4 Department of Energy Targets 9
1.5 Thesis Objective 10
2 Theoretical Background 13
2.1 Electrochemical Thermodynamics 13
2.1.1 Theoretical Open Circuit Voltage 13
2.1.2 Polarization Curves 14
2.2 Fuel Cell Components 16
2.2.1 Proton Exchange Membrane: 16
2.2.2 Gas Diffusion Layer: 17
2.2.3 Catalyst Layer: 18
2.3 Calculation for Mass Flow Rate 19
2.4 Cyclic Voltammetry 20
2.5 Degradation Mechanisms 25
2.6 Carbon Corrosion 27
2.6 Accelerated Stress Tests in Literature 31
3 Experimental Methods 38
3.1 The Overall Setup 38
3.2 Flow Control Setup 41
3.3 MEA preparation 44
3.3.1 Catalyst Ink Preparation 44
3.3.2 Coating the Catalyst on Gas Diffusion Layer 44
3.3.3 Hot-pressing the 7-layer MEA 45
3.4 Operation procedure 46
3.4.1 Linear Sweep Voltammetry 46
3.4.2 MEA Conditioning 48
3.4.3 Performance Tests 49
3.4.4 Cyclic Voltammetry and ECSA Calculation 49
4 Results and Discussion 52

4.1 A Novel Accelerated Stress Test for Carbon Corrosion 52
4.1.1 Ideal Flow Rate for ULF Mode 52
4.1.2 Different Load Cycle Profiles Under ULF mode 55
4.1.3 Post-Mortem Analysis of the MEA under SEM 68
4.1.4 Discussion 74
4.2 Effect of Ultra-Low Flow Operation to MEA Durability 75
4.2.1 100 hours of Flow-through, Ultra-low Flow and Dead-ended Operation for MEA with Commercial Catalyst Support 75
4.2.2 72 hours of Flow-through, Ultra-low Flow and Dead-ended Operation for MEA with Carbon Fiber Catalyst Support 78
4.2.3 Discussions 80
5 CONCLUSION 81
6 Future Work 83
7 APPENDIX 84
7.1 The program uploaded to the syringe pump 84
7.2 The program uploaded to the Arduino 85
8 REFERENCES 86

LIST OF FIGURES

Figure 1.1: Proton exchange membrane fuel cell schematic 5
Figure 1.2: Calculated mass of vehicles using battery or fuel cell technology as a function of their range [1] 7
Figure 1.3: Estimated well-to-wheels greenhouse gas emissions as a function of vehicle range for the average US marginal grid mix in the 2010–2020 time period [1] 8
Figure 1.4: DOE targets and the current status (in green) 10
Figure 1.5: Flow paths for a) Flow-through, b) Dead-ended anode, c) Ultra-low flow modes of operation 11
Figure 2.1: A representative fuel cell I-V curve 14
Figure 2.2: Chemical structure of the Nafion™ ionomer 17
Figure 2.3: The scanning electron microscope image of the micro-porous carbon particles of a GDL used in this thesis 18
Figure 2.4: The representation (left) and the transmission electron microscope image (right) [9] of the catalyst layer 19
Figure 2.5: Cyclic Voltammogram of Pt-black/Nafion electrode [10] 21
Figure 2.6: Cyclic Voltammogram of Pt-black/Nafion electrode with marked regions 22
Figure 2.7: Cyclic Voltammogram of Pt-black/Nafion electrode with redox processes shown 24
Figure 2.8: The charge density region (shaded area) for ECSA calculation [12] 25
Figure 2.9: Representation image of catalyst degradation mechanisms [18] 27
Figure 2.10: Potential distributions during the reverse current conditions where Vma is the anode metal potential, Vmc is the cathode metal potential, Φ is the electrolyte potential [31]. 30
Figure 3.1: PEMFC test setup 38
Figure 3.2: Fuel cell test station (left) and the back-pressure unit (right) 39
Figure 3.3: A model NE-500 syringe pump 40
Figure 3.4: a) Syringe pump with the heating cuffs on the syringe, b) syringe pump with heating connections, c) Arduino controller connected to the syringe pump 41
Figure 3.5: Syringe pump control interface 42
Figure 3.6: Arduino pins used for voltage reading and TTL signal generation 43
Figure 3.7: The MEA preparation procedure 45
Figure 3.8: Overall uncompressed MEA thickness 46
Figure 3.9: Linear sweep voltammogram for hydrogen crossover in our PEMFC 46
Figure 3.10: MEA break-in voltage cycling profile 48
Figure 3.11: Cyclic voltammogram of a 25 cm^2 active area MEA in Gamry's original software 50
Figure 4.1: a) Bipolar plates and b) MEA for the 25 cm^2 cell 52
Figure 4.2: I-V curves taken at different temperatures 53
Figure 4.3: Voltage transient for the DEA operation for a 25 cm^2 cell 53
Figure 4.4: Voltage transient for the 25 cm^2 cell under DEA with ULF mode 54
Figure 4.5: Power density (mW/cm^2) vs current (A) curve for a fresh 25 cm^2 MEA 55
Figure 4.6: Summary of all the cycle profiles applied 56
Figure 4.7: Current vs time plot for the cycle profile 1 57

Figure 4.8: Part of the voltage transient during operation under cycle profile 1 58
Figure 4.9: Comparison of the cyclic voltammograms for the fresh MEA and 240 h of operation under cycle profile 1 58
Figure 4.10: Part of the voltage transient during operation under cycle profile 2 59
Figure 4.11: Comparison of the cyclic voltammograms for the fresh MEA, 240 h of operation under cycle profile 1 and 96 h of operation under cycle profile 2 60
Figure 4.12: Last 10 hours of the voltage transient during operation under cycle profile 3 61
Figure 4.13: Comparison of the cyclic voltammograms for the fresh MEA, 240 h of operation under cycle profile 1, 96 h of operation under cycle profile 2 and 48 h of operation under cycle profile 3 61
Figure 4.14: 32 hours of the voltage transient during operation under cycle profile 4 62
Figure 4.15: Comparison of the cyclic voltammograms for the fresh MEA, 240 h of operation under cycle profile 1, 96 h of operation under cycle profile 2, 48 h of operation under cycle profile 3 and 32 h of operation under cycle profile 4 63
Figure 4.16: First 60 hours of the voltage transient during operation under cycle profile 5 64
Figure 4.17: Last 10 hours of the voltage transient during operation under cycle profile 5 65
Figure 4.18: Comparison of the cyclic voltammograms for the fresh MEA, 240 h of operation under cycle profile 1, 96 h of operation under cycle profile 2, 48 h of operation under cycle profile 3, 32 h of operation under cycle profile 4 and 70 h of operation under cycle profile 5 65
Figure 4.19: 18 hours of the voltage transient during operation under cycle profile 6 66
Figure 4.20: Comparison of the cyclic voltammograms for the fresh MEA, 240 h of operation under cycle profile 1, 96 h of operation under cycle profile 2, 48 h of operation under cycle profile 3, 32 h of operation under cycle profile 4, 70 h of operation under cycle profile 5 and 18 h of operation under cycle profile 6 67
Figure 4.21: Time evolution of the ECSA loss after each cycle profile 68
Figure 4.22: Dissection plan and analyzed sections (in green) of the MEA for SEM analysis 69
Figure 4.23: SEM images of the dissected MEA after carbon corrosion study. a) section number 1, b) section number 7, c) section number 10, d) section number 12, e) section number 15, f) section number 17, g) section number 22, h) section number 23 73
Figure 4.24: First 10 hours of the FT mode for the commercial 8.17 cm^2 MEA 76
Figure 4.25: First 10 hours of the ULF mode for the commercial 8.17 cm^2 MEA 76
Figure 4.26: First 10 hours of the DEA mode for the 8.17 cm^2 MEA with commercial catalyst support..... 77
Figure 4.27: Cyclic voltammograms after 100 hours of FT, ULF and DEA operation for the 8.17 cm^2 MEA with commercial catalyst support..... 77
Figure 4.28: I-V curves taken after each modes of operation for the 8.17 cm^2 MEA with commercial catalyst support 78
Figure 4.29: Cyclic voltammograms after 72 hours of FT, ULF and DEA operation for the 8.17 cm^2 MEA with carbon fiber carbon support 79
Figure 4.30: I-V curves taken after each modes of operation for the 8.17 cm^2 MEA with carbon fiber carbon support 80

1 INTRODUCTION

1.1 The Proton Exchange Membrane Fuel Cell

A fuel cell is a type of battery that converts chemical energy directly to electricity. However, unlike a normal battery, fuel cell should be fed with fuel and oxidant for this electrochemical process. Characterized by their electrolyte type, there are five main types of fuel cells: alkaline; phosphoric acid, molten carbonate, solid oxide and proton exchange membrane fuel cells. Among these, the proton exchange membrane or polymer electrolyte membrane fuel cells (PEMFC) have the advantage of low operating temperature, no toxic emissions and easier manufacturing.

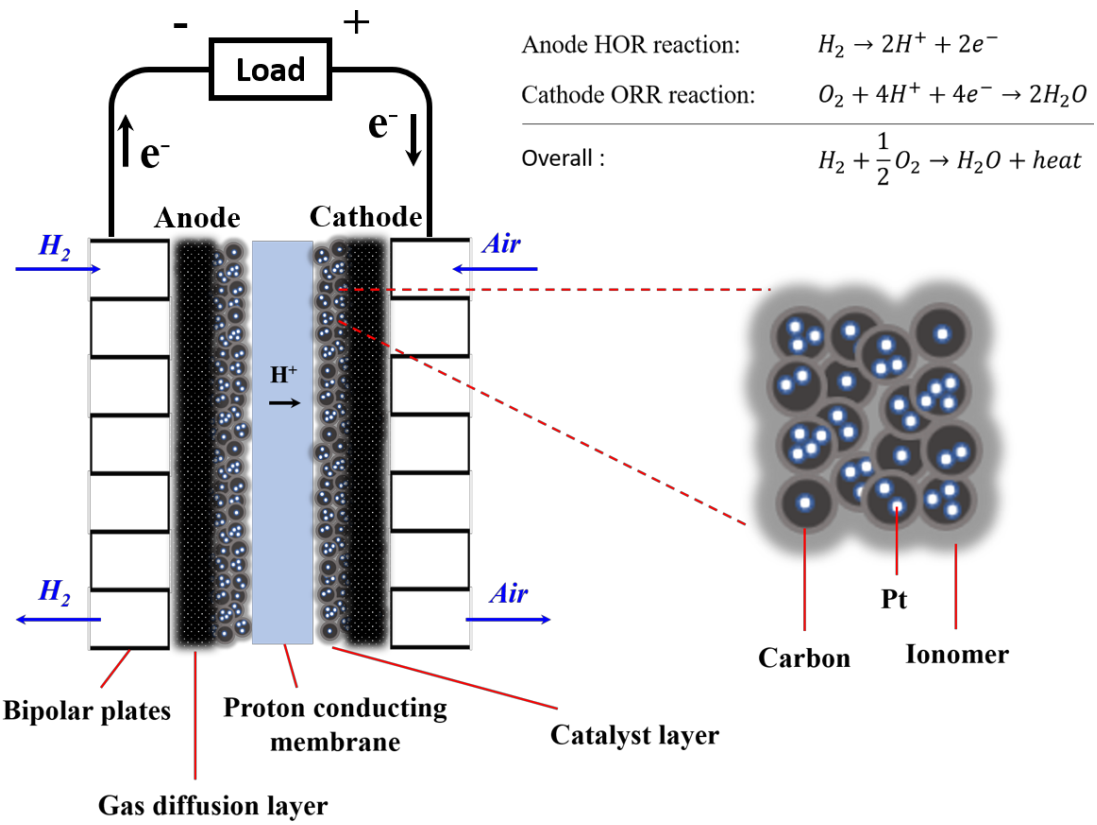

Figure 1.1: Proton exchange membrane fuel cell schematic

The cross-sectional schematic of a single PEMFC is shown in *Figure 1.1*. Gas diffusion layers, catalyst layers and the membrane compose the membrane-electrode-assembly (MEA). The fuel (hydrogen) is fed into the anode inlet whereas the oxidant (oxygen) is fed into the cathode inlet in the form of air or as pure oxygen. While the fuel and the oxidant flow through graphite bipolar plates, they penetrate into gas diffusion layers and reach the catalyst layer surface. When the hydrogen hits the catalytic Pt particles, the electrons of hydrogen are stripped off which is called the hydrogen oxidation reaction (HOR). The resulting protons (H^+) are conducted to the cathode side through the proton exchange membrane whereas the electrons (e^-) arrive at the cathode by flowing through an external load. This flow of electrons forms the electrical current. The same catalyst particles help the oxygen combine with these protons and electrons to form water and heat.

1.2 The Future of Fuel Cells

Hydrogen is the most abundant element that can be found in nature. One of the biggest advantages of the fuel cells come from hydrogen's superior energy density compared to lithium ion batteries. The second vital advantage is the clean byproduct of the fuel cells which is water. As a result, the fuel cells are promising candidates for being the future energy systems in the world.

Thomas (2009) reported the calculated vehicle masses if they were using lead-acid (PbA) battery, nickel metal hydride (NiMH) battery, lithium ion battery (Li-ion) and fuel cell as a function of the ranges they can cover (Figure 1.2). According to this data, to be able to cover a range of 100 miles, the total mass of a PbA battery car should be 3000 kg, a NiMH battery car should be 1750 kg, a Li-ion battery car should be 1400 kg and a fuel cell car should be 1200 kg. If this range is 300 miles which is a more realistic target, the mass of the Li-ion car should be 2300 kg whereas the fuel cell car should be 1200 kg. The PbA and NiMH battery cars are not even feasible. The extra mass needed to increase the range of a fuel cell vehicle is small, since only the volume of the hydrogen storage tank should be increased. Thus, battery electric vehicles will be much heavier than the fuel cell vehicles for the same driving range.

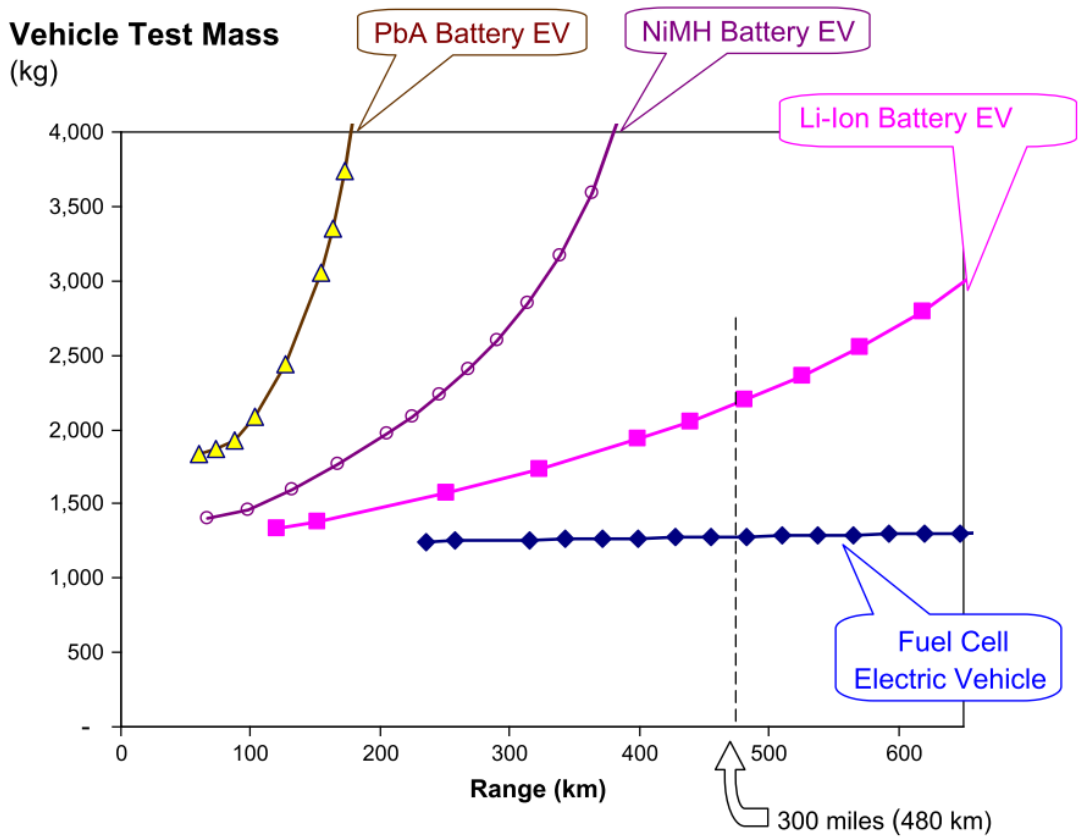

Figure 1.2: Calculated mass of vehicles using battery or fuel cell technology as a function of their range [1]

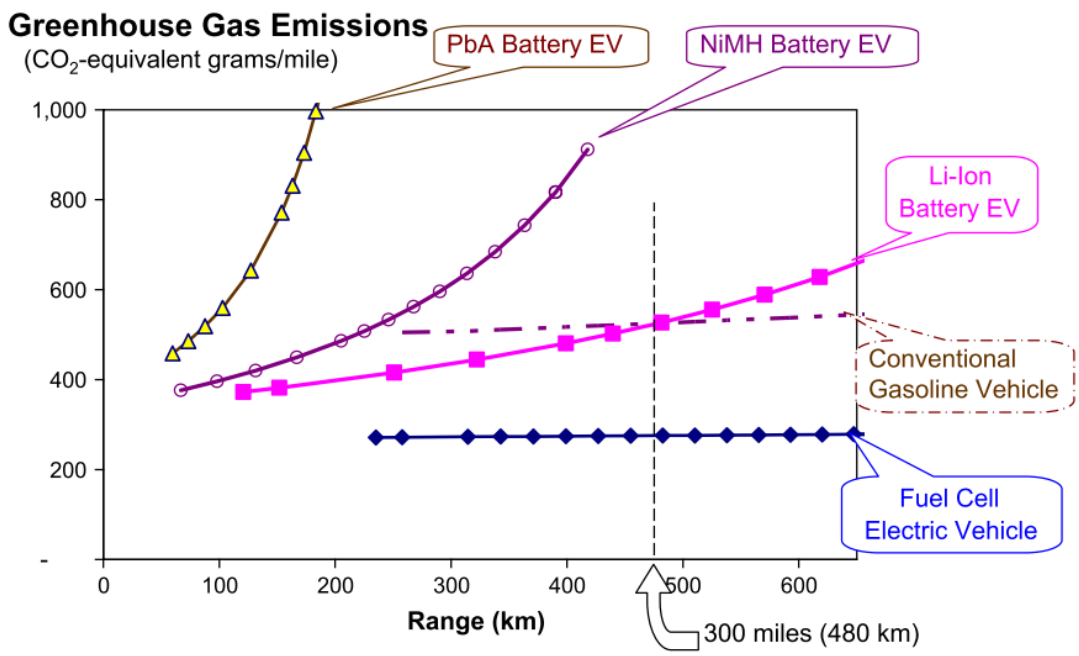

Figure 1.3: Estimated well-to-wheels greenhouse gas emissions as a function of vehicle range for the average US marginal grid mix in the 2010–2020 time period [1]

In the same paper, the estimated greenhouse gas emissions of the current energy systems were compared assuming that all the hydrogen is produced form natural gas (Figure 1.3). There are cleaner processes to produce hydrogen such as splitting water by using renewable energy sources. Still, this graph confirms that the fuel cell technology can be a better energy system for a clean environment.

The fuel cell technology is already being used in cars, busses, forklift trucks, submarines and even drones. Longer operating time per storage, better range, fast fueling, quiet operation and low thermal signature are some of the advantages that makes fuel cells attractive systems to use in these products.

Safety concerns due to the highly volatile and buoyant nature of hydrogen, cost and infrastructure are some issues that discourage a broader use of fuel cells. Toyota announced [2] that they started to use a new technology for their hydrogen tanks. They report that winding the tank with carbon fiber reinforced plastic improves the durability of the tank so that it can survive serious crashes. They also claim that the new system is leakage proof and to demonstrate, they fire a bullet to the hydrogen filled tank. The tank was punctured but did not explode, the hydrogen quickly escaped without flaming.

The cost and the lack of the infrastructure seems to be the biggest disadvantages of the current fuel cell technology. However, the current advances in catalyst research and initiatives to increase the number of hydrogen stations can pave the way for a widely adopted fuel cell technology.

1.3 Challenges

Three serious challenges for the PEMFC technology are the cost, efficiency and durability, all of which are closely related. The cost is high because Pt is the best catalyst so far, but it is also expensive. Decreasing the amount of Pt used or using Pt-free catalysts can lead to efficiency and durability issues because the use of less or cheaper materials may not catalyze the electrochemical reactions as good as Pt. Likewise, the current systems need to have feedback mechanisms to use the wasted hydrogen and this makes the system more expensive and complex. There are some cheaper systems that involves closing the anode exit of the fuel cell and force all the hydrogen to diffuse into the cathode and increase the efficiency. However, this time the catalyst layer suffers from corrosion which affects the durability. Finally, due to the harsh operation conditions, the fuel cell may experience reversible and irreversible damages.

1.4 Department of Energy Targets

U.S. Department of Energy (DOE) has set some targets for the year 2020 for the commercialization of fuel cells. In 2017, they updated these targets as a result of recent advances in fuel cell technology. Figure 1.4 shows the DOE targets for light-duty vehicles and how much of it is succeeded for each item.

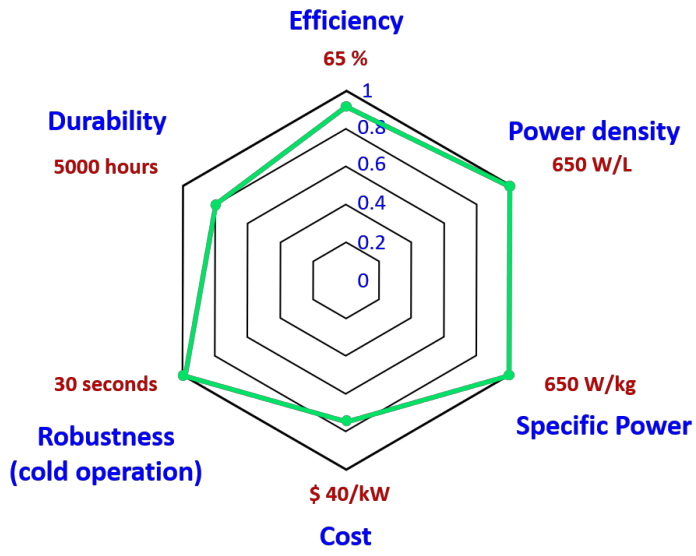

Figure 1.4: DOE targets and the current status (in green)

Apparently, cost, durability and efficiency are still the most important topics for the fuel cell research. Among them, increasing the efficiency by maximizing the hydrogen utilization is the scope of this thesis.

1.5 Thesis Objective

The usual operation mode of a fuel cell is the flow-through operation. In flow-through (FT) mode (Figure 1.5, a) the anode exit of the fuel cell is directly connected to the exit hose which leads to the back-pressure unit. In this mode, the nitrogen and water vapor which diffuse from the cathode to the anode and unused hydrogen flows through the exit hose and reach the back-pressure unit.

The wasted hydrogen decreases the efficiency by decreasing the hydrogen utilization. One way to prevent this is to use recovery systems that enables reusing the waste hydrogen. However, this makes the overall system bulkier and more complex. Another way to accomplish a high hydrogen utilization is to run the fuel cell in dead-ended anode mode.

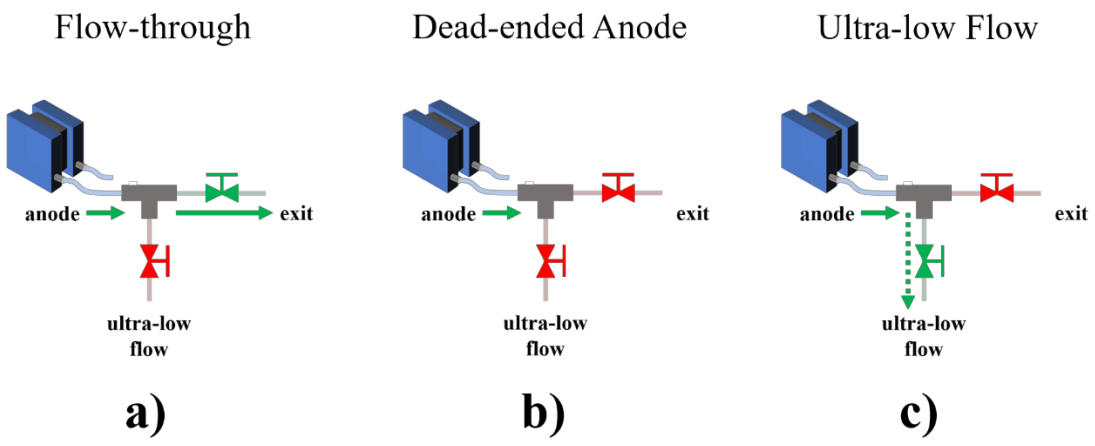

Figure 1.5: Flow paths for a) Flow-through, b) Dead-ended anode, c) Ultra-low flow modes of operation

In dead-ended anode (DEA) mode (Figure 1.5, b), the anode exit of the fuel cell is a dead-end. The nitrogen and water vapor cannot be purged and accumulates in the flow channels. The unused hydrogen has nowhere to escape and flows to the cathode. As a result, the cell is forced to use all the hydrogen in this mode. However, due to the accumulated water and nitrogen in the anode, some part of the flow channels is blocked. Hydrogen cannot reach this blocked region which stops the proton transport from anode to the cathode. As a result, the cathode side of this region suffers from local fuel starvation which leads to carbon corrosion.

The irreversible damage caused by these harsh operating conditions lead to the loss of mass transport, loss of electrode connectivity, and loss of electrochemically active area by catalyst detachment. In the end, the fuel cell suffers from considerable performance loss and decreased lifetime. Therefore, research for more durable materials is necessary. However, testing them against carbon corrosion in real life operating conditions can be time consuming and expensive. In the first part of this thesis, a new accelerated stress test protocol that promotes a fast carbon corrosion in realistic operating conditions is proposed.

Furthermore, the effect of ultra-low flow (ULF) mode against carbon corrosion is studied and compared to that of DEA mode. In the ULF mode, a very small amount of flow is allowed to evacuate the accumulated water vapor and nitrogen (Figure 1.5, c). Evacuation of the water vapor and nitrogen prevents the local fuel starvation from happening in the

cathode, decreasing the amount of corrosion. In the second part of the thesis, the amount of damage induced by FT, ULF and DEA modes of operation were analyzed and compared to show that the ultra-low-flow mode causes less damage to the cell while maximizing the hydrogen utilization as in the dead-ended-anode mode.

2 THEORETICAL BACKGROUND

2.1 Electrochemical Thermodynamics

2.1.1 Theoretical Open Circuit Voltage

The theoretical cell voltage for the H_2/O_2 cell can be calculated via the Gibbs free energy ΔG° [3]:

$$E^{0,} = -\frac{\Delta G^{\circ}}{nF} \tag{2.1}$$

where n is the number of electrons produced per hydrogen, F is the Faraday's constant (96,485 Coulombs/electron mol) and ΔG° for water vapor is given as follows [4] :

$$\Delta G^{\circ} = -240{,}203 + 3.933\,T\,\ln T + 0.0069\,T^2 - 1.54808\,10^{-6}\,T^3 + 16.40\,T \tag{2.2}$$

where T is the temperature. The calculated theoretical fuel cell potential of H_2/O_2 at 25 ℃ is 1.23 V.

This value is valid at atmospheric pressure. To calculate the theoretical value at non-standard conditions (different partial pressures/different concentrations), the following Nernst equation is used [3][5]:

$$E = E^{0,} + \frac{RT}{nF}\ln\frac{(p_{H_2})(p_{O_2})^{0.5}}{(p_{H_2O})} \tag{2.3}$$

where E is the theoretical cell potential at non-standard conditions, $E^{0,}$ is the theoretical cell potential at standard conditions (formal potential), R is the ideal gas constant, T is the temperature, n is the number of electrons produced per reaction, F is the Faraday's constant, p_{H_2}, p_{O_2} and p_{H_2O} are the partial pressures of the corresponding gases.

2.1.2 Polarization Curves

When an external load is connected to the fuel cell, some net current flows through this load. This net current is divided by the active area to find the current density. The voltage-current density relationship is a representative of the fuel cell performance which is also called an I-V curve or a polarization curve. An I-V curve is usually obtained by scanning the voltage and measuring the resulting current or scanning the current and measuring the output voltage.

Ideally, the I-V curve should be somewhat a linear line at 1.23 V vs the current density. However, due to the kinetic, ohmic and mass transport limitations that causes irreversible voltage loses [3], the real polarization curves look like the one shown in Figure 2.1.

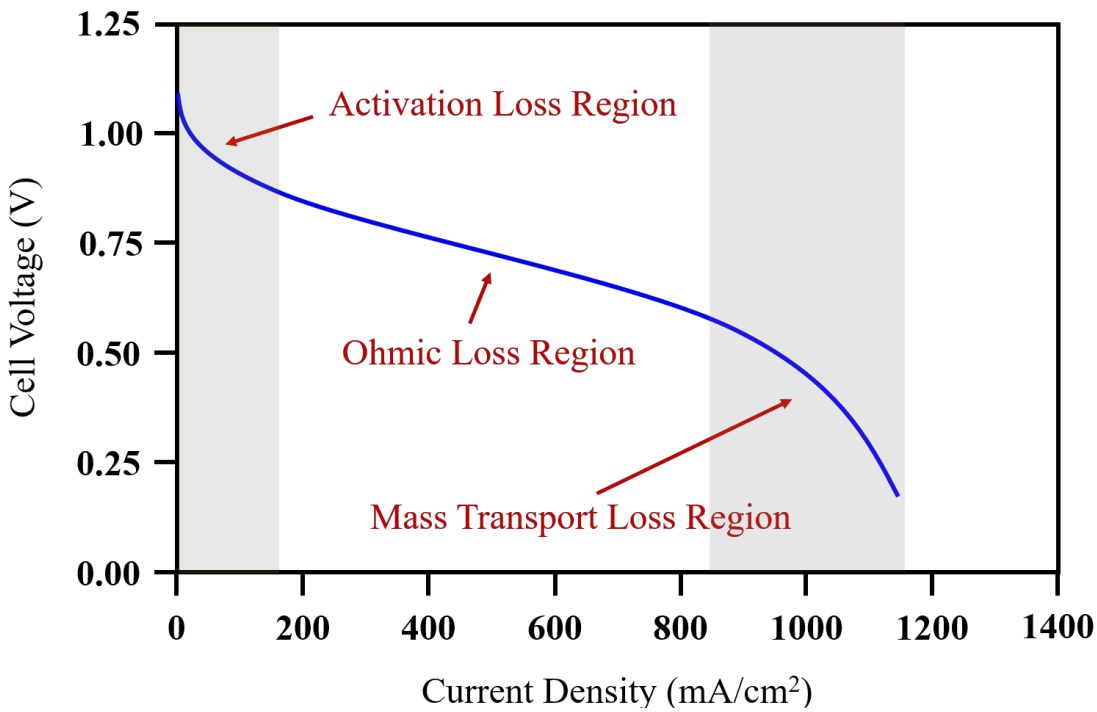

Figure 2.1: A representative fuel cell I-V curve

The first deviation from the ideal/theoretical voltage originates from the fuel crossover and internal losses such as electronic conduction through the electrolyte together with the

electrode material and catalyst oxidation at the cathode. As a result, the polarization curve does not start from 1.23 V (open circuit voltage).

The activation loss is due to the voltage needed to overcome the energy barrier to the electrochemical reaction. Tafel equation predicts the activation loss (ΔV_{act}) in a simple and purely empirical way as follows [3]:

$$\Delta V_{act} = a + b \log i \tag{2.4}$$

where $a = 2.3 \frac{RT}{\alpha_c F} \log i_0$ being the kinetic parameter and $b = 2.3 \frac{RT}{\alpha_c F}$ being the Tafel slope.

The current density, i mentioned above is given by the Butler-Volmer equation:

$$i = i_0 \left(exp\left(\frac{\alpha_a \Delta V\, F}{RT}\right) - exp\left(\frac{\alpha_c \Delta V\, F}{RT}\right)\right) \tag{2.5}$$

where i_0 is the exchange current density, ΔV is the overpotential ($E - E_{theor}$), α_a and α_c are the anodic and cathodic transfer coefficients respectively. The activation polarization is cathode-dominated because of the sluggish oxygen reduction reaction of the cathode. The exchange current density for the oxygen reduction is ca. 1000 times less than the hydrogen oxidation on the anode side.

The performance loss due to the ohmic limitations is caused by the resistance to ionic current through the electrolyte, electronic current through the electrodes and the contact resistance. The pseudo-linear portion of the polarization curve forms the ohmic loss region (Figure 2.1).

$$\Delta V_{ohm} = i\, R_{ohm} \tag{2.6}$$

As the equation 2.6 suggests, the total voltage drop due to ohmic loss increases as the current drawn increases. The value for R_{ohm} can be estimated by taking the high frequency intercept of the x axis on the Nyquist plot which is acquired by the impedance spectroscopy.

The loss caused by the mass transport limitations occurs because of the concentration gradient that develops when the electrode reaction rate exceeds the rate at which the reactant can be supplied. The speed that the reactant is delivered to the reaction site limits the reaction rate and this speed is limited by the transport mechanism of the gas in the gas diffusion layer and electrolyte. The transport mechanism includes convection, diffusion and migration of the products such as hydrogen, oxygen, protons and water, into and out of the catalyst sites [6]. The voltage loss (ΔV_{conc}) due to the concentration polarization is described by:

$$\Delta V_{conc} = 2.3\frac{RT}{nF}\log\left(\frac{i_{im}}{i_{lim} - i}\right) \tag{2.7}$$

where i_{im} is the transport limiting current density. It is the current density at which the amount of reactant consumed is equal to that of the diffused and reached the catalyst surface. This type of loss shows itself at higher current portion of the I-V curve (Figure 2.1).

2.2 Fuel Cell Components

2.2.1 Proton Exchange Membrane:

The polymer electrolyte membrane (PEM) is the ionic conductor between the electrodes. It also separates the anode and cathode so that there is no direct recombination of the fuel with the oxidant. Furthermore, PEM serves as an electronic insulator between the electrodes.

Perfluorosulfonic acid (PFSA) membranes, also known as the Nafion® membranes are widely used in PEMFCs. As seen in Figure 2.2, the fluoropolymer backbone of $-(CF_2)_n-$ groups in the Nafion structure provides the mechanical stability and the sulfonic acid ($-SO_3H-$) groups enable the proton conduction.

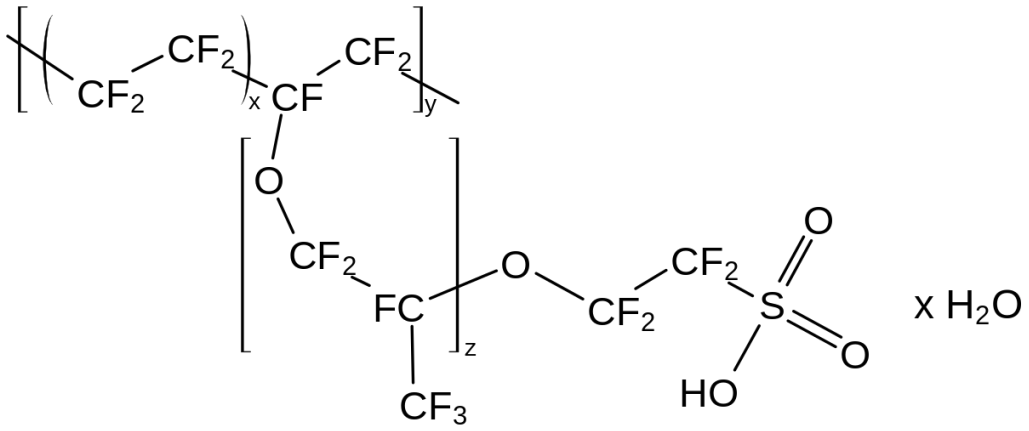

Figure 2.2: Chemical structure of the Nafion™ ionomer

The membrane should be hydrated to enable the proton conduction of the sulfonic groups [3], [7], [8]. A process called "the conditioning" or "break-in" is performed to humidify the sulfonic groups in the membrane before operation.

2.2.2 Gas Diffusion Layer:

The gas diffusion layer (GDL) is composed of macro and micro-porous layers and serves as the gas transfer medium for fuel and oxidant. While supplying the hydrogen and air/oxygen to the electrodes, it also helps evacuation of the water, either produced by the reaction or coming as humidity thanks to the macro and micro-porous layers and hydrophobic coating. Furthermore, the GDL provides mechanical stability and electrical contact between the catalyst layer and the current collectors.

The GDL is composed of either woven carbon cloth or carbon paper as the macro-porous layer and a thin coating which includes carbon particles as the micro-porous layer that is mixed with polytetrafluoroethylene (PTFE) for hydrophobicity. The microporous layer of a sample used in this thesis study is shown in Figure 2.3.

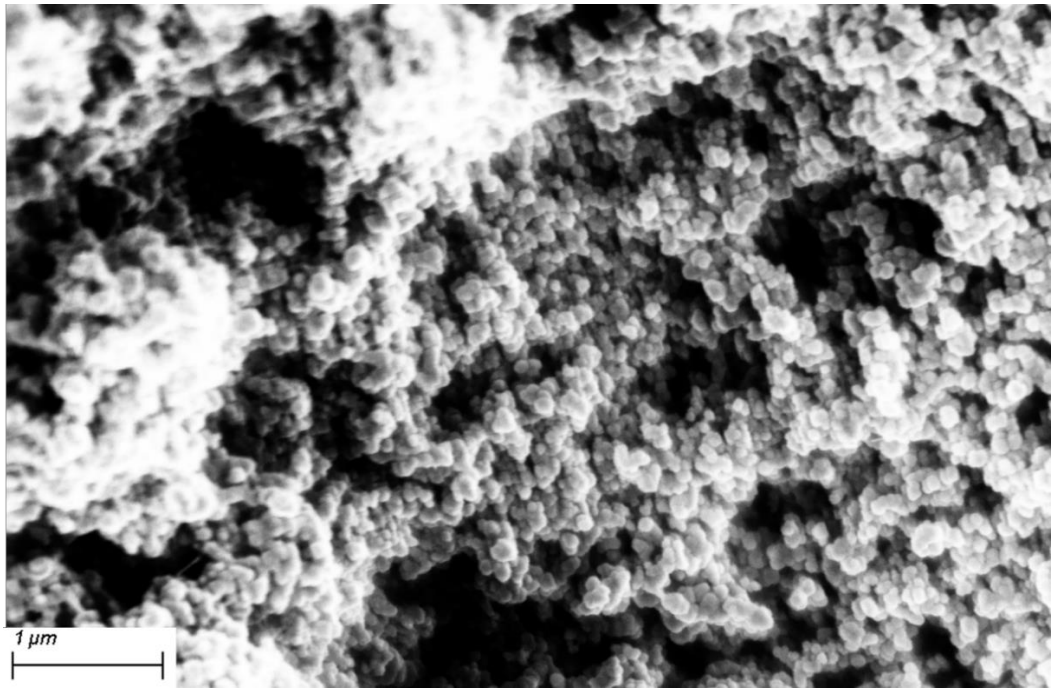

Figure 2.3: The scanning electron microscope image of the micro-porous carbon particles of a GDL used in this thesis

2.2.3 Catalyst Layer:

Catalyst layer (CL) is the medium that makes HOR and ORR possible. The standard material used for the catalyst layer is metallic Pt on high surface area carbon support. Pt is the most common catalyst for now because of its high stability against harsh operating conditions and low overpotential for the oxidation and reduction reactions [3], [7], [8].

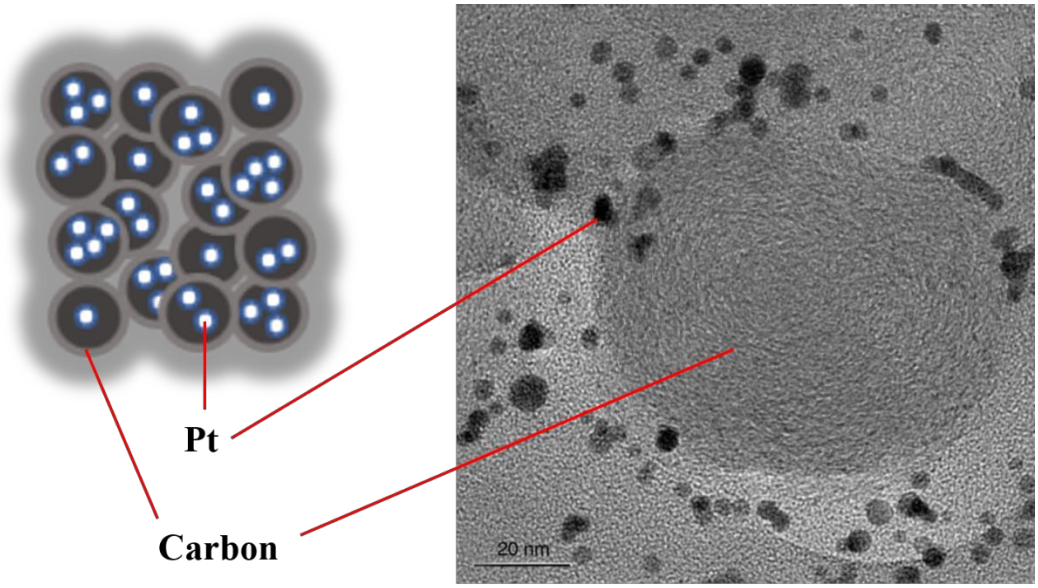

Figure 2.4: The representation (left) and the transmission electron microscope image (right) [9] of the catalyst layer

CL is also critical for its ionic conductivity that provides proton transport to/from the membrane and electrical conductivity that provides electron transport from anode to cathode. Furthermore, the carbon support of the CL is a continuation of the micro-porous layer of the GDL and this facilitates the gas diffusion and water removal.

The catalyst layer can be coated onto the GDL or the Nafion membrane. In this thesis, catalyst coated GDLs are used.

2.3 Calculation for Mass Flow Rate

The amount of gas that will be consumed for a desired current is calculated from the Faraday's law as follows:

$$\dot{N} = \frac{I}{nF} \tag{2.8}$$

where $\dot{N}$ is the reactant consumption rate in mole/s, I is the current, n is the number of moles of electrons exchanged per mole and F is the Faraday's constant which is 96,485 C/mol

The molar hydrogen consumption rate will be: $\dot{N}_{H_2} = \frac{I}{2F}$ since 2 electrons are involved and the molar oxygen consumption rate will be $\dot{N}_{O_2} = \frac{I}{4F}$ since 4 electrons are involved. The evaluation of these values for I=1A would give:

$\dot{N}_{H_2} = 3.11\ x\ 10^{-4}$ mole/min

Now, to find the flow rate, this value should be translated into volume by using the ideal gas law:

$PV = NRT$ where P is the pressure, V is the volume, R is the ideal gas constant and T is the temperature. In this thesis study, the common operation temperature used is 55 ℃ and the pressure used 1,5 atm. Replacing these values, the hydrogen consumed is calculated to be:

$\dot{V}_{H_2,consumed} = 0.005578$ L/min-A and likewise, oxygen consumed or, if the reactant is air, air consumed would be:

$\dot{V}_{O_2,consumed} = 0.00279$ L/min-A

$\dot{V}_{Air,consumed} = 0.0133$ L/min-A

These flow rates are for a reaction producing 1 A of current and the stoichiometric ratios of 1 for anode and cathode.

2.4 Cyclic Voltammetry

Cyclic voltammetry (CV) is a versatile and quick electrochemical technique which gives valuable information on reduction and oxidation processes as well as kinetic and thermodynamic details of chemical systems. CV measurement is usually performed with three-electrode arrangement: Reference electrode (RE), working electrode (WE) and counter electrode (CE). The potential relative to the RE is scanned at the WE and the resulting current

flowing through the CE is recorded. The CV measurements can be done both in situ and ex situ. However, in this thesis, all the CV measurements are performed in situ. Thus, the RE is the pseudo-reference electrode and is connected to the anode side, therefore scanned potentials are in the form of V vs reversible hydrogen electrode (RHE). The CE is connected to the anode as well. The cathode side is employed as both WE.

A ex-situ cyclic voltammogram of Pt/C – Nafion electrode is shown in Figure 2.5:

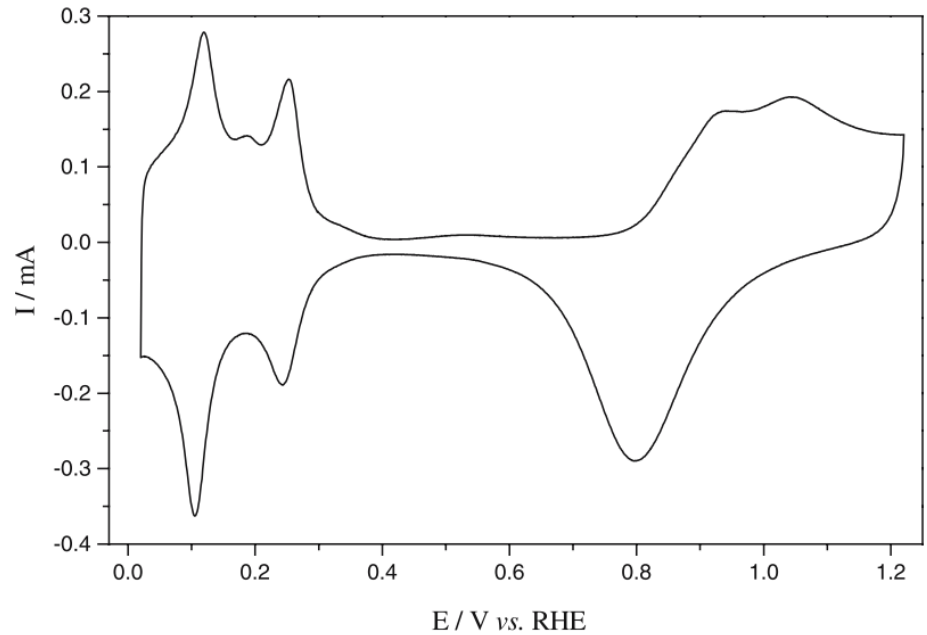

Figure 2.5: Cyclic Voltammogram of Pt-black/Nafion electrode [10]

The peaks appear in the ex-situ voltammogram are the result of oxidation and reduction reactions on the Pt surface. The Nernst equation can be used to understand the behavior of an electrochemical system against a potential sweep. For the reduction and oxidation on the Pt surface, the Nernst equation can be modified as:

$$E = E^0 + \frac{RT}{nF}\ln\frac{[H^+]}{[H_2]} = E^0 + 2.3026\frac{RT}{2F}\log_{10}\frac{[H^+]}{[H_2]} \quad \textbf{(2.9)}$$

where E is the applied potential, E^0 is the formal potential, R is the ideal gas constant, T is the temperature, n is the number of electrons produced per hydrogen, F is the Faraday's constant, $[H^+]$ and $[H_2]$ are the concentrations of redox couples.

When a potential E is applied, H^+ will be reduced to H_2 at the electrode surface until $2.3026\frac{RT}{2F}\log_{10}\frac{[H^+]}{[H_2]}$ is equal to $E - E^{0,}$. This will result in a current and H^+ will deplete until the potential is reversed.

Figure 2.5 is marked into regions in Figure 2.6 to understand what really happens during a CV scan.

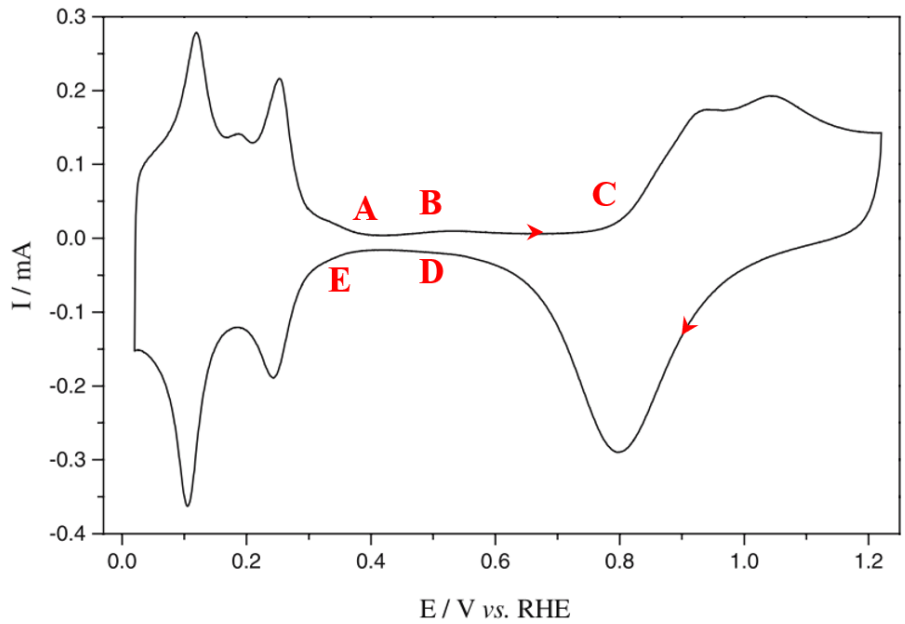

Figure 2.6: Cyclic Voltammogram of Pt-black/Nafion electrode with marked regions

When the scan starts with a positive potential which is about 400 mV (point A) until about 500 mV (point B), a relatively small capacitive current is measured which occurs due to the charging of the electrolytic double layer. Above this potential (point B), oxygen is chemisorbed on the Pt surface as:

$$Pt + OH^- \rightarrow Pt - OH + e^- \quad \textbf{(2.10)}$$

Above 800 mV (point C) Pt-oxide formation starts:

$$Pt - OH + OH^- \rightarrow Pt - O + H_2O + e^- \quad \textbf{(2.11)}$$

When the potential is reversed, these two reactions above change direction as well and the oxygen molecules around the Pt surface are reduced. When all the surface oxide is depleted (point D) the small capacitive double layer current is observed again. At around 400

mV, hydrogen adsorption starts on the Pt surface. Two well-resolved peaks at around 275 mV and 125 mV are observed which are attributed to H adsorption/desorption on Pt(100) and Pt(110) crystal surfaces respectively [8]. A full hydrogen layer is created after the second peak is completed. Then the voltage is reversed again to start a new cycle and the hydrogen is oxidized.

The hydrogen oxidation occurs on the Pt surface in 2 steps. It is either via Tafel-Volmer mechanism or Heyrovski-Volmer mechanism [11].

<u>First step: electrochemical adsorption</u>

$$H_2 + 2Pt \leftrightarrow 2PtH_{ads} \qquad \text{(Tafel Reaction)} \qquad \textbf{(2.12)}$$

$$H_2 + Pt \leftrightarrow PtH_{ads} + H^+ + e^- \qquad \text{(Heyrovski Reaction)} \qquad \textbf{(2.13)}$$

<u>Second step: discharging of adsorbed hydrogen</u>

$$PtH_{ads} \leftrightarrow Pt + H^+ + e^- \qquad \text{(Volmer Reaction)} \qquad \textbf{(2.14)}$$

The overall oxidation of hydrogen is a very fast reaction compared to the oxygen reduction reaction on the cathode.

Figure 2.7 summarizes the adsorption/desorption processes mapped on the CV shown in Figure 2.6.

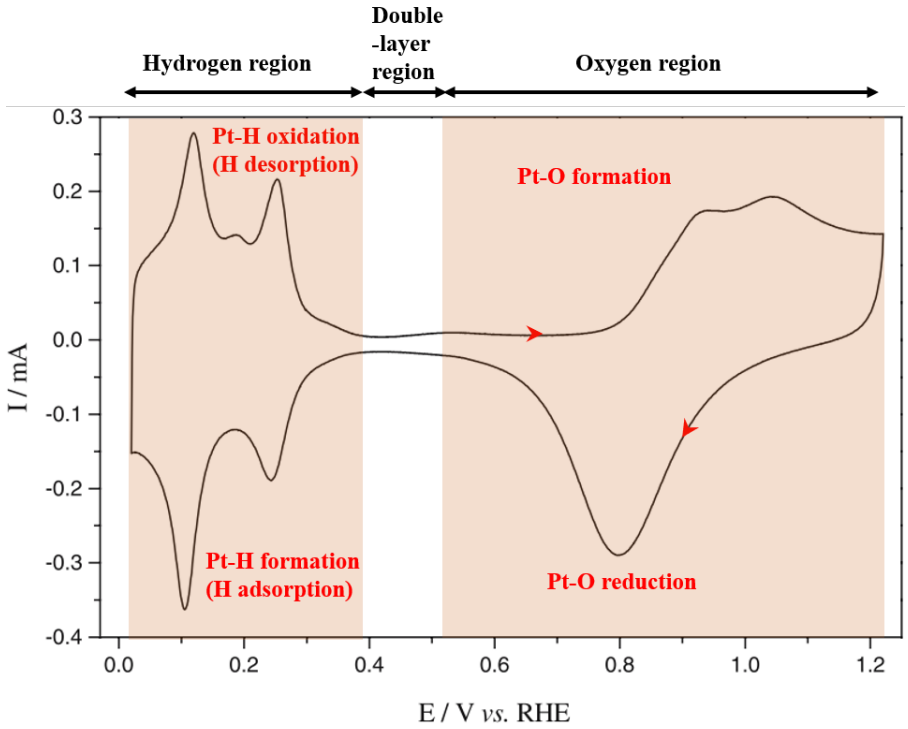

Figure 2.7: Cyclic Voltammogram of Pt-black/Nafion electrode with redox processes shown

The electrochemical surface area (ECSA) is an important performance metric. It can be used to get information on the catalyst utilization or membrane electrode assembly (MEA) health monitoring.

ECSA is related to the total charge required for the complete adsorption of hydrogen, forming a monolayer. The voltage range should be selected such that the charge transfer reactions are adsorption limited. In order to avoid carbon corrosion, the applied voltage should be smaller than 0.8 V.

In addition to the hydrogen adsorption/desorption reaction mentioned above, for the ECSA calculation, CO stripping might be used as well since CO can strongly adsorb on the Pt surface. However, for this type of operation the anode side should be fed with CO instead of H_2 as the fuel which is not used in this thesis.

The charge required to desorb one monolayer of hydrogen is calculated by integrating the shaded region of an in-situ voltammogram as defined in Figure 2.8.

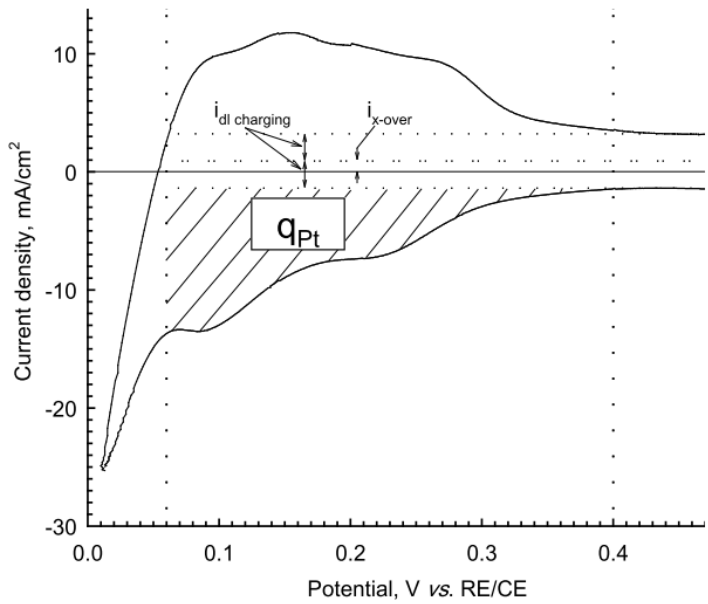

Figure 2.8: The charge density region (shaded area) for ECSA calculation [12]

As seen in Figure 2.8, the region starts at the beginning of the hydrogen adsorption or the voltage where the pseudo-capacitive layer ends. The end of the region is where the Pt(110) adsorption peak onsets.

This experimental charge density value is then divided by the charge required to reduce one monolayer of protons on Pt (defined by Γ) to find the overall surface area of Pt that is involved in the catalytic activity. This new value is normalized by dividing with the Pt loading (L) to find the electrochemically active area per mass. The overall formula is given below:

$$ECSA(cm_{Pt}^2/g_{Pt}) = \frac{q_{Pt}}{\Gamma . \mathrm{L}} \quad \textbf{(2.15)}$$

where Γ is 210 $\mu C/cm_{Pt}^2$ [13] and L is the Pt loading in the electrode in $g_{Pt}/cm_{electrode}^2$

.

2.5 Degradation Mechanisms

Commercialization of fuel cells have brought about some new challenges in cost and durability. Up until then, fuel cells were tested under ideal conditions and with high Pt loadings. However, if this technology is to be a successful alternative to the existing ones, it

needs to withstand some challenging conditions such as long-term operation, operation under extreme temperatures, use of less or cheaper materials (i.e. reduction of Pt content) and different operation modes that increases the hydrogen utilization (i.e. dead-ended or near-dead-ended anode modes). In this part, the degradation mechanism for each fuel cell component is summarized with a special emphasis for the carbon support degradation (carbon corrosion) which is the main focus of this thesis study.

The membrane degradation can be classified into three categories: mechanical, thermal and chemical degradation [14]. Operation under different temperatures and humidity levels causes the membrane to swell and dry, leading to expansion and contraction of the membrane and creation of local stress areas. As a result, punctures, pinholes, cracks or tears can form in the membrane. This is the mechanical degradation. It can spoil the performance via hot spot formation, fuel crossover or formation of radicals [15], [16]. The second mechanism, thermal degradation is usually caused by the high operating temperatures and poor water management which causes the dehydration of the membrane[7], [15] This dehydration reduces the proton conduction which leads to the performance loss. Finally, the chemical degradation stems from the radical attack such as peroxides and hydroperoxides that are formed as a result of operation under high temperature, low humidification, high gas pressure and high cell voltages [15], [17].

Catalyst degradation shows itself as the electrochemically active surface area (ECSA) loss and takes place mainly on the cathode catalyst layer due to the high potentials and the existence of the oxidant in the cathode. It can be observed in 2 main forms: coarsening and oxidation of particles [14]. There are three primary coarsening mechanisms: coalescence, dissolution of particles and electrochemical Ostwald ripening [14], [18], [19]. Coalescence occurs when Pt crystals migrate on the carbon support surface and agglomerate/sinter together when in close proximity [7], [18], [19]. Dissolution of Pt particles is due to high potentials, potentials which are higher than 0.8 V [7], [14], [17]–[21]. These dissolved particles either reprecipitate onto other Pt particles and form larger and energetically more favorable particles, or diffuse into electrochemically inactive parts of the membrane electrode assembly such as Nafion membrane, forming the Pt band [18]. Ostwald ripening is a thermodynamically driven process in which small particles dissolve and redeposit onto larger

particles to minimize the surface energy [7], [14], [17]–[21]. The Ostwald ripening and dissolution/reprecipitation are similar. In reprecipitation, the dissolved Pt ions may nucleate on a particle or defect which did not serve as a catalyst site. Finally, the oxidation of particles involves carbon support oxidation and the subsequent Pt particle detachment. The details of this process is explained in the next subsection.

A representative image for the catalyst degradation is given in Figure 2.9.

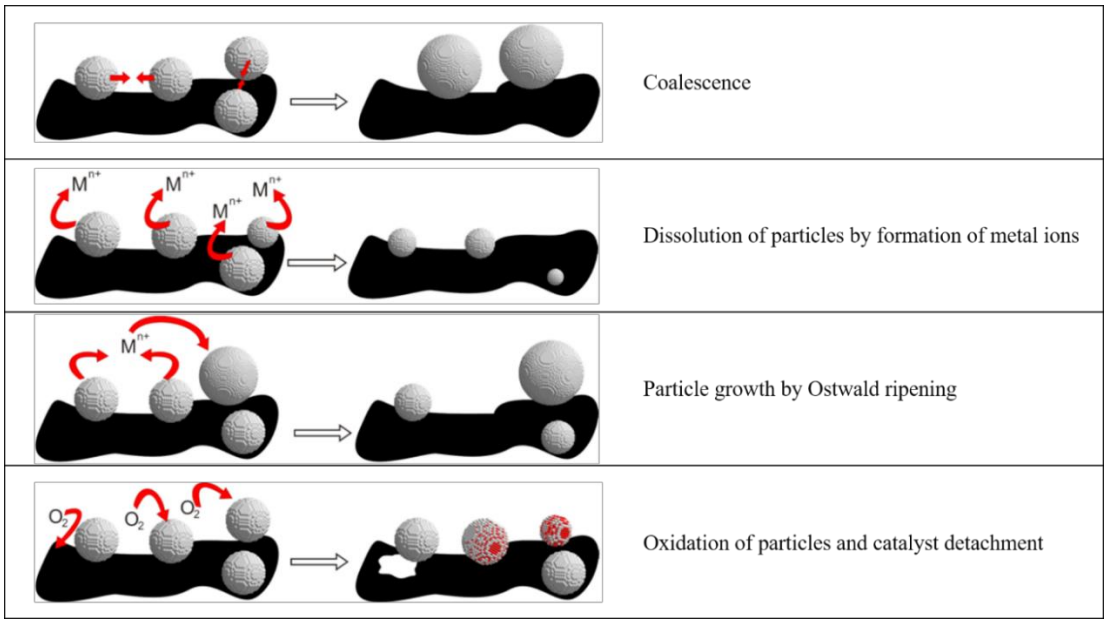

Figure 2.9: Representation image of catalyst degradation mechanisms [18]

2.6 Carbon Corrosion

The carbon support oxidation or carbon corrosion has been known for almost half a century [22]. The preliminary research on carbon corrosion was performed for phosphoric acid fuel cells which work at high temperatures (150 – 220 ℃). Until 2004 [23], [24] it was regarded as a high temperature phenomenon and negligible for PEMFCs that operates at lower temperatures.

Thermodynamically, the oxidation of carbon takes place at very low potentials:

$$C + 2H_2O \leftrightarrow CO_2 + 4H^+ + 4e^- \qquad E_0 = 0.207\,V \text{ vs RHE} \qquad \textbf{(2.16)}$$

This direct pathway of carbon oxidation is a slow reaction for PEMFC operating temperatures. Fortunately, this reaction does not have a considerable effect on the fuel cell performance. However, it was reported that the oxidation of the carbon surface can occur at 65 ℃ at potentials higher than 0.8 V vs RHE [23] with an indirect pathway as follows:

$$C \rightarrow C_{(s)}^{+} + e^{-} \tag{2.17}$$

$$C_{(s)}^{+} + H_2O \rightarrow CO_{surf} + 2H^{+} + e^{-} \qquad E_0 > 0.3\,V \text{ vs RHE} \tag{2.18}$$

$$CO_{surf} + H_2O \rightarrow CO_2 + 2H^{+} + 2e^{-} \qquad E_0 = 0.8\,V \text{ vs RHE} \tag{2.19}$$

When the potential is higher than 0.3 V vs RHE, carbon surface oxides start to form irreversibly. The CO_{surf} is then oxidized to form CO_2 at a potential of 0.8 vs RHE. Willsau et al. [25] states that the CO_{surf} forms on the carbon support and adsorbed on Pt nanoparticles to form $CO_{surf} + Pt \rightarrow Pt - CO_{ads}$, therefore its electro-oxidation occurs only when there is Pt around. When there is no Pt around, carbon corrosion occurs at potentials above 1.1 V vs RHE.

Willsau et al. [25] and Roen et al [24] reported that the existence of Pt decreases the potential for the CO formation and increases the CO_2 emission. They concluded that Pt catalyzes the overall carbon oxidation reaction for temperatures higher than 50 ℃ which is explored in other works as well [26]–[28].

At elevated electrode potentials ($E > 0.98\,V$ vs RHE), the electrochemical formation of platinum oxide occurs as follows [17]:

$$Pt + H_2O \leftrightarrow PtO + 2H^{+} + 2e^{-} \qquad E_0 = 0.98\,V \text{ vs RHE} \tag{2.20}$$

Thus, at potentials higher than 0.98 V vs RHE, the Pt surface is reversibly oxidized and passivated into PtO. This prevents the Pt from catalyzing the carbon oxidation reaction.

However, enhanced carbon oxidation reaction is observed when cycling the voltage between 0.6 V and 1.0 V vs RHE [29]. It was explained that the Pt oxidation is a reversible process and during the load cycling, if the lower limit of the potential is close to 0.7 V vs RHE, this PtO blanket on the Pt surface disappears and forms again and again. This

instantaneous restructuring of the Pt surface which is caused by the repeated reduction and oxidation of Pt nanoparticles, catalyzes the process of carbon corrosion [24], [29].

Apart from the reaction kinetics, it is also important to discuss the conditions that provoke the corrosion of the carbon support. The potentials mentioned above can go as high as 1 V. However, most of these data are acquired by using an external potentiostat with nitrogen flowing in the cathode. It seems odd to observe such elevated potentials during the normal operation of a fuel cell. Nevertheless, it was shown that the cathodic potentials can reach to 1.5 V vs RHE when there is local fuel starvation in the cathode [30].

The local fuel starvation is a dangerous operating condition which involves local undersupply of the reactant gas while the oxidant supply is sufficient. This situation can induce local cathode potentials significantly higher than 1 V. These high potentials induce carbon support oxidation that leads to permanent performance loss and also shows itself as electrochemically active area loss.

Figure 2.10 shows what happens when some part of the MEA experience local fuel starvation. On the left-hand side of the MEA, labeled as region A, fuel is present on the anode and the fuel cell behaves as normally. This fuel-rich region can deliver high currents and the potential will be close to its equilibrium voltage. However, when there is no fuel present, labeled as region B, there is no electron or proton source at lower potentials and available oxygen in region B lowers the electrolyte potential (Φ). The electrode will shift to much higher potentials in order to maintain the interfacial potential difference imposed by the fuel-rich part of the cell and still conserving the current. Due to this higher cathode potentials, the current will flow from cathode to anode in the fuel-starved region (region B). To sustain such a current flow in region B, oxygen reduction occurs in the anode thanks to the oxygen that permeates through the membrane and carbon corrosion takes place in the cathode. The high electrochemical potential of the cathode not only promotes carbon oxidation, but also favors Pt dissolution. This reverse-current mechanism is first explained by Reiser et al. [31] and confirmed in other works [30], [32], [33].

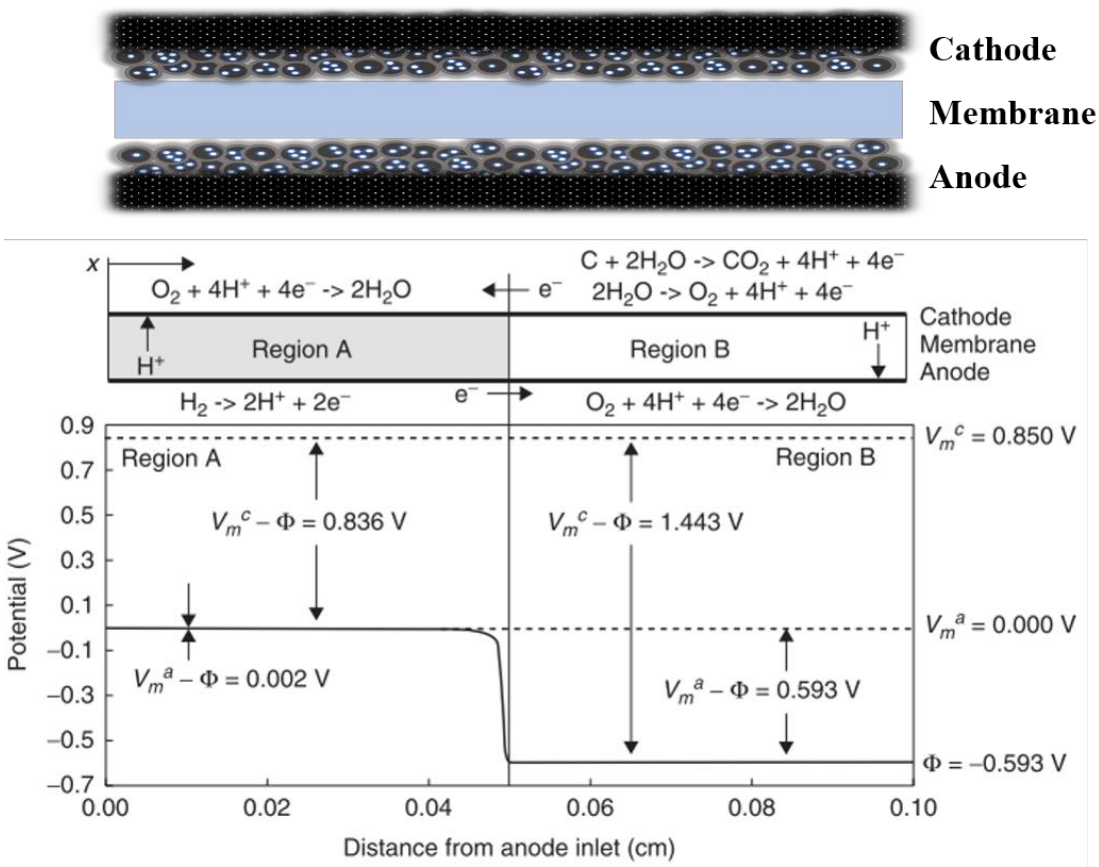

Figure 2.10: Potential distributions during the reverse current conditions where V_m^a is the anode metal potential, V_m^c is the cathode metal potential, Φ is the electrolyte potential [31].

Some reasons for the fuel starvation are 1) improper gas supply in which the channels of the flow field can be blocked and cause insufficient supply of the reactant, 2) sudden load increase where feeding of the gas cannot follow a sudden load demand fast enough, 3) start-up/shut-down processes in which during a prolonged shut-down the anode is filled with air and after the start-up, the region close to the anode exit is hydrogen starved, 4) dead-ended anode operation where the anode exit is closed and water as well as nitrogen accumulates in the anode flow field leading to a blanketed/fuel starved region.

The gas diffusion layer (GDL) consists of carbon fibers coated with Teflon (PTFE) for hydrophobicity. The micro-porous layer (MPL) is an intermediate layer between the catalyst layer (CL) and GDL which is made up of the same carbon black as CL. The Teflon coating in GDL makes it less susceptible to electrochemical oxidation of carbon. And there is no Pt

in MPL that can catalyze a carbon oxidation reaction. However, carbon in GDL and MPL is still prone to electrochemical oxidation at high cathodic potentials during a fuel starvation and in the existence of water and temperatures higher than 80 ℃ [14], [34], [35].

Delamination of MPL from the GDL was also reported [36], [37] but under freeze/thaw cycling from -15 ℃ to 80 ℃.

2.6 Accelerated Stress Tests in Literature

The search for new catalyst support materials that are more robust and durable against carbon corrosion is ongoing. Durability tests are used to test their performance against harsh operating conditions. However, when these tests last more than thousands of hours, the research for new materials become time consuming and expensive.

Accelerated stress tests (AST) are designed to solve this problem. Research groups as well as organizations such as American Department of Energy (DOE) and Fuel Cell Commercialization Conference of Japan (FCCJ) came up with different ASTs focusing on different types of degradation issues. Some of them are: membrane/MEA degradation [38]–[47], ionomer degradation [40], electrocatalyst degradation [38]–[41], [47]–[50] and carbon support degradation [24], [38]–[41], [47], [50], [51].

As stated in the thesis objective, first part of the thesis focuses on the ASTs designed specially to speed up the carbon corrosion and propose a new AST that works under realistic operating conditions such as using hydrogen as the fuel, oxygen as the oxidant and extracting current under load cycling.

The carbon electrode used in this thesis is composed of 3 main regions: the gas diffusion layer (GDL), the micro-porous layer (MPL) and the catalyst layer (CL). The GDL (Sigracet 39BC) was carbon paper which is composed of carbon fibers. These fibers are coated with Teflon (PTFE) for hydrophobicity. As a result, this layer is durable against electrochemical corrosion. The MPL contains carbon black, the same carbon black in the CL but due to the lack of Pt particles in the carbon black of MPL, this layer is not susceptible to electrochemical corrosion because Pt catalyzes oxidation reactions [14], [17]. However, it is

reported that MPL can experience carbon corrosion due to chemical surface oxidation by water and high potentials [35], [52] . The CL is composed of catalyst support which is the Pt loaded carbon black. This layer is prone to corrosion and the mechanism are explained previously.

The ASTs that focuses on the carbon corrosion (or carbon support degradation) in the literature are summarized below.

Table 2.1: AST protocol designed for carbon corrosion by Yu et al. (2006) [53]

Yu et al. (2006)		
Cycle	Artificial startup/shutdown environment using 4-way valves for anode and cathode. Single cell 50 cm^2	
Number	200 cycles	
Cycle time	0.52 to 5.2 seconds	
Temperature	80ºC	
Relative humidity	Anode/cathode 66/66%	
Fuel/oxidant	Hydrogen/Air	
Pressure	1.5 bar	
Metric	**Frequency**	**Target**
ECSA/cyclic voltammetry	After every 20 startup/shutdown cycles	

In 2006, Yu et al. built an artificial startup/shutdown environment using 4-way valves for the inlets, that can control the gas purge front residence time (Table 2.1). They used real life operation fuels; hydrogen and air for the anode and cathode respectively. They designed

this AST to show that graphitized carbon support shows higher carbon corrosion resistance against conventional carbon supports.

Table 2.2: AST protocol designed for carbon corrosion by American Department of Energy in 2007 [38]

American Department of Energy-2007		
Cycle	Hold at 1.2V for 24h; run polarization curve and ECSA test; repeat for total of 200h. Single cell 25–50 cm^2	
Number	Continuous operation for 200 h	
Cycle time		
Temperature	95ºC	
Relative humidity	Anode/cathode 80/80%	
Fuel/oxidant	Hydrogen/N_2	
Pressure	1.5 bar	
Metric	**Frequency**	**Target**
ECSA/cyclic voltammetry	Every 24 h	$\leq$40% loss of initial area

In the reference [38], the part "Catalyst Support Cycle and Metrics" is the American Department of Energy (DOE) test protocol for carbon corrosion (Table 2.2). In this 2007 version, they proposed to use hydrogen on the anode and nitrogen on the cathode while holding the potential at 1.2 V for 200 hours. The details of this protocol are given in Table

2.2. Since no current is extracted, an external potentiostat is employed to apply a potential as high as 1.2 V.

Table 2.3: AST protocol designed for carbon corrosion by The Fuel Cell Commercialization Conference of Japan in 2010 [39]

The Fuel Cell Commercialization Conference of Japan		
Cycle	Triangle sweep cycle: 500 mV/s between 1.0 V and 1.5 V; run polarization curve and ECSA; repeat for total 400 h. Single cell 25 cm^2	
Number	60,000 cycles	
Cycle time	2 seconds	
Temperature	80ºC	
Relative humidity	Anode/cathode 100/100%	
Fuel/oxidant	Hydrogen/N_2	
Pressure		
Metric	**Frequency**	**Target**
ECSA/cyclic voltammetry	After 10, 100, 1k, 3k, 10k, 20k, and 30k cycles	$\leq$50% loss of initial area

The Fuel Cell Commercialization Conference of Japan (FCCJ) proposed their own test protocols in 2010 [39] (Table 2.3). Instead of a potential hold, they reported that a start/stop cycle in the form of a triangle sweep would promote a faster carbon corrosion. In their cycle, the potential is swept from 1 V to 1.5 V with 0.5 V/s increments while feeding the anode

with hydrogen and cathode with nitrogen for 60000 cycles. The failure criterion was an ECSA loss of 50 %.

Table 2.4: AST protocol designed for carbon corrosion by American Department of Energy in 2013 [54]

American Department of Energy-2013		
Cycle	Triangle sweep cycle: 500 mV/s between 1.0 V and 1.5 V; run polarization curve and ECSA; repeat for total 400 h. Single cell 25–50 cm^2	
Number	5000 cycles	
Cycle time	2 seconds	
Temperature	80ºC	
Relative humidity	Anode/cathode 100/100%	
Fuel/oxidant	Hydrogen/N_2	
Pressure	Atmospheric pressure	
Metric	**Frequency**	**Target**
ECSA/cyclic voltammetry	After 10, 100, 1k, 3k, 10k, 20k, and 30k cycles	$\leq$40% loss of initial area

In 2013, American DOE revised their AST protocols [54] and changed their accelerated stress test procedure for carbon corrosion (Table 2.4). The revised version is the same as FCCJ except for the number of cycles and the failure criterion which was still the same; 40 % ECSA loss.

Table 2.5: AST protocol designed for carbon corrosion by Macauley et al. (2018) [55]

Macauley et al. (2018)		
Cycle	Potentiostatic square-wave pulse with varying voltage upper limit:0.95-0.6 V and lower limit: 0.4-0.8 V with 0.05 V increments both. and potential hold times ranging from 0.5 min. to 5 min. Single cell 50 cm^2	
Number	Continuous operation for 1000 h	
Cycle time		
Temperature	80ºC	
Relative humidity	Anode/cathode 100/100%	
Fuel/oxidant	Hydrogen/Air	
Pressure	1 bar	
Metric	**Frequency**	**Target**
ECSA/cyclic	After 0, 200, 400, 1000 h	$\leq$40% loss of initial area

voltammetry		

In 2018, Macauley compared DOE and FCCJ carbon corrosion protocols to their own AST (Table 2.5). What they proposed is dramatically different than the other ASTs because 1) they use real life operation fuels, 2) they run the cell under real life operating conditions. So, unlike the other ASTs, this test can be applied directly in-situ, complying with the physical constraints of real system operations. However, a vital disadvantage of this AST is the duration. It takes more than 1000 hours to degrade the carbon support by 40 %.

3 EXPERIMENTAL METHODS

3.1 The Overall Setup

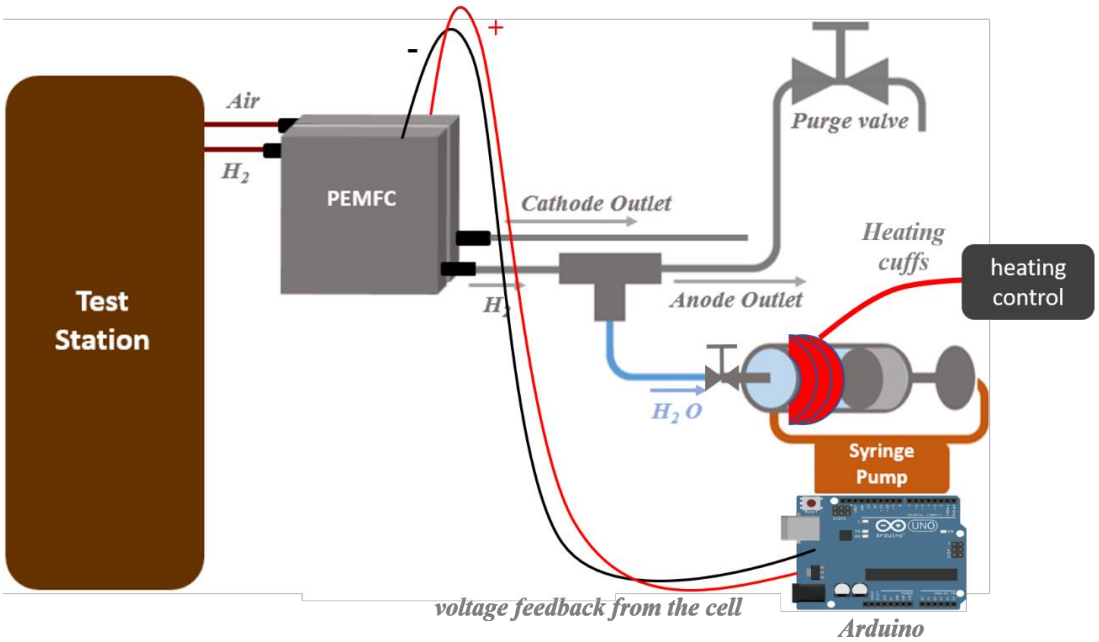

Figure 3.1: PEMFC test setup

The overall setup in Figure 3.1 has some modifications to make the fuel cell possible to work in flow through, ultra-low flow and dead-ended anode modes of operation. The humidified air and hydrogen are fed into the cell through the cathode and the anode inlets respectively by the built-in mass flow controllers in the test station. The cathode outlet connects directly to the back-pressure unit. The anode outlet is separated into two different

paths: 1- directly to the syringe pump, 2- to the backpressure unit through a manual purge valve.

For the flow through operation, it is enough to keep the purge valve open and the syringe pump off. For the ultra-low-flow operation, the purge valve should be closed so that the only route for the outlet flow is to the syringe pump. And for the dead-ended anode operation, the purge can be performed through the purge valve, keeping the syringe pump off. A second option for this mode is to keep the purge valve closed and use the syringe pump for the anode purge. This option is a fully automated, highly precise way of purging the anode.

Figure 3.2: Fuel cell test station (left) and the back-pressure unit (right)

The test station which is a Model 850e (Scribner Associates) and accompanying high temperature back-pressure unit (Scribner Associates) is shown in Figure 3.2. It can control the reactant flows, temperature, humidity and the load and can perform electro impedance measurements.

The Teflon tubing is connected by stainless steel fittings to prevent leakage. The stainless-steel purge valve is a manual valve (Swagelok™) to enable dead-ended-anode operation.

Figure 3.3: A model NE-500 syringe pump

The syringe pump is a model NE-500 purchased from syringepump.com. It can maintain flow rates as low as 30 µl/h, generating a pressure about 2 bars. The syringe pump can be digitally controlled through an TTL logic interface.

A microcontroller unit called Arduino UNO is incorporated to the syringe pump for the smart control and computer monitoring. The Arduino can read voltage from the cell and decide whether to start the syringe pump as programmed.

3.2 Flow Control Setup

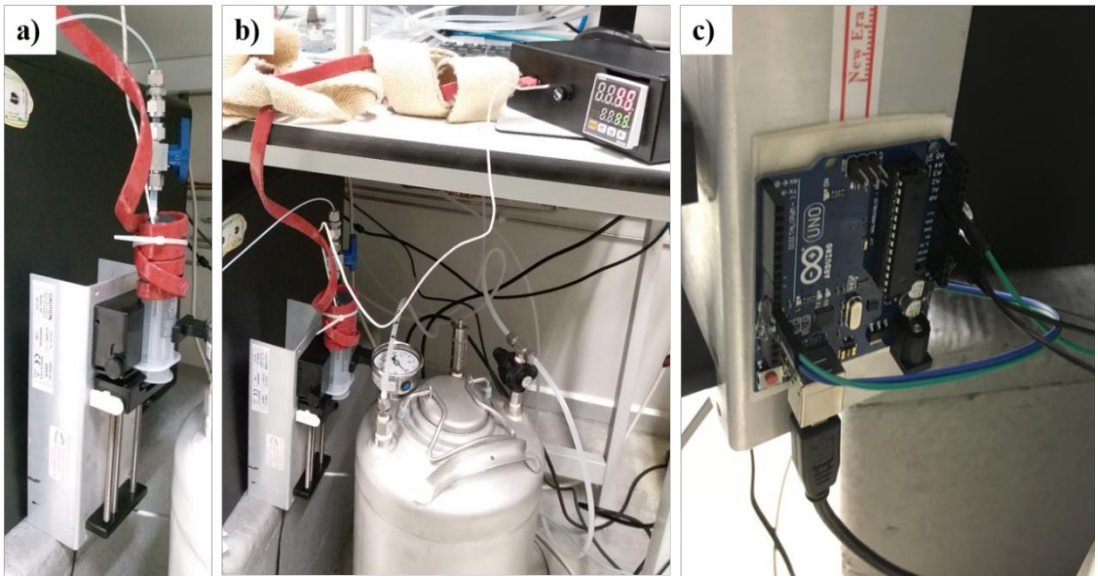

Figure 3.4: a) Syringe pump with the heating cuffs on the syringe, b) syringe pump with heating connections, c) Arduino controller connected to the syringe pump

Figure 3.4 shows the overall flow control setup. The syringe pump can be controlled and programmed via pump-to-pc network cable and a free software provided by the supplier. The control-only-option was limited to the parameters such as the flow rate and total volume to be dispensed. For the desired operation, the syringe pump was modified and programmed to start and stop with voltage feedback coming from the fuel cell.

Figure 3.5: Syringe pump control interface

The syringe pump can be programmed so that it can read digital inputs. This input should be in terms of TTL (transistor-transistor-logic) signal and the connection should be made through the RS-232 interface seen in Figure 3.5.

The programming of the pump is performed by entering the commands in a spreadsheet. For the program which was uploaded to the syringe pump via a commercial software called SyringePumpPro, please refer to the Appendix.

The second challenge to make this voltage feedback-controlled syringe pump possible was to incorporate an Arduino microcontroller to the syringe pump. The voltage was read through the analog pins, then evaluated inside the microcontroller and the resulting signal was sent by the digital output pins on the Arduino. The TTL signal generated to communicate with the syringe pump was a 0-5V amplitude, 100 ms wide square wave that was connected to the number 5 pin of the RS-232 interface on the pump. The status of the pump was also monitored to eliminate random pauses after start-up and shut-down of the pump. For the program uploaded to the Arduino, please refer to the Appendix. The pins used on the Arduino is shown in Figure 3.6.

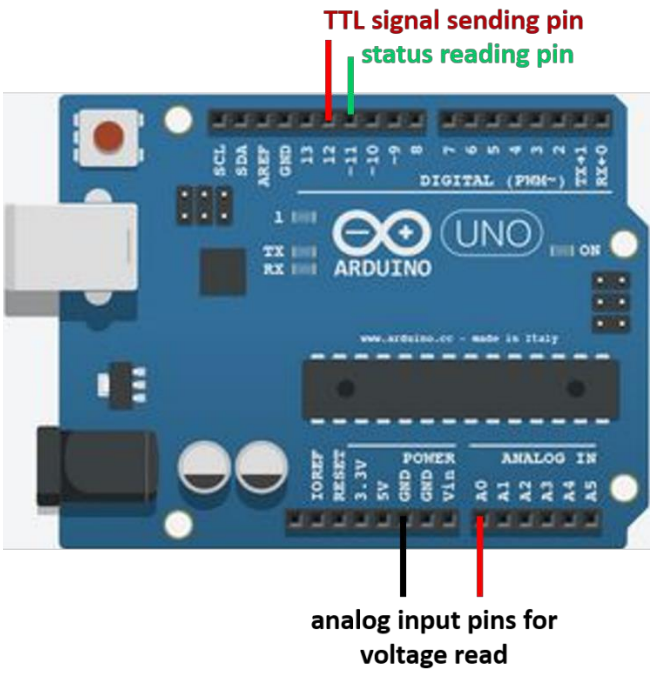

Figure 3.6: Arduino pins used for voltage reading and TTL signal generation

There was also the extra suction caused by the condensing steam when the saturated water vapor reaches the syringe. While the syringe pump is withdrawing at 50 µl/min, the saturated water vapor leaves the anode at 55 ℃ with a partial pressure of 0.157 bar [56]. When it reaches to the syringe, the temperature drops to 30 ℃ and the partial pressure of the saturated water vapor drops to 0.042 bar. The volume occupied by the water vapor decreases because of this condensation. As a result, the condensation of the water vapor will provide an extra suction at the anode. The extra flow caused by this suction is calculated as follows:

$$(P_{sat}(55) - P_{sat}(30))\dot{V} = \dot{n}\, R\, T \qquad \textbf{(3.1)}$$

where $\dot{V}$ is the volumetric flow rate, $\dot{n}$ is the molar flow rate, $P_{sat}(55)$ and $P_{sat}(30)$ are the steam pressures at 55 ℃ and 30 ℃ respectively, R is 8.314 x 10^{-2} L bar mol^{-1} K^{-1}, V is the volume migrating which is 50 µl/min and the temperature T is 30 ℃ (303 °K).

When this equation is solved for the mole number per minute, $\dot{n}$ is calculated to be 2.2726 x 10^{-7} mol/min. This value is multiplied by the mole number of nitrogen, 18 and

translated into volume by using the ideal gas law. The extra suction resulting from the condensation of the 55 ℃ steam is calculated to be 39.23 µl/min. This is almost two times the desired flow rate. Therefore, a heating system for the syringe was manufactured.

The syringe was heated to 45 ℃ to eliminate this extra suction and observed no considerable increase in the water level, which means there is not much water condensing and the heating eliminates the extra suction. The temperature was limited to 45 ℃ due to the polypropylene structure of the syringe used.

3.3 MEA preparation

Some of the original parameters were adopted from the reference [57]. The MEA preparation process is composed of catalyst ink preparation, coating the catalyst on gas diffusion layer and hot-pressing the gaskets, catalyst coated GDL and membrane together. The details are explained below.

3.3.1 Catalyst Ink Preparation

The catalyst powder HiSpec 4000 Pt/C (40 % Pt on carbon black from Alfa Aesar) was mixed to Nafion ion exchange resin (20% ionomer in alcohol/water from Aldrich) with a Pt/C to Nafion weight ratio of 77:23 in a water/isopropanol solvent. The addition of water to the isopropanol is to avoid reaction of the Pt/C powder with Nafion or oxygen. For 0.2 gr of Pt/C powder, 16 ml of isopropanol and 4-5 drops of double distilled deionized water was used.

The overall dispersion was first sonicated for 1 hour and then stirred for another hour.

3.3.2 Coating the Catalyst on Gas Diffusion Layer

The gas diffusion layers (GDL) used were Sigracet 39BC carbon paper (nafionstore.com) with 325 µm thickness. The microporous layer on GDL that was PTFE treated is about 100 µm thick.

The catalyst ink was sprayed onto the GDL with a spray gun following horizontal, vertical and diagonal routes. The amount of mass sprayed calculated with respect to the Pt loading. For this thesis, a Pt loading of 0.5 mg/cm^2 was used for both anode and cathode. For

such a Pt loading, the amount of solid weight increments for the GDLs with 25 cm^2 and 8.17 cm^2 area were 40.58 mg and 13.26 mg respectively.

The coated GDLs were dried in a 60 °C for 30 minutes. The resulting coating thickness is about 15 µm.

3.3.3 Hot-pressing the 7-layer MEA

Nafion 212 (fuelcellstore.com) with thickness 50.8 µm is sandwiched between 2 catalyst coated GDLs as well as teflon coated fiberglass gaskets. The overall assembly was hot-pressed at 130 °C under about 1 N for 5 minutes.

Below is a visual summary of the overall procedure (Figure 3.7) and the resulting MEA thickness (Figure 3.8):

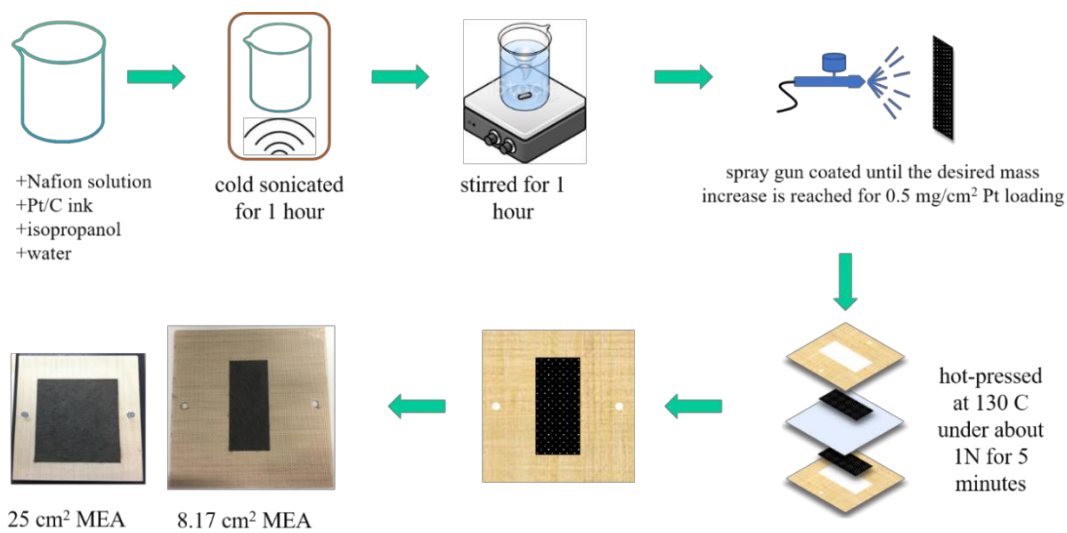

Figure 3.7: The MEA preparation procedure

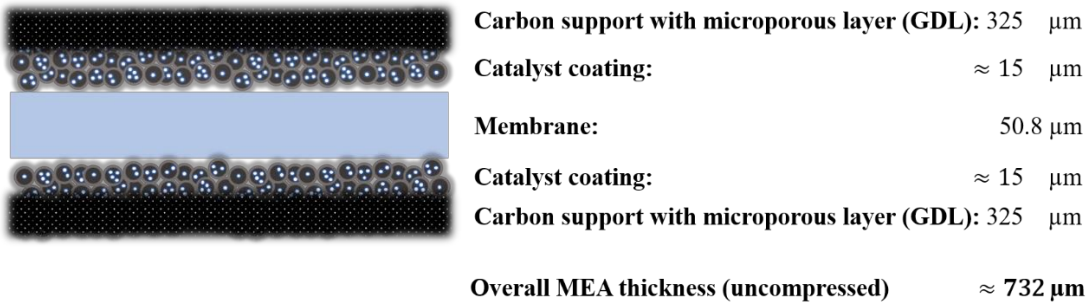

Figure 3.8: Overall uncompressed MEA thickness

3.4 Operation procedure

After preparing a new MEA, there are some procedures to follow before it can be used properly. First, a linear sweep voltammetry is performed to check if there is any fuel leakage (hydrogen crossover) or internal short. Second, the MEA is conditioned to make the Nafion™ membrane work properly. Then the beginning of life performance curves (IV curves) and cyclic voltammograms (CV) are recorded. CV is an important tool to monitor the MEA degradation because electrochemically active surface area (ECSA) data can be extracted from CV. The details of these procedures are explained in this section.

3.4.1 Linear Sweep Voltammetry

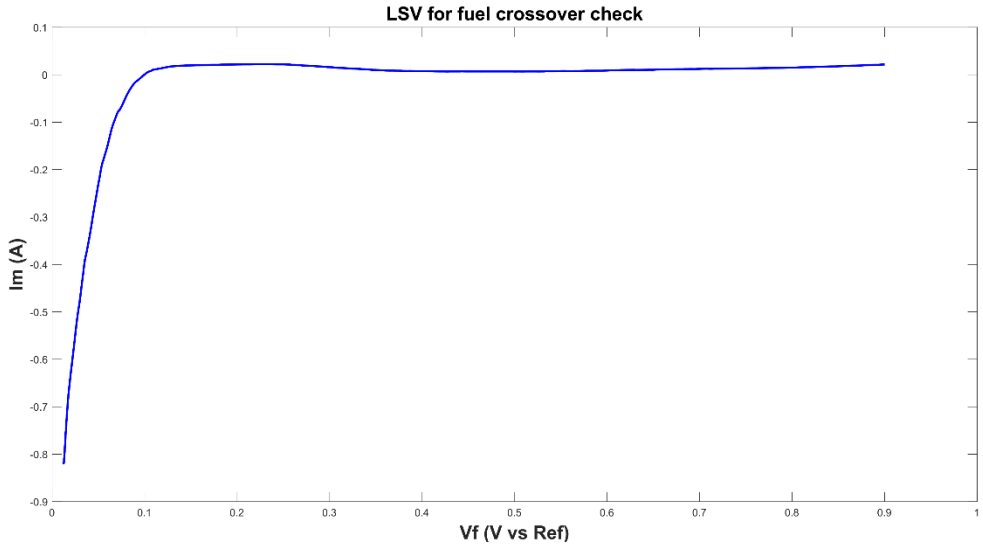

Figure 3.9: Linear sweep voltammogram for hydrogen crossover in our PEMFC

Linear sweep voltammetry (LSV) is a simple in situ technique which is quite accurate for single cells to detect fuel crossover [58]. Fuel crossover occurs when the reactant gasses penetrate from one electrode to the other through the membrane. It is the fuel (hydrogen) which degrades the cell when penetrates from the anode to the cathode and the amount of crossover of the oxidant (oxygen) is usually at a very slow rate which can be neglected.

Under open circuit conditions, the rate of the gas crossover is the highest since there is no reactant gas being consumed [45]. As a result, a potentiostat is required to scan the voltage while the cell is in open circuit condition.

The anode is fed with hydrogen whereas the cathode is fed with nitrogen, both with 100 % RH [59]. The flow rates used were 0.05 l/min for both. The temperature was set to 30 °C. The voltage is scanned from 0.1 V to 0.9 V with a scan rate of 1mV/sec [59]. This way, any hydrogen gas that might be present at the cathode is oxidized.

The Figure 3.9 is a typical LSV for one of the 8.17 cm^2 active area MEAs used in this thesis. There is a region between 0.4 V and 0.6 V which is free of any adsorption or desorption processes. This region is the transport limiting current region [60]. By using this current value, the hydrogen crossover flux can be calculated as follows [59]:

$$J_{x-over,H_2} = \frac{i_{lim}}{n.F} \tag{3.2}$$

where i_{lim} is the transport limiting current density (A/cm^2), n is the number of electrons involving the reaction (n=2 since H_2 releases 2 electrons in this case) and *F* is the Faraday's constant (96,485 C/electron-mole).

It is acceptable to have a crossover flux on the order of 10^{-9} $mole/cm^2/s$ [59] which corresponds to a limiting current density of 1 to 2 mA/cm^2. In case of a hydrogen crossover, the limiting current increases with the increasing potential. As a result, a linearly increasing value of the limiting current over increasing potential means that there is a finite resistance which indicates the fuel crossover, as well as an internal short. If the transport limiting region

has a constant current over potential, this means that there is no significant fuel crossover and the MEA is ready for the next step which is conditioning.

3.4.2 MEA Conditioning

The membrane in the MEA comes as dry and hot-pressing procedure of the MEA preparation make it even drier. Since Nafion™ membranes need to be humidified for a good ion conduction, a procedure to activate or break-in the Nafion™ membrane is necessary.

The conditioning can be performed offline and online. Offline procedure may involve exposing the MEA to saturated steam at high pressures (110 kPa) [61], boiling the MEA or rinsing the MEA in deionized water for 100 h.

The online procedure is easier since it can be performed in the test instrument itself. After installing the MEA in the test cell, a potential is applied to extract a decent current. The water formed as a result of the reaction humidifies the membrane. The applied potential cycle profile is shown below:

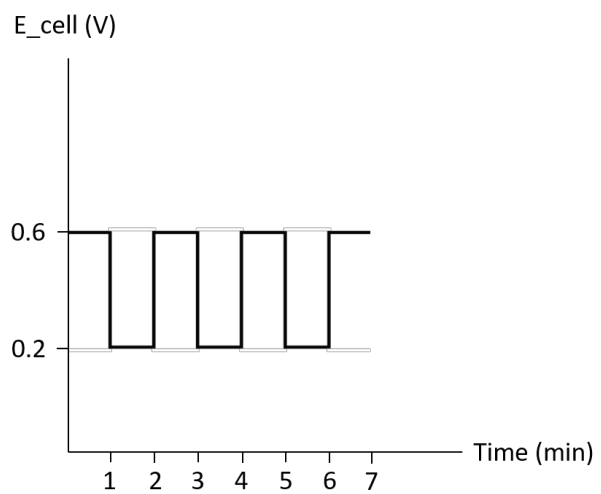

Figure 3.10: MEA break-in voltage cycling profile

As seen in Figure 3.10, applying 0.6 V for 60 seconds and 0.2 V for 60 seconds consecutively will help the cathode water which was formed as a result of the reaction to be mostly preserved in the cathode side. This procedure is continued until the current density is

stabilized which takes about 24 hours for our MEAs. Since the test cell is composed of a single cell, holding the potential at 0.6 V until the current density is stabilized can also make no big difference.

The flow rates for this process were 0.26 l/min for the anode and 1 l/min for the cathode. The temperature was 55 °C which was supposed to be the operating temperature. The backpressure was set to 1 bar. The anode and cathode relative humidity (RH) is 100 %.

3.4.3 Performance Tests

After the MEA is conditioned, the performance curves should be recorded to monitor the MEA health. Before each test, at least 30 minutes of nitrogen purging was necessary to get rid of any water accumulated in the bipolar plate channels.

The IV curves are taken by scanning the voltage from 0.2 V to 1 V with 0.05V/min scan rate. The flow rates used were 0.26 l/min for the anode hydrogen and 1 l/min for the cathode air. The temperature was 55 °C. The backpressure was set to 1 bar. The anode and cathode RHs were kept at 100 %.

3.4.4 Cyclic Voltammetry and ECSA Calculation

To be able to monitor the MEA degradation, a cyclic voltammogram was taken before and after every operation.

The parameters used for the cyclic voltammetry (CV) is similar to the LSV. The anode is fed with hydrogen and the cathode is fed with nitrogen, both with 100 % RH. The flow rates used were 0.05 l/min for both. The temperature was set to 30 °C.

The voltage is scanned from 0.025 V to 0.8 V with a scan rate of 100mV/sec with a number of 100 cycles first. This fast CV is taken as a conditioning to stabilize the voltammogram. Then, another scan with the same potential intervals but a scan rate of 40mV/sec is taken for 60 cycles.

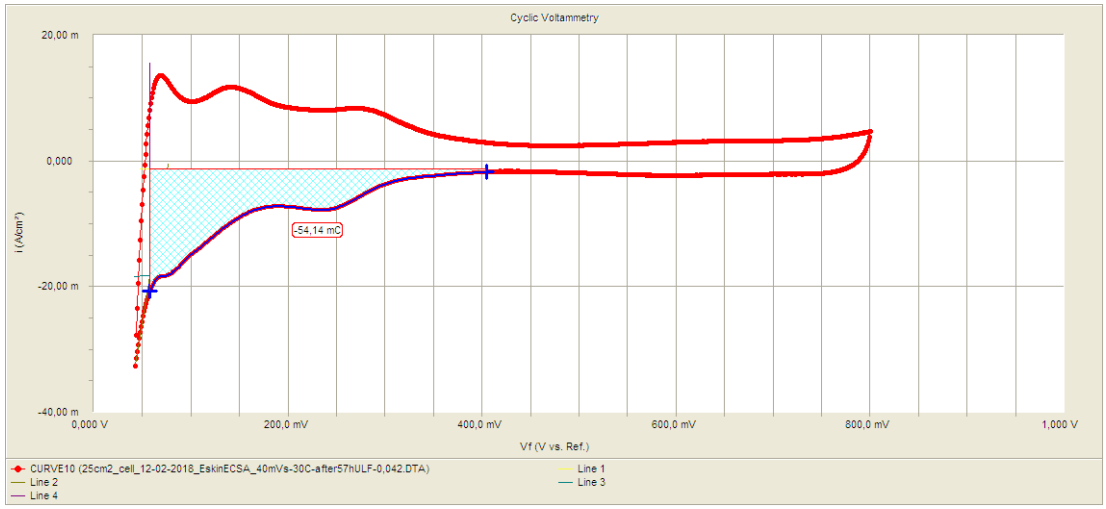

Figure 3.11: Cyclic voltammogram of a 25 cm^2 active area MEA in Gamry's original software

The resulting cyclic voltammogram is shown in Figure 3.11. To be able to calculate the ECSA, the potential window should be chosen such that the area under the curve due to H adsorption during the reverse scan starts from the onset of the first peak until the double layer capacitance region as shown in the Figure 3.11. The blue shaded area is then integrated using the commercial software (Gamry Echem Analyst). The calculated value is the charge density q_{Pt} (mC/cm^2). Here, the value showed as 54.14 mC should me in mC/cm^2 which is a minor mistake in the software.

$$ECSA(cm_{Pt}^2/g_{Pt}) = \frac{q_{Pt}}{\Gamma . \mathrm{L}} \tag{3.3}$$

where Γ is 210 $\mu C/cm_{Pt}^2$ [13] and L is the Pt loading in the electrode in $g_{Pt}/cm_{electrode}^2$ which is 0.5 mg/cm^2 for the tested samples. The ECSA in the Figure 3.11 is calculated to be 5.15 x 10^5 cm_{Pt}^2/g_{Pt}.

4 RESULTS AND DISCUSSION

4.1 A Novel Accelerated Stress Test for Carbon Corrosion

As mentioned in Chapter 2.7, the current ASTs focusing on the carbon corrosion are either performed under unrealistic conditions or takes so long. The following experiments are performed to design a new AST that induces faster carbon corrosion under real life operating conditions.

4.1.1 Ideal Flow Rate for ULF Mode

Figure 4.1: a) Bipolar plates and b) MEA for the 25 cm^2 cell

The bipolar plates with 1 mm rib width and 0.7 mm channel width are used for the dead ended operation (Figure 4.1). The performance curves taken at temperatures between 50 ℃ - 75 ℃ are shown in Figure 4.2. As the temperature goes higher than 65 ℃, the performance curves get worse.

After several hardware updates and try outs, the optimum parameters for a dead ended anode (DEA) mode were acquired.

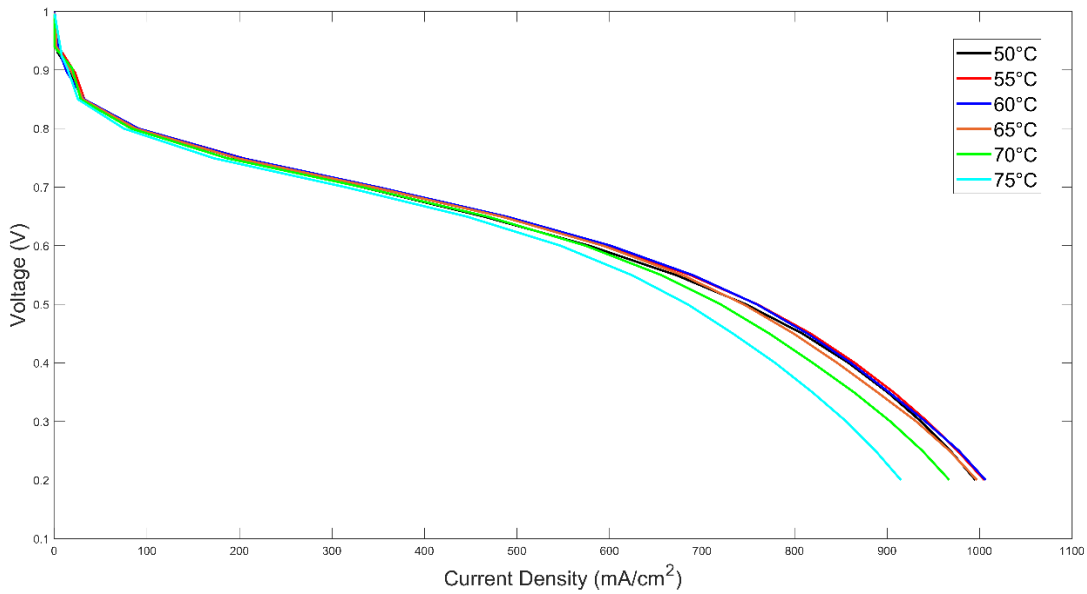

Figure 4.2: I-V curves taken at different temperatures

In Figure 4.3, the voltage transient for the DEA mode for 1 hour of operation is shown. The anode relative humidity (RH) was 25 % and the cathode RH was 100 %. The current density was 0.5 A/cm^2 and the temperature was 55 ℃.

The purge valve was opened for 1 second when the voltage dropped to 0.36 V. The duration of the DEA cycles was between 8 to 17 minutes at the beginning. The cycle duration stabilized around 17 minutes after a few hours.

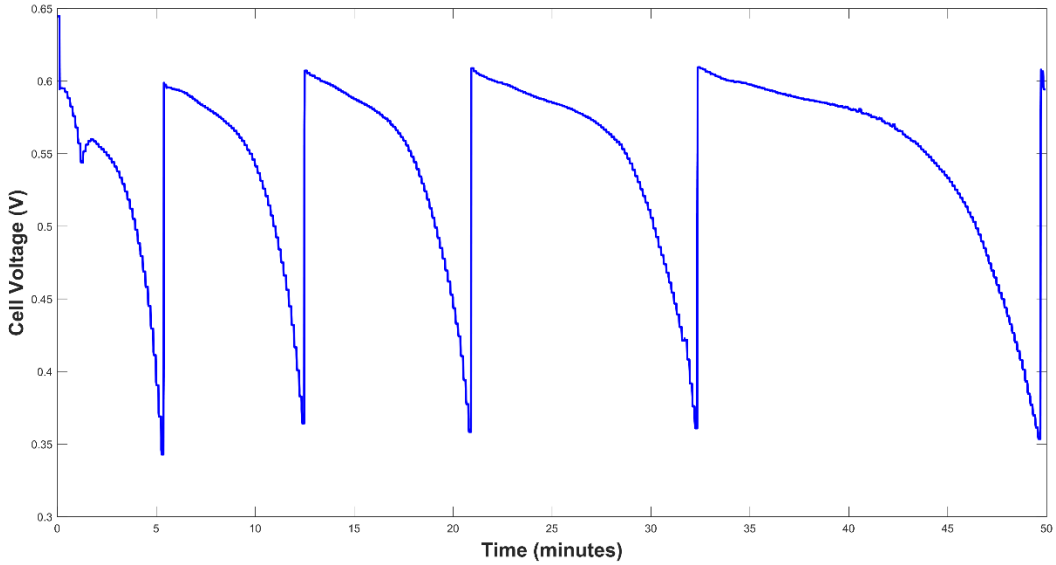

Figure 4.3: Voltage transient for the DEA operation for a 25 cm^2 cell

Obtaining a decent DEA cycle profile ensured that there is no leakage throughout the system. The next thing to ensure was the proper operation of the ultra-low flow system and the optimum flow parameters for this 25 cm^2 cell were acquired (Figure 4.4).

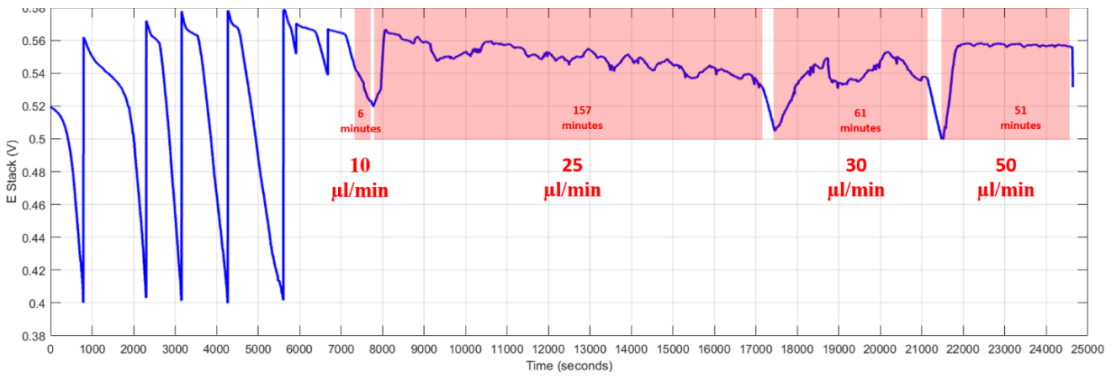

Figure 4.4: Voltage transient for the 25 cm^2 cell under DEA with ULF mode

After ensuring that the system went into DEA mode, several flow rates were tried. When the flow rate was 10 µl/min for 6 minutes, the voltage could not be recovered. The recovery showed itself when the flow rate was increased to 25 µl/min. However, the voltage continued to decrease for the following 157 minutes which concludes that 25 µl/min is not enough either.

The voltage started to show an almost stable trend when the flow rate was 30 µl/min. After keeping this rate for 1 hour, it was decided that a higher flow rate should be applied to get a decent stable voltage transient. When the flow rate was 50 µl/min, the voltage was convincingly stable after a smooth recovery. Therefore, the optimum ULF flow rate was set to 50 µl/min.

The hydrogen utilization at this flow rate is calculated as follows:

$$U = \frac{V_{reactant,consumed}}{V_{reactant,total}} \tag{4.1}$$

$V_{reactant,consumed}$ is calculated previously as 0.005578 L/min-A for 1,5 atm and 55 °C. For a current density of 0.5 A/cm^2 (12.5 A) this value will be 0.0697 L/min. If we assume the ultra-low flow rate is the wasted flow and is composed of totally hydrogen, $V_{reactant,total}$ will be $V_{reactant,total} = 0.005578 + 50 \text{ x } 10^{-6}$ L/min. Therefore, the utilization will be 0.99928. In other words, in this ultra-low flow regime, only % 0.07 or ‰ 0.7 of hydrogen is wasted at most.

The voltage drop at the end of 51 minutes ULF operation is due to the termination of the experiment.

4.1.2 Different Load Cycle Profiles Under ULF mode

The next step was to evaluate how the MEA responds to different load cycle profiles under ULF mode. A fresh MEA was conditioned and the reference data such as beginning-of-life (BOL) I-V curves, cyclic voltammograms (CV), electrochemically active surface area (ECSA) was extracted. To decide operation temperature to work at, the power density vs current curve was analyzed.

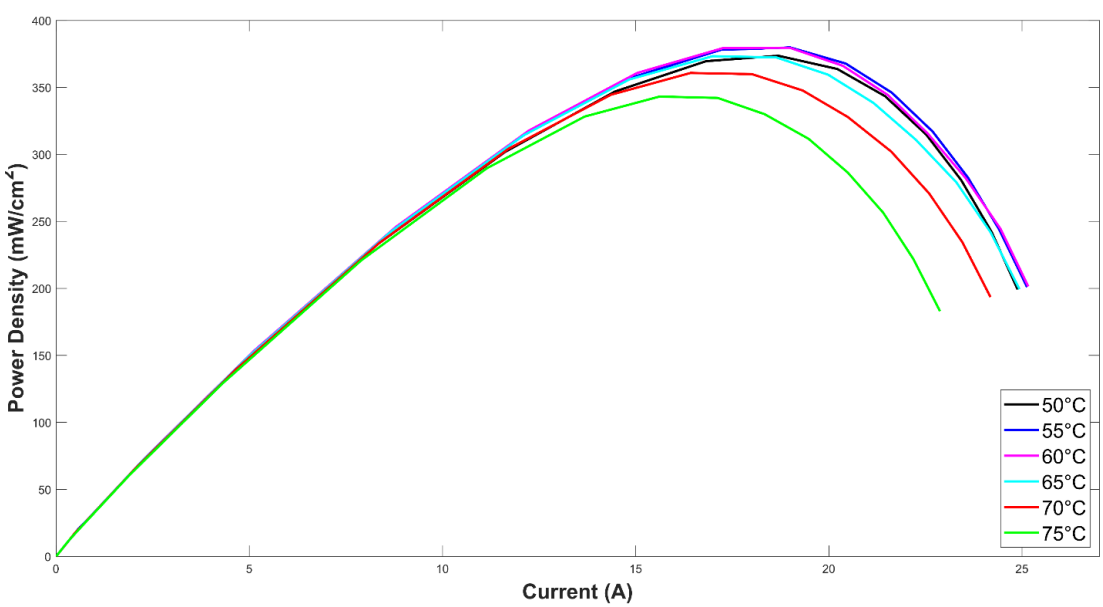

Figure 4.5: Power density (mW/cm^2) vs current (A) curve for a fresh 25 cm^2 MEA

In Figure 4.5, the flow rates were 0.26 l/min for hydrogen and 1 l/min for air. The relative humidity (RH) was 100 % for both anode and cathode with an atmospheric backpressure. The highest power density yield was at 55 ℃ and 60 ℃. However, the low temperature option was chosen, mainly because of the polypropylene syringe. Because the syringe is heated to eliminate the syphoning effect and the maximum temperature at which the syringe holds its structural integrity is 50 ℃.

The summary of the load cycle profiles applied is shown in Figure 4.6. The details about these profiles are explained below.

#	Temperature (C)	ULF rate (ul/min)	RH (%)	Cycle Profile	Duration (hours)
1	55	50	25 Anode 75 Cathode	1-from 0,96 A/cm^2 to 0,32A/cm^2 2-from 0,32 A/cm^2 to 0,96A/cm^2 3-10 minutes at 0,96 A/ccm^2 70 min per cycle 4-5 minutes at open circuit	240
2	55	30	25 Anode 75 Cathode	1-from 0,96 A/cm^2 to 0,32A/cm^2 2-from 0,32 A/cm^2 to 0,96A/cm^2 3-10 minutes at 0,96 A/cm^2 70 min per cycle 4-5 minutes at open circuit	96
3	55	50	25 Anode 100 Cathode	Constant at 0,6 A/cm^2 Syringe pump activates at 0,43V and stops at 0,51 V	48
4	55	50	25 Anode 100 Cathode	Constant at 0,08 A/cm^2 Syringe pump activates at 0,7 V and stops at 0,75 V	32
5	55	50	25 Anode 100 Cathode	1- Constant at 0,08 A/cm2 for 60 h 2- Constant V at 0,5 V for 2,5 h and constant J at 0,16 A/cm^2 for 10 h	70
6	55	50	25 Anode 100 Cathode	Constant V at 0,475 V for 3 h and constant J at 0,16 A/cm^2 for 15 h	18

Figure 4.6: Summary of all the cycle profiles applied

Profile 1:

This profile was designed to see the MEA response operating on a cycle which has: 1) an increasing power demand, 2) a decreasing power demand, 3) a maximum power demand for a while 4) idle (no demand) for a while. So, the applied cycle was composed of 4 steps:

1-From 0.96 A/cm^2 to 0.32 A/cm^2 with 0.025 A/cm^2 per minute

2-From 0.32 A/cm^2 to 0.96 A/cm^2 with 0.025 A/cm^2 per minute

3-10 minutes at 0.96 A/cm^2

4-5 minutes at OCV

Figure 4.8 shows these steps on a current vs time plot. One cycle was about 70 minutes. The cell operated under continuous ULF mode with 50 µl/min flow rate. The RHs were the same as the DEA mode, which were 25 % for the anode and 100 % for the cathode. This profile was run for a total of 240 hours. CVs are taken every 20 hours.

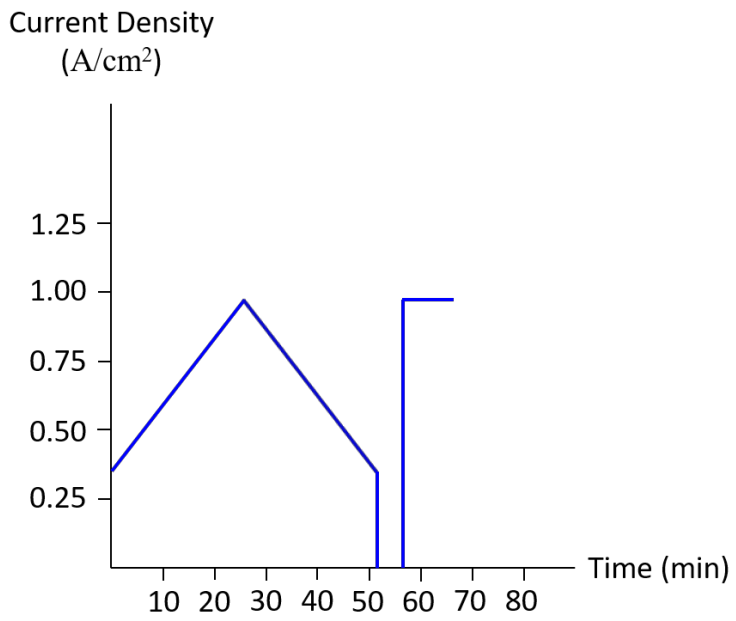

Figure 4.7: Current vs time plot for the cycle profile 1

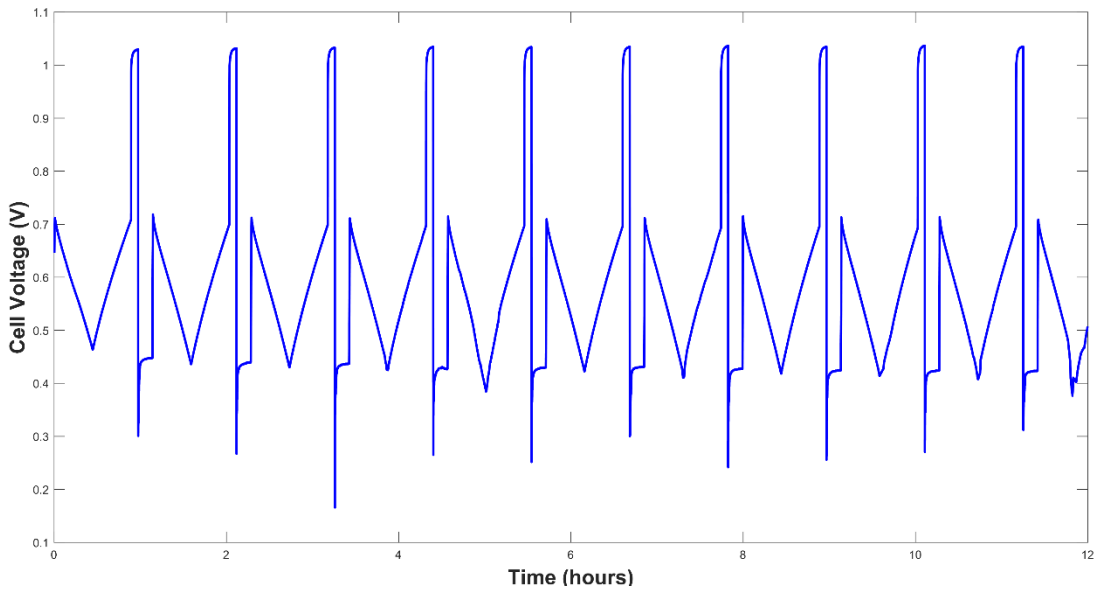

Figure 4.8: Part of the voltage transient during operation under cycle profile 1

The voltage was almost stable, ensuring that the amount of withdrawal (50 µl/min) was enough to maintain such a load cycle profile.

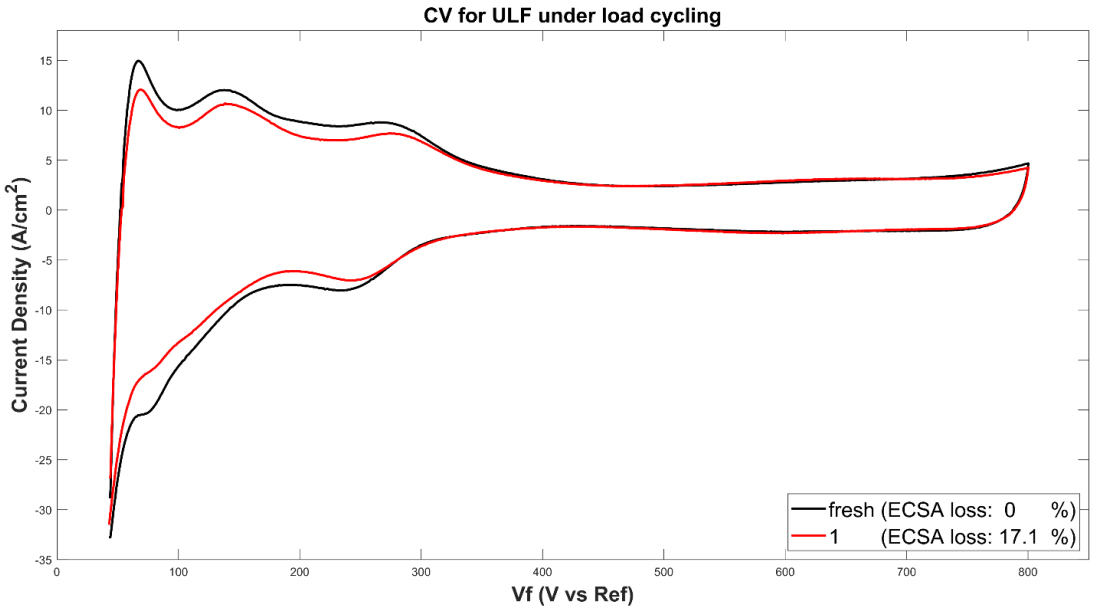

Figure 4.9: Comparison of the cyclic voltammograms for the fresh MEA and 240 h of operation under cycle profile 1

The resulting ECSA loss can be seen in Figure 4.9. The overall ECSA loss was 17.1 %, which is far away from the DOE criterion of degradation which is 40 % loss in ECSA.

Profile 2:

This profile was designed to see what happens when the MEA operates on exactly the same load cycle as in cycle profile 1 but with a lower ULF rate. The flow rate was set to 30 µl/min.

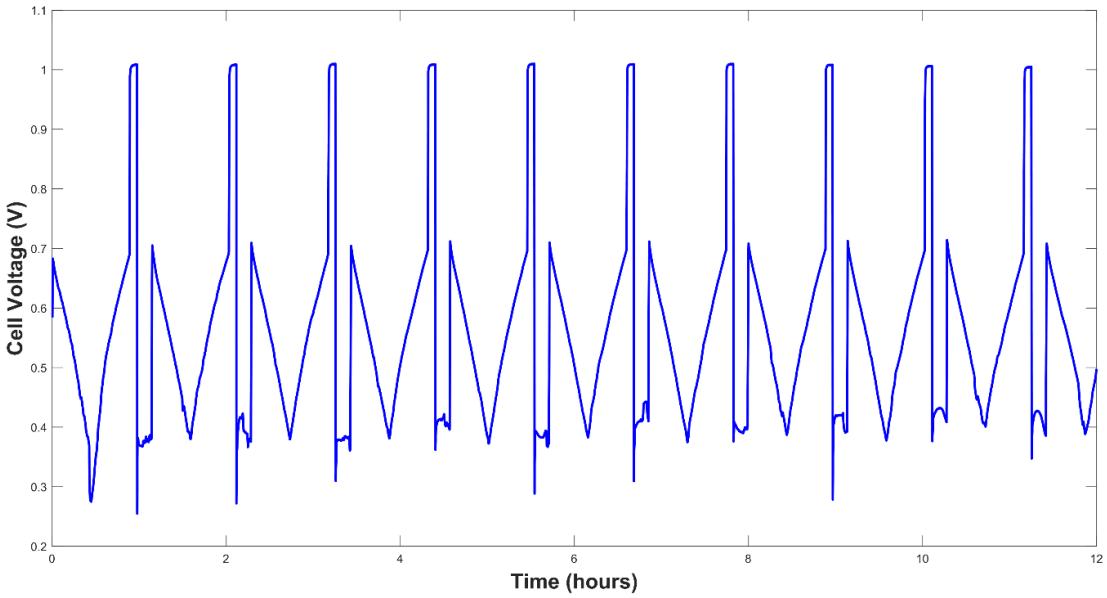

Figure 4.10: Part of the voltage transient during operation under cycle profile 2

The voltage was stable, but not as stable as that of profile 1. However, as seen in the first ULF trials, the flow rate is good enough to maintain this load profile.

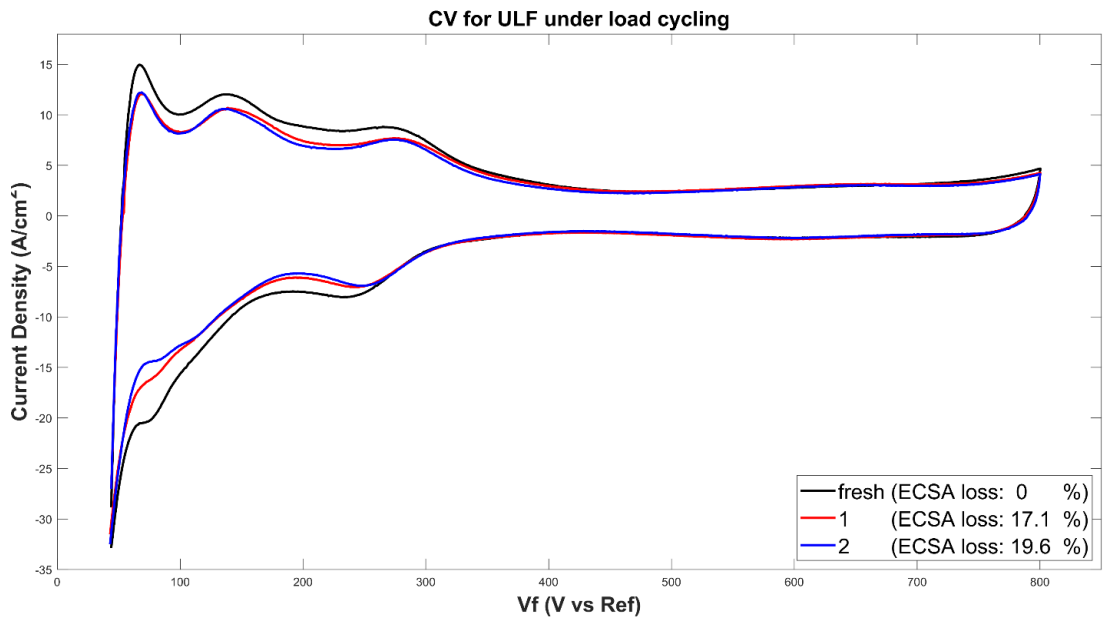

Figure 4.11: Comparison of the cyclic voltammograms for the fresh MEA, 240 h of operation under cycle profile 1 and 96 h of operation under cycle profile 2

The cumulative ECSA loss was calculated to be 19.6 % after the second load cycle profile, still far away from the DOE target. The rate of loss was slow even though this profile was run for 96 h. We needed to find a faster way to degrade the carbon support, so another load cycle profile was tried.

Profile 3:

In order to accelerate the carbon corrosion, the cell is forced to work at a local fuel starvation regime continuously. To perform this, a constant current density of 0.6 A/cm^2 was drawn. The ULF pump is programmed to be triggered when the voltage is below 0.43 V with 50 µl/min withdrawal rate. The pump is programmed to stop when the voltage recovered back to 0.51 V. This profile was run for 48 h.

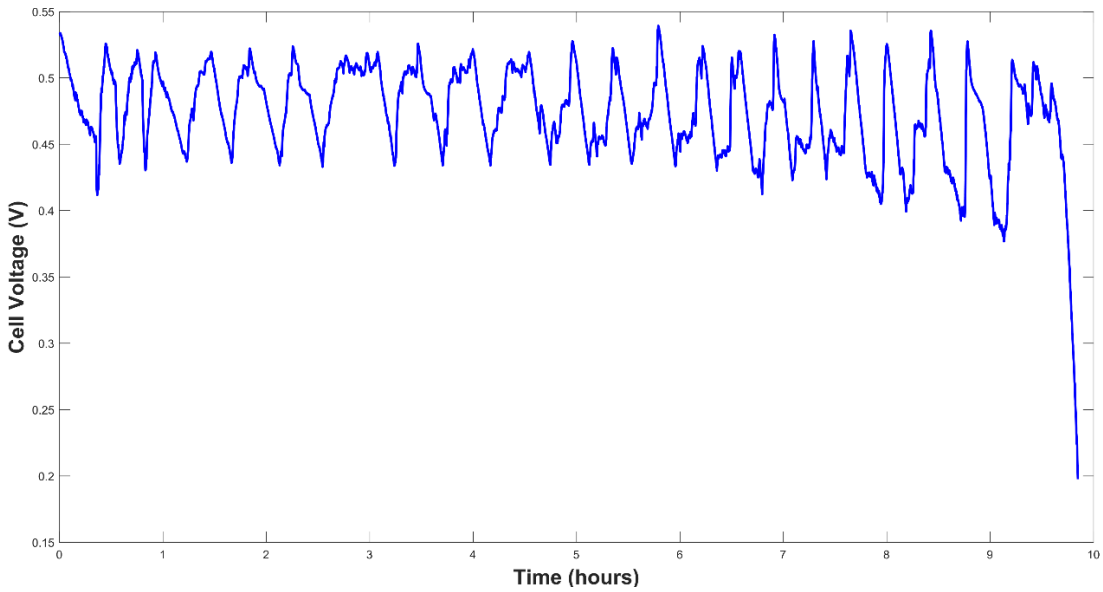

Figure 4.12: Last 10 hours of the voltage transient during operation under cycle profile 3

Towards the end of the voltage transient (Figure 4.12), some irregularities started to show up, probably due to the accumulated water in the anode.

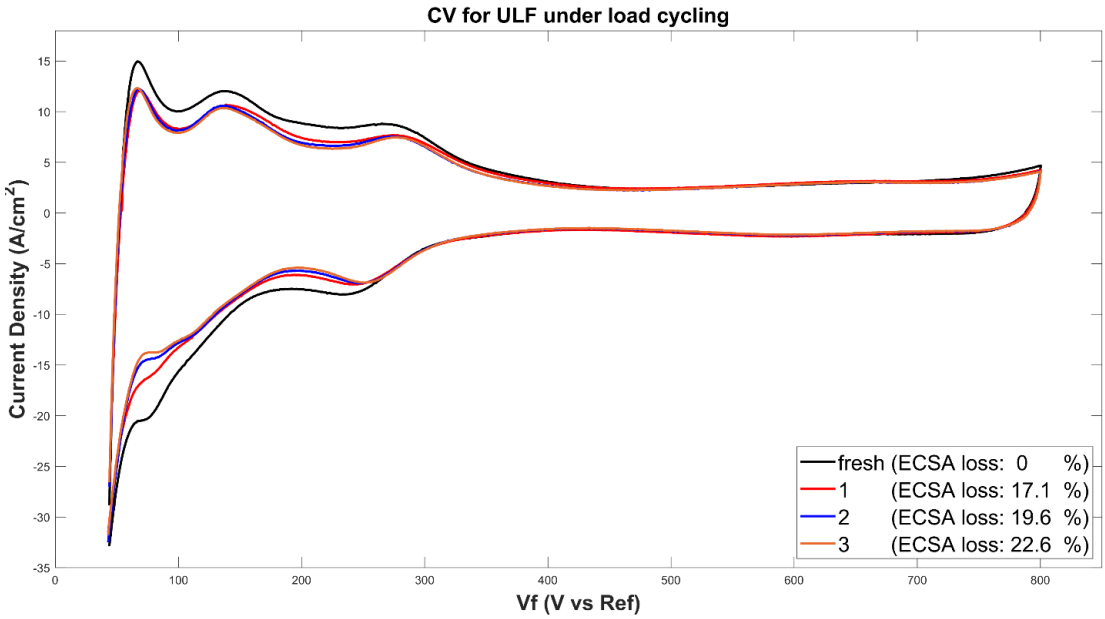

Figure 4.13: Comparison of the cyclic voltammograms for the fresh MEA, 240 h of operation under cycle profile 1, 96 h of operation under cycle profile 2 and 48 h of operation under cycle profile 3

Although the degradation rate was still low, the amount of carbon oxidation was better than the cycle profiles applied previously especially considering the duration. The amount of extra loss in the ECSA confirmed that forcing the cell to work in a fuel starved regime promotes carbon corrosion better than load cycling. This is why the remaining of the profiles focused on local fuel starvation regime.

Profile 4:

To increase the area that goes through local fuel starvation, a smaller current is drawn with a current density of 0.08 A/cm^2. Furthermore, to increase the fuel starvation duration, the trigger voltages are selected closer to each other. In other words, the pump was programmed to start working when the voltage was below 0.7 V and end when it recovers to 0.75 V. The flow rate was again 50 µl/min. The total duration of this profile was 32 hours.

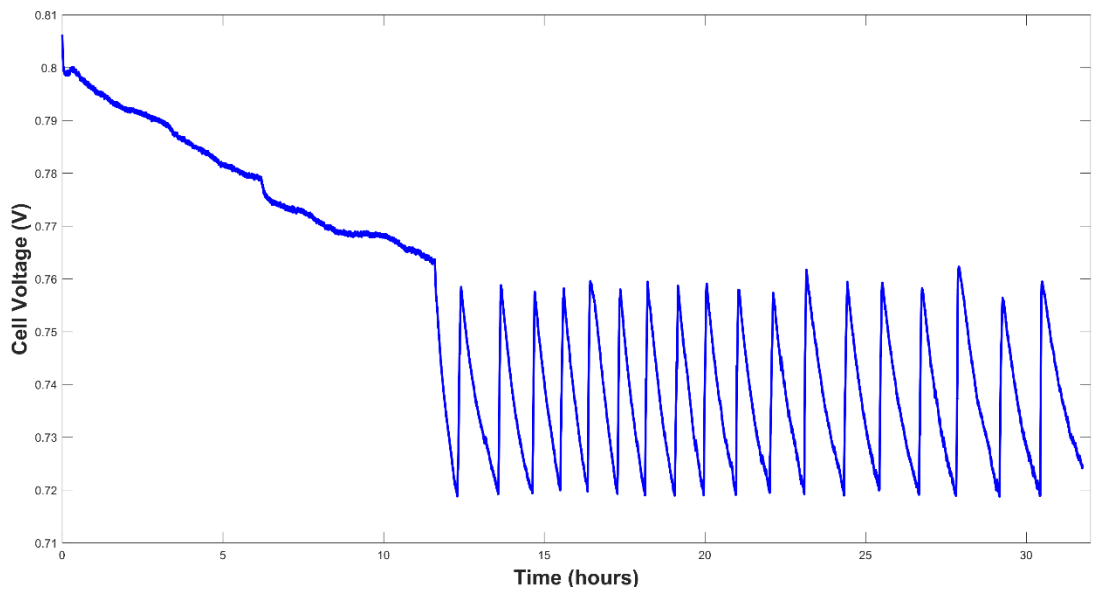

Figure 4.14: 32 hours of the voltage transient during operation under cycle profile 4

It took more than 12 hours for the nitrogen and water to accumulate into the anode bipolar plates and induce the fuel starvation mode. This was something expected and done on purpose as mentioned above.

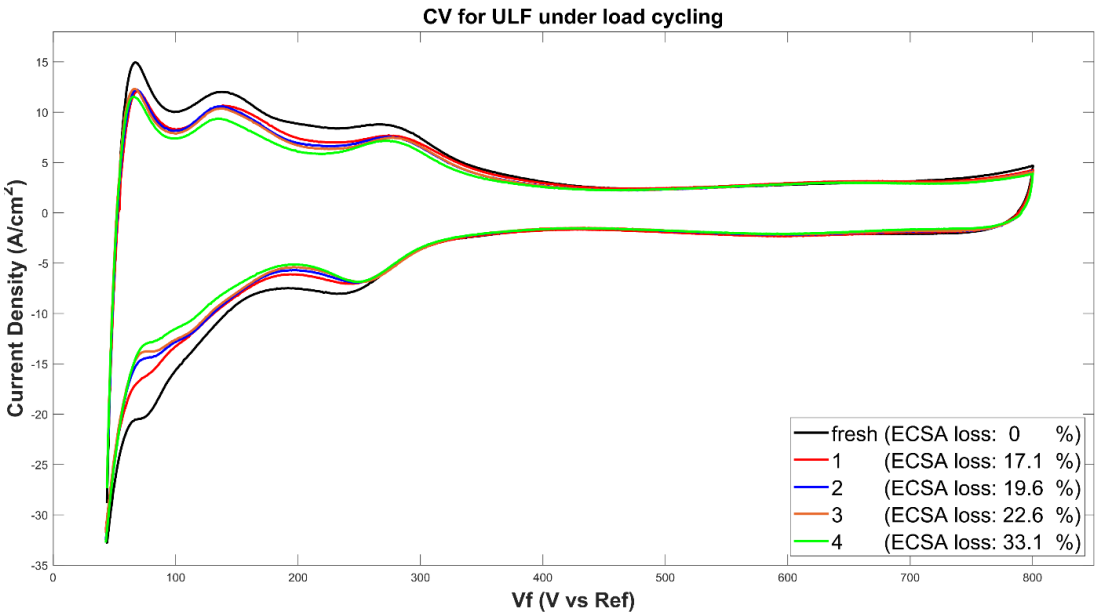

Figure 4.15: Comparison of the cyclic voltammograms for the fresh MEA, 240 h of operation under cycle profile 1, 96 h of operation under cycle profile 2, 48 h of operation under cycle profile 3 and 32 h of operation under cycle profile 4

The cumulative ECSA loss reached to 33.1 % with an increase of 10.5 % with respect to the previous cycle profile. This is the highest increase in the corrosion rate considering the duration of the operation. In fact, the reason for such a fast carbon oxidation was mentioned and will be re-discussed after reporting the remaining cycle profiles.

The result above raised a question: is this the first 12 h part or the voltage cycling part that contributed most to the degradation? In the next profile, the first constant current density part was isolated to see the effects on the carbon corrosion.

Profile 5:

The same current density as profile 4, 0.08 A/cm^2 was drawn for 60 hours. The syringe pump was also deactivated to see if the voltage decreases all the way through zero. However, as shown in Figure 4.16, the voltage was stabilized around 0.7 V. The nitrogen and water that diffused to the anode and the water that was dragged to the cathode reached to an

equilibrium. Also, only a small portion of the cell is active as the most parts are blanketed by nitrogen and liquid water.

Then, to see if the same equilibrium will be reached for a higher current density, the current was doubled (0.16 A/cm^2) after a purge. But first, to shorten the duration that is needed to reach the equilibrium, the voltage was kept at 0.5 V until the current stabilizes. This time, the voltage was stabilized around 0.48 V.

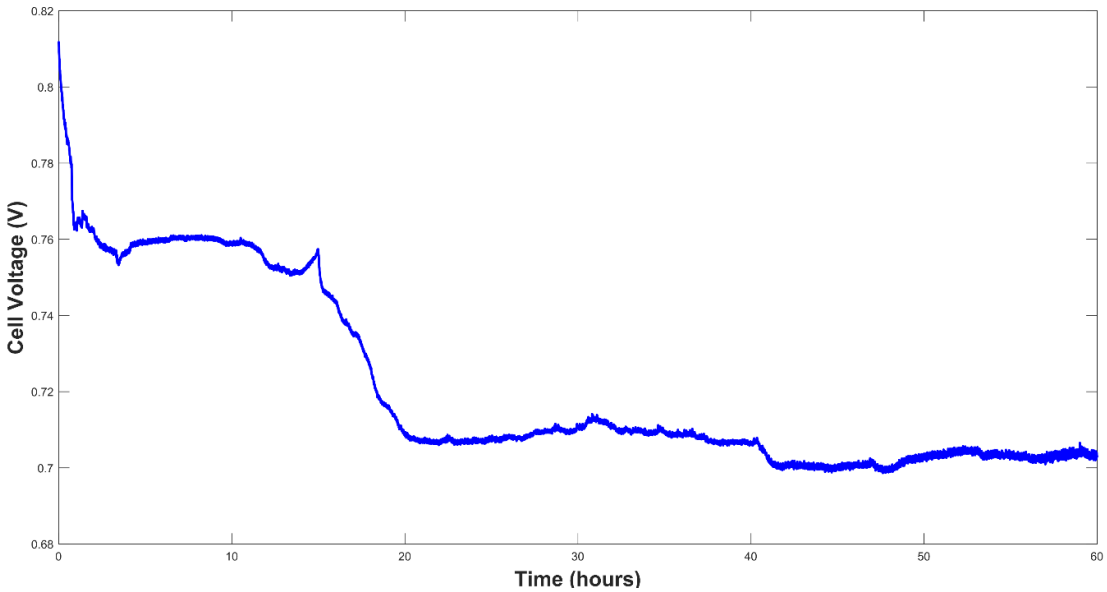

Figure 4.16: First 60 hours of the voltage transient during operation under cycle profile 5

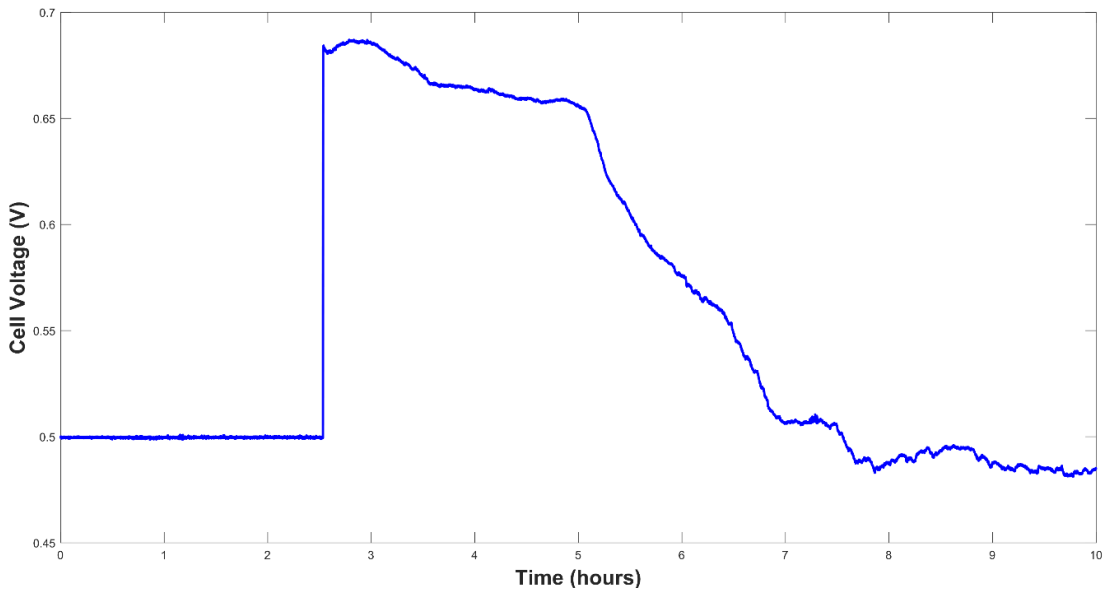

Figure 4.17: Last 10 hours of the voltage transient during operation under cycle profile 5

The equilibrium was reached again. In the end, cycle profile 5 was a 70 h repetition of the first part of the profile 4.

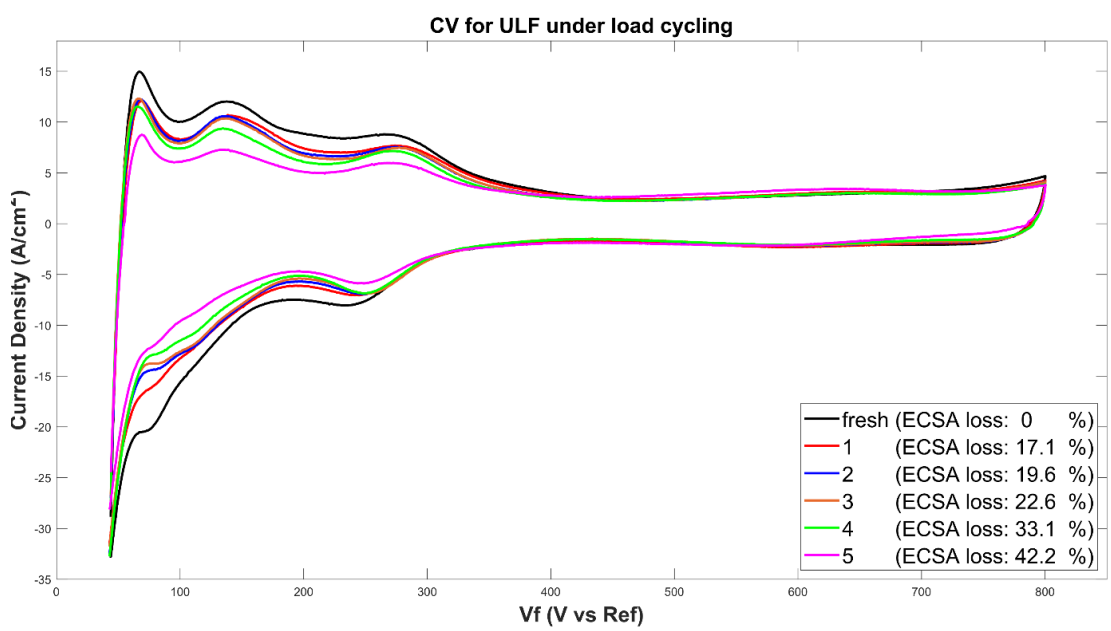

Figure 4.18: Comparison of the cyclic voltammograms for the fresh MEA, 240 h of operation under cycle profile 1, 96 h of operation under cycle profile 2, 48 h of operation under cycle profile 3, 32 h of operation under cycle profile 4 and 70 h of operation under cycle profile 5

The contribution to the overall ECSA loss was less than profile 4, considering the cycle duration. This suggests that the voltage cycling part was more effective than the voltage stabilization part in profile 4.

The 9 % extra loss in profile 5 is also big compared to the second and third cycle profiles.

Profile 6:

A current density of 0.16 A/cm^2 was drawn for 18 hours. Similar to the profile 5, the voltage was held constant at 0.475 V until the current stabilized and then the constant current regime was applied. This cycle profile was only aimed to show if a current density of 0.16 A/cm^2 has a huge effect on a possible faster carbon corrosion.

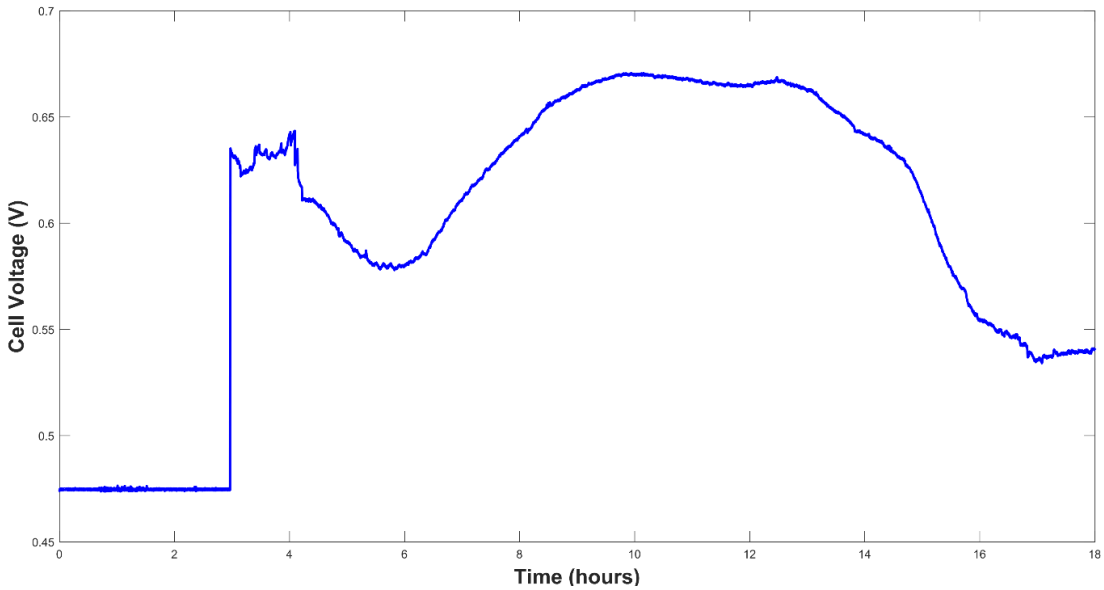

Figure 4.19: 18 hours of the voltage transient during operation under cycle profile 6

The voltage stabilized at around 0.53 V after a very odd path. However, up until this profile, the overall ECSA was already dropped to 42.2 % meaning that most of the carbon was oxidized and from the SEM images in the next session, even the carbon of the MPL was

corroded. This means, some of the hydrophobicity on the electrode is lost and the water is poorly managed. Therefore, this odd behavior in the voltage transient can be attributed to the overall degradation and resulting water flooding.

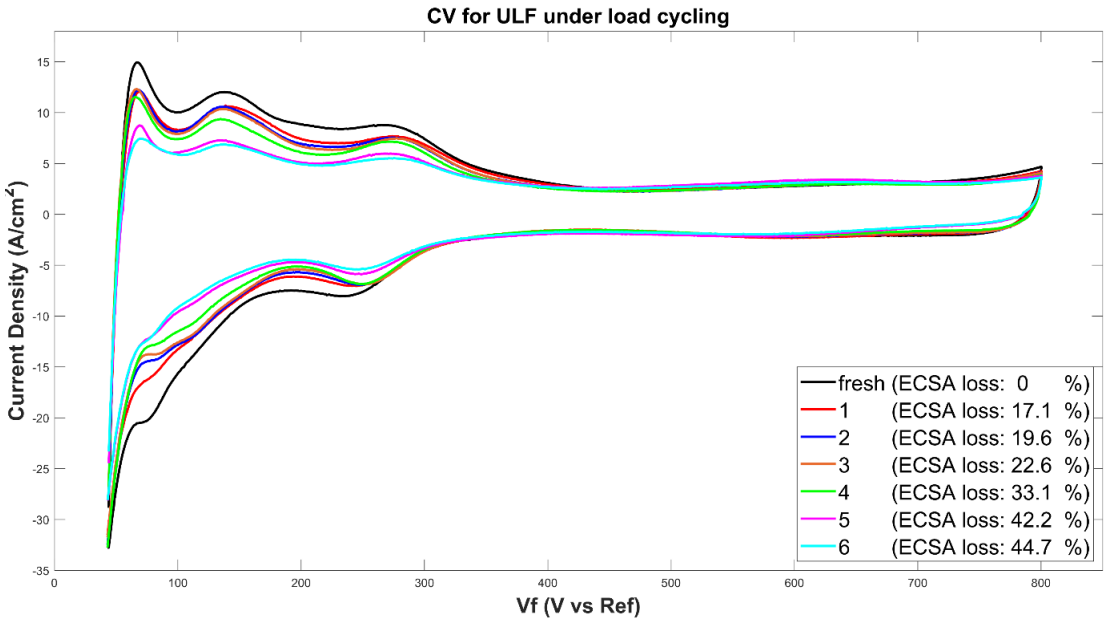

Figure 4.20: Comparison of the cyclic voltammograms for the fresh MEA, 240 h of operation under cycle profile 1, 96 h of operation under cycle profile 2, 48 h of operation under cycle profile 3, 32 h of operation under cycle profile 4, 70 h of operation under cycle profile 5 and 18 h of operation under cycle profile 6

The overall ECSA loss increased by 2.5 % and judging by the duration, it is not as fast as cycle profile 4.

To better see the effects of each cycle profile, a summary of the profiles and a time evolution of the cumulative ECSA loss was given below.

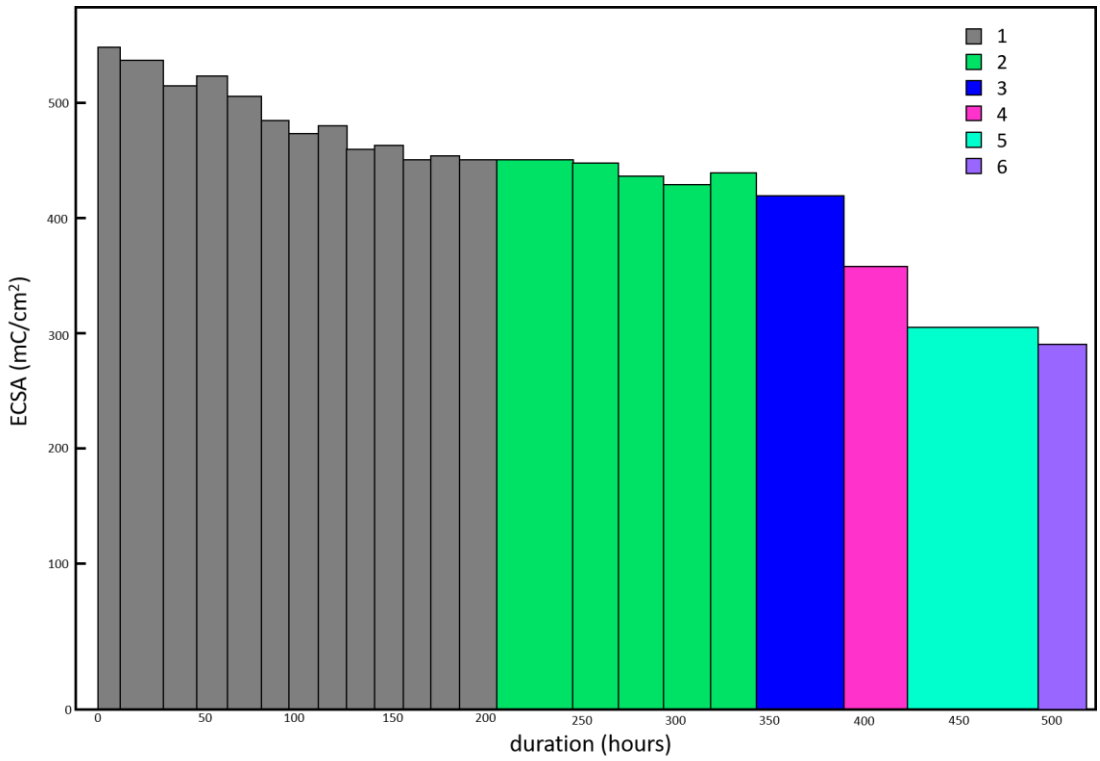

Figure 4.21: Time evolution of the ECSA loss after each cycle profile

4.1.3 Post-Mortem Analysis of the MEA under SEM

The final MEA was removed from the fuel cell fixture and analyzed under Scanning Electron Microscope (SEM). The MEA was dissected into 25 pieces and only some parts that can sample the inlet, outlet and middle part of the MEA are shown in Figure 4.22.

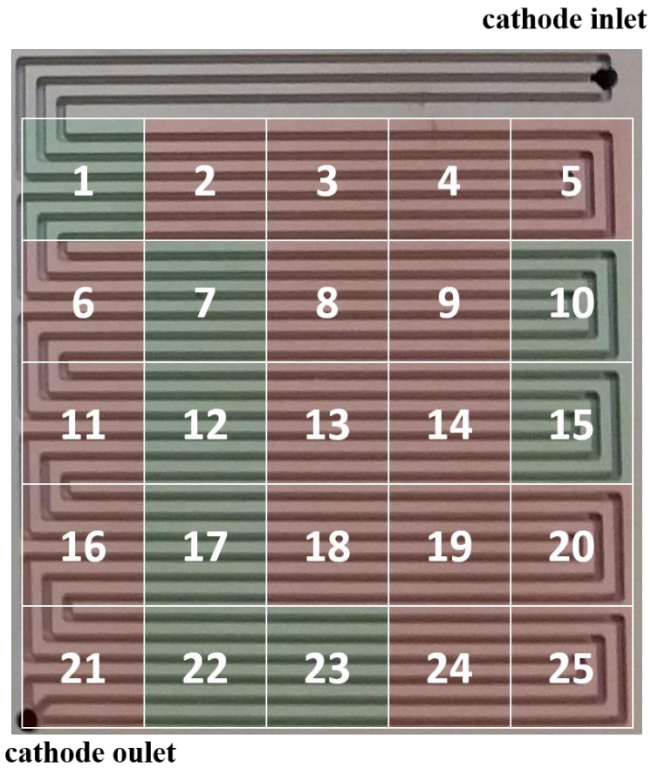

Figure 4.22: Dissection plan and analyzed sections (in green) of the MEA for SEM analysis

A total of 8 different pieces were imaged under SEM. To make sure of any possible anomaly, two pieces from the near-outlet region are selected. Since the structure of number 17 is similar to those from the near-outlet region, no other pieces were analyzed from this row. Due to some transitions in the structure, 2 pieces were selected for the middle region. For the same reason, again two pieces were selected from the second row. Since there were no delamination for the number 7 and 10, only one piece was selected for the near-inlet region. The reason for not selecting the pieces on the edges such as number 16 and number 21 is because these pieces were delaminated and cracked during sample preparation.

In all the SEM images below (Figure 4.23), the anode is on top and the cathode is in the bottom. Furthermore, during the SEM sample preparation, the GDLs delaminated from the membrane which is the reason for the sandwich-like look in some of the images. The delamination occurred because of the swelling of the nafion membrane during operation.

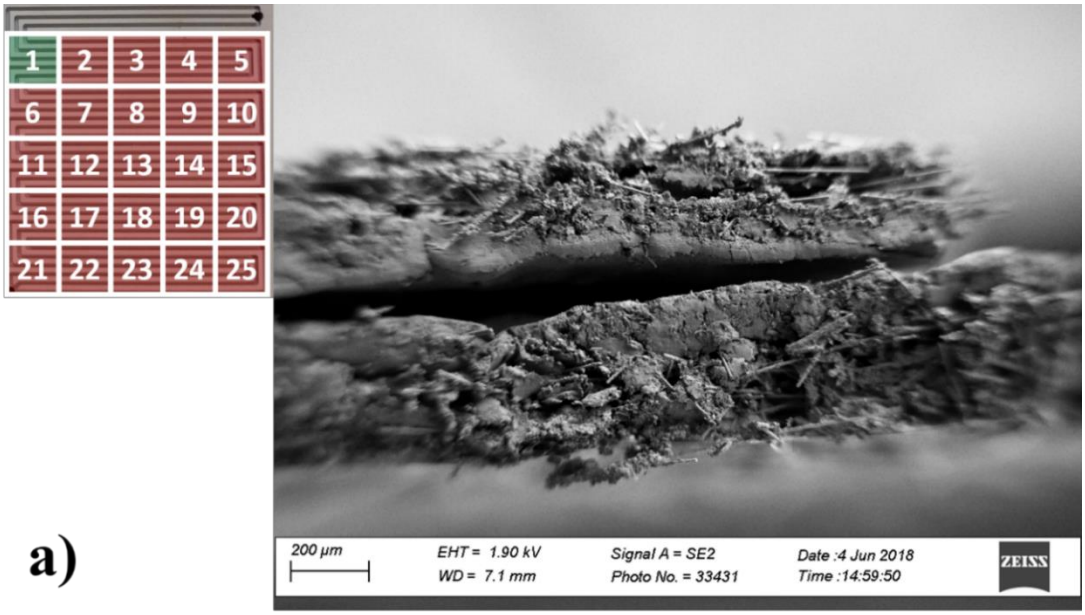
1 2 3 4 5
6 7 8 9 10
11 12 13 14 15
16 17 18 19 20
21 22 23 24 25
200 µm
EHT = 1.90 kV
WD = 7.1 mm
Signal A = SE2
Photo No. = 33431
Date :4 Jun 2018
Time :14:59:50
ZEISS

a)

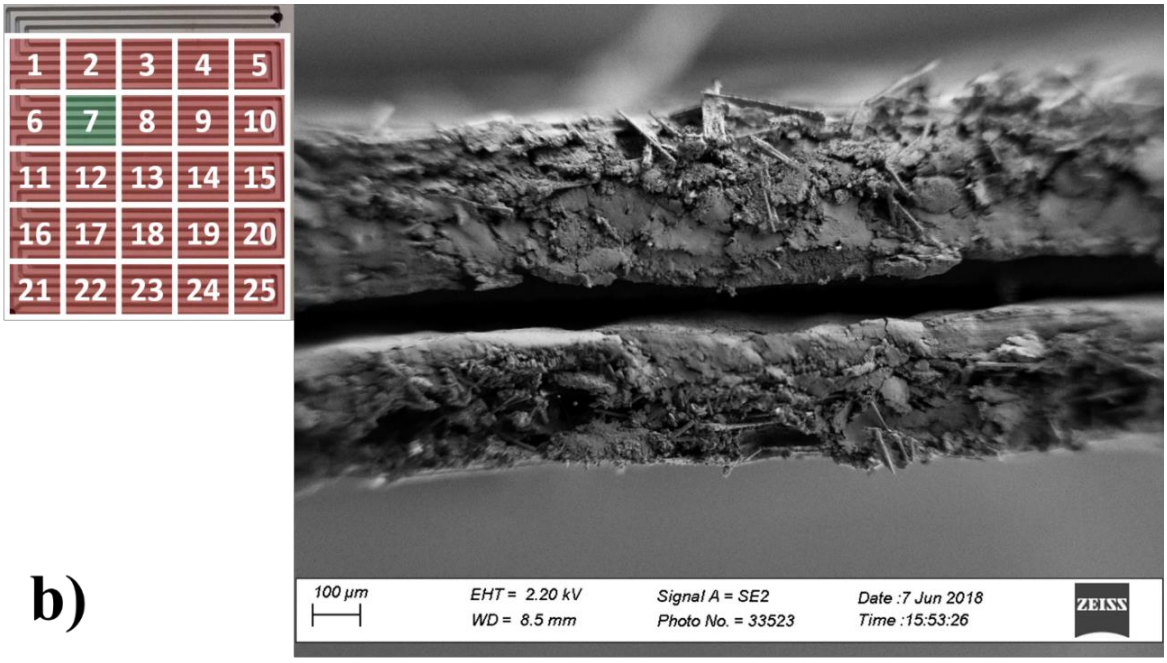
1 2 3 4 5
6 7 8 9 10
11 12 13 14 15
16 17 18 19 20
21 22 23 24 25
100 µm
EHT = 2.20 kV
WD = 8.5 mm
Signal A = SE2
Photo No. = 33523
Date :7 Jun 2018
Time :15:53:26
ZEISS

b)

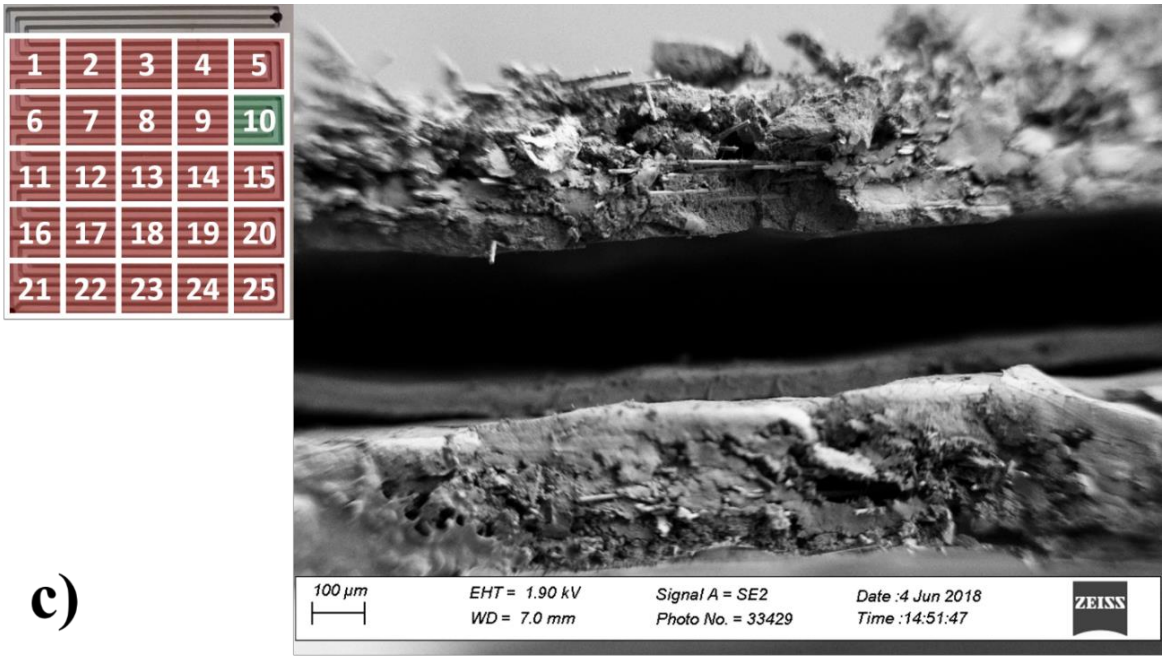
1 2 3 4 5
6 7 8 9 10
11 12 13 14 15
16 17 18 19 20
21 22 23 24 25
100 µm
EHT = 1.90 kV
WD = 7.0 mm
Signal A = SE2
Photo No. = 33429
Date :4 Jun 2018
Time :14:51:47
ZEISS

c)

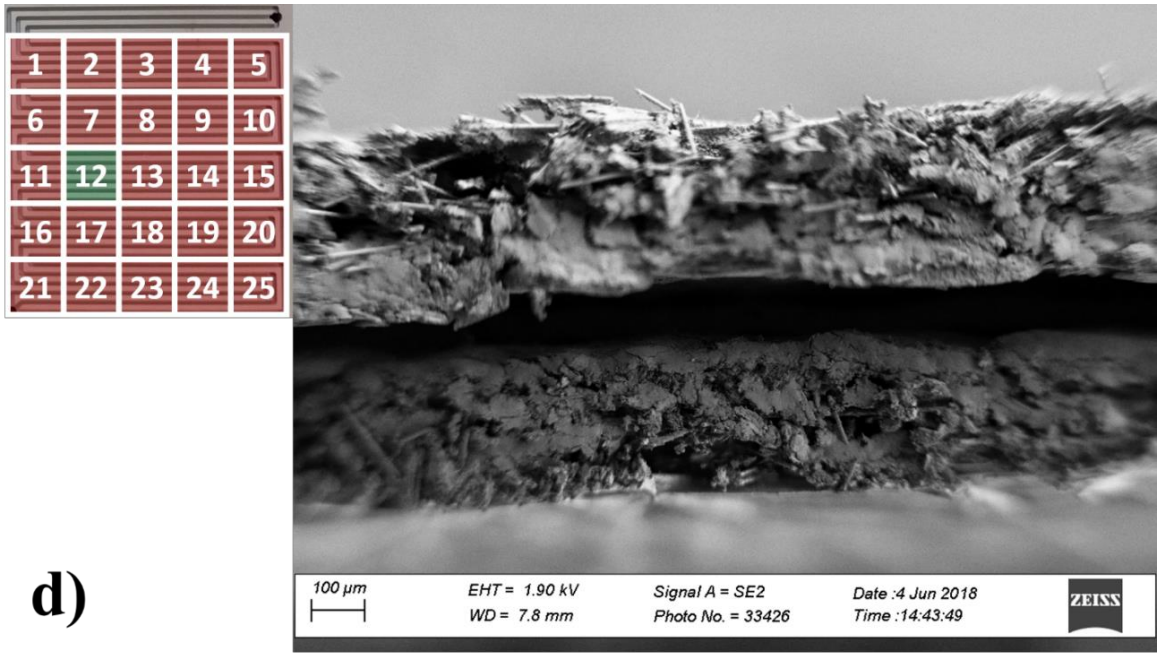
1 2 3 4 5
6 7 8 9 10
11 12 13 14 15
16 17 18 19 20
21 22 23 24 25
100 µm
EHT = 1.90 kV
WD = 7.8 mm
Signal A = SE2
Photo No. = 33426
Date :4 Jun 2018
Time :14:43:49
ZEISS

d)

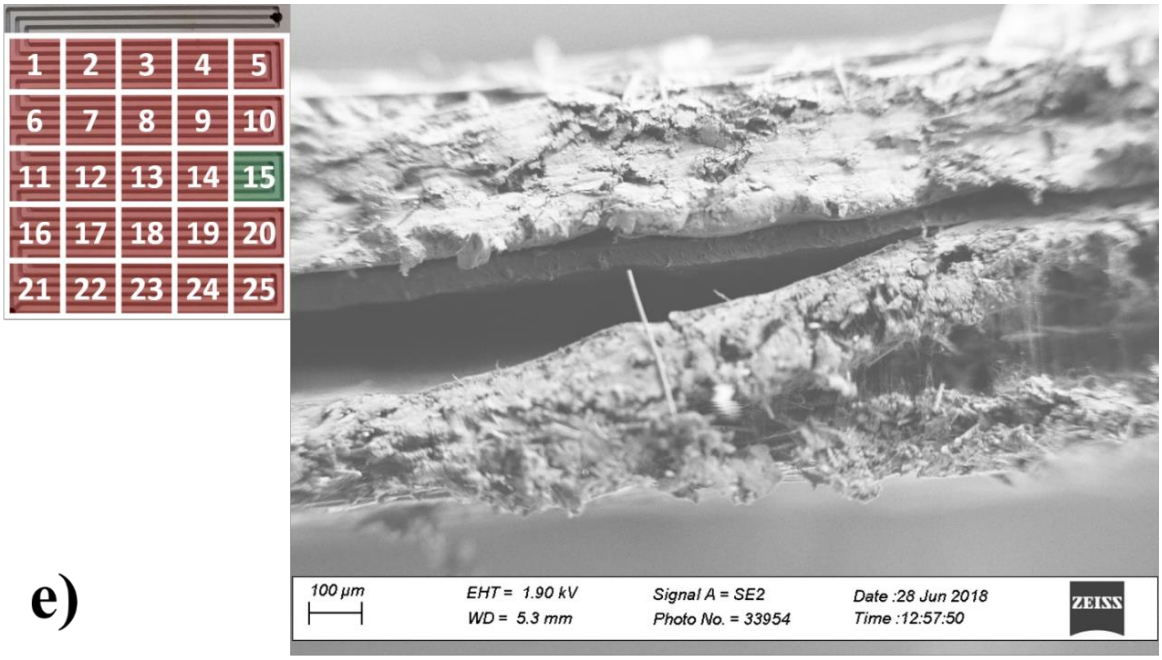
1 2 3 4 5
6 7 8 9 10
11 12 13 14 15
16 17 18 19 20
21 22 23 24 25
100 µm
EHT = 1.90 kV
WD = 5.3 mm
Signal A = SE2
Photo No. = 33954
Date :28 Jun 2018
Time :12:57:50
ZEISS

e)

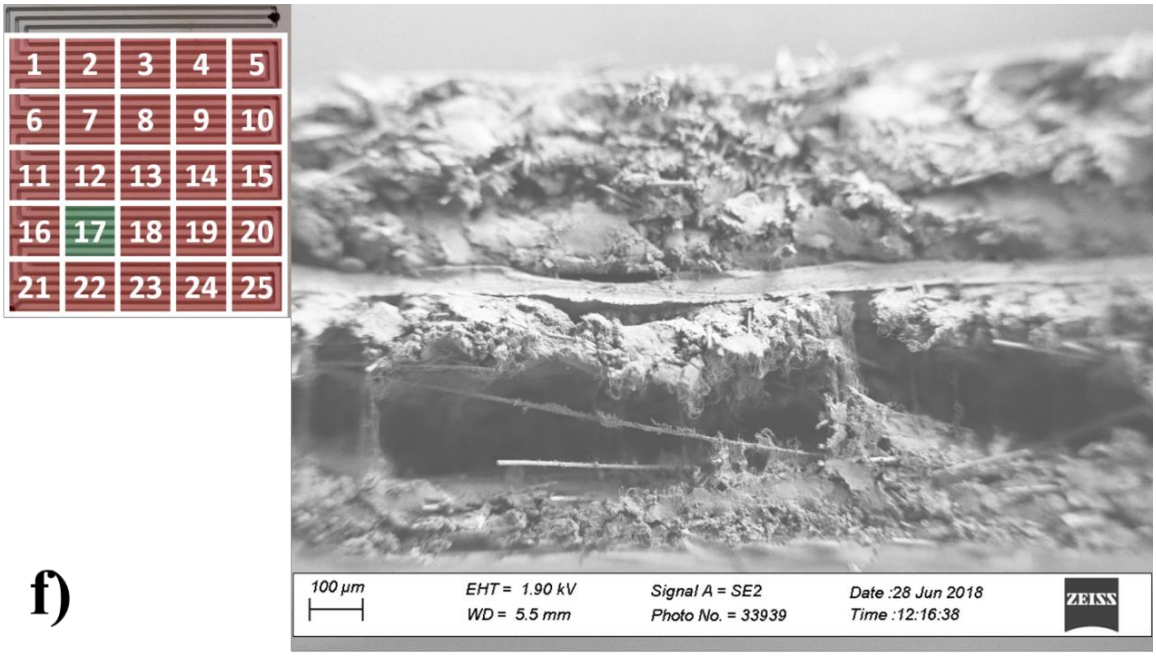
1 2 3 4 5
6 7 8 9 10
11 12 13 14 15
16 17 18 19 20
21 22 23 24 25
100 µm
EHT = 1.90 kV
WD = 5.5 mm
Signal A = SE2
Photo No. = 33939
Date :28 Jun 2018
Time :12:16:38
ZEISS

f)

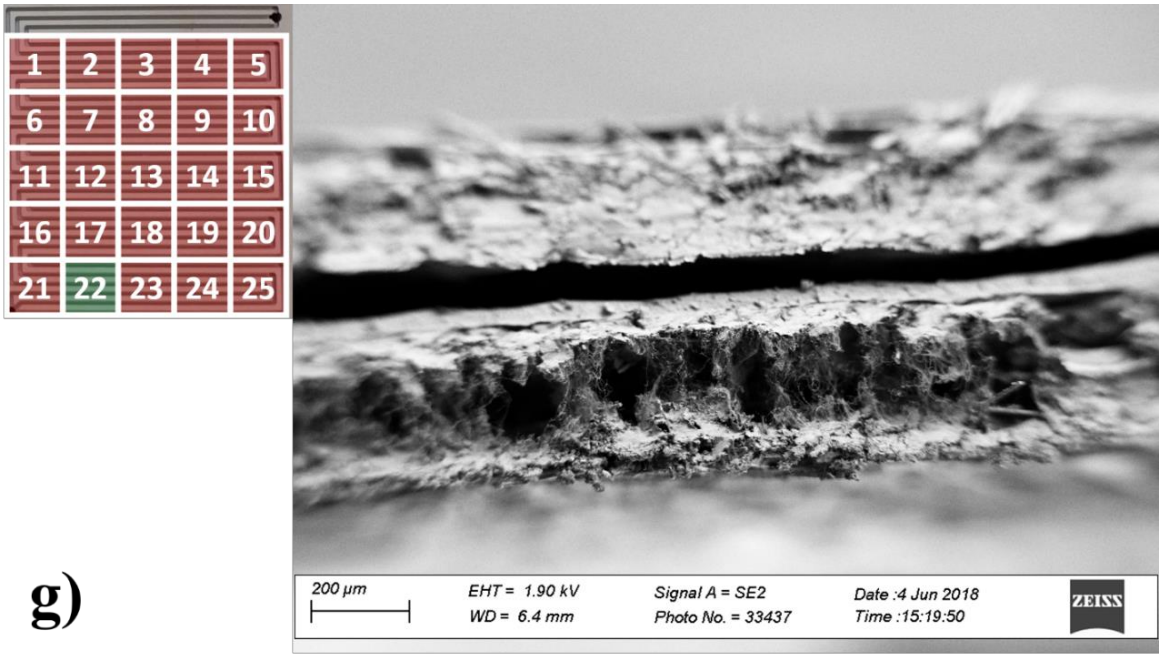

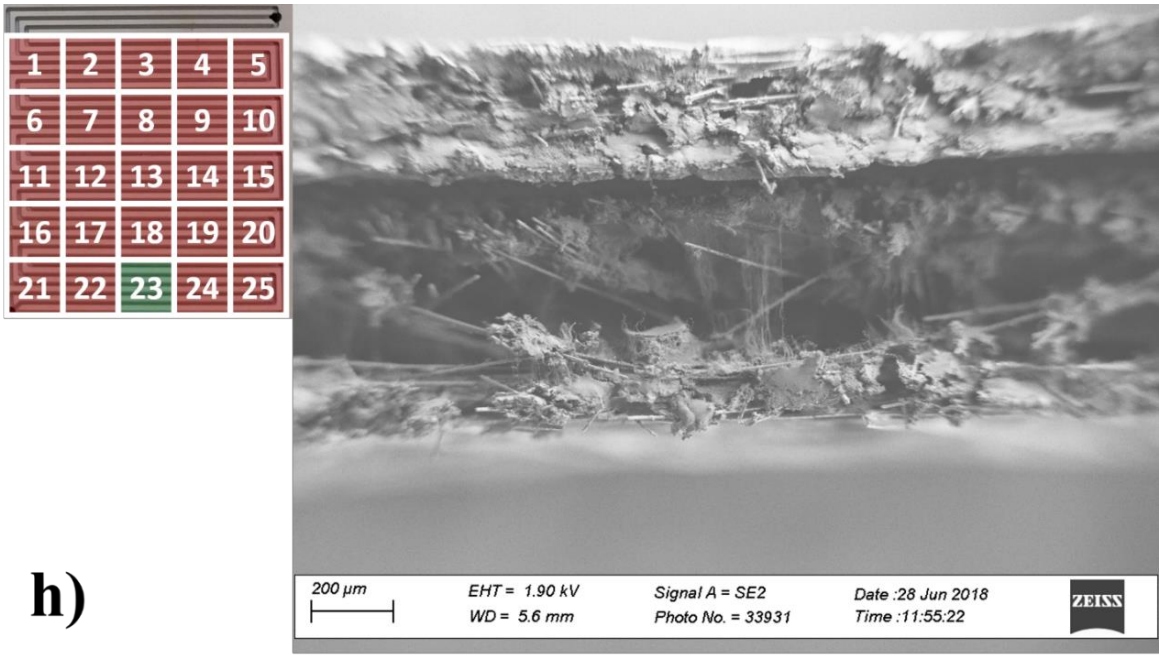

Figure 4.23: SEM images of the dissected MEA after carbon corrosion study. a) section number 1, b) section number 7, c) section number 10, d) section number 12, e) section number 15, f) section number 17, g) section number 22, h) section number 23

4.1.4 Discussion

The cycle profiles were performed to find a fast and real-life-operation AST that can be used to find new materials that are durable against the harsh operating conditions such as dead-ended or near-dead-ended modes of operation. The cyclic voltammograms are useful in evaluating the degree of carbon corrosion because the ECSA that is calculated from the CV data gives information on how much of the MEA can actively contribute to current generation.

Judging by the duration, the cycle profile 4 gave the fastest carbon corrosion for the 25 cm^2 MEA used in this part of the study. Previously, in Chapter 2.5 and 2.6, it was mentioned that cycling the voltage between 0.7 V and 1.0 V vs RHE first fully covers the Pt surface with Pt-oxide which blankets the Pt surface and then reduces the Pt surface. This instantaneous restructuring of the Pt surface by the repeated reduction and oxidation of Pt nanoparticles, catalyzes the process of carbon corrosion. In cycle profile 4, during the first part where the voltage is stabilized around 0.76 V, the cathodic voltage rises because of the local fuel starvation. As a result, the voltage at the cathode can be high enough to fully oxidize the Pt surface. When the pump is triggered and the accumulated water and nitrogen in the anode "slightly" purged by applying an ultra-low flow, the cathode potential drops back to below 0.98 V vs RHE where the reduction of the Pt surface can take place. Thus, cycle profile 4 can be employed as a new AST for fast carbon corrosion that works under realistic operating conditions.

The SEM images not only confirm the carbon support degradation, but also show what happens when a catalyst coated GDL experience electrochemical oxidation of carbon. Looking at the dissected pieces, there is a delamination in the GDL. One possible explanation could be using a catalyst coated GDL instead of catalyst coated membrane. When the GDL is sprayed with the catalyst ink, some portion of the ink diffused into the MPL and interfaced with the macro-porous layer of the GDL. During the operation, due to the existence of the water vapor that comes with the high relative humidity, the carbon corrosion started at this interface and caused the delamination. At the portions of the cathode which are close to the

outlet, the effect of carbon corrosion is maximum. The same delamination can be seen even at portions far away from the outlet, such as section 15. This suggests that the fuel starved region reached almost to the middle of the cathode. In other parts where the carbon corrosion does not exist, the microporous structure of the carbon paper can be seen.

4.2 Effect of Ultra-Low Flow Operation to MEA Durability

In Section 4.1, it was calculated that only % 0.07 or ‰ 0.7 of hydrogen is wasted when operating under ultra-low-flow (ULF) mode with 50 µl/min flow rate. In terms of hydrogen utilization, this is a promising value. However, this is a near-dead-ended anode regime and the same consequences of DEA mode of operation may harm the MEA in a similar way. To evaluate the effect of long term ULF operation, a comparative study was performed. An 8.17 cm^2 of fresh MEA which was prepared using commercial GDLs and membrane and operated under flow through mode for 100 h, then ULF mode for 100 h and finally DEA mode for another 100 h. Then the CVs taken after each operation were recorded.

4.2.1 100 hours of Flow-through, Ultra-low Flow and Dead-ended Operation for MEA with Commercial Catalyst Support

For the FT mode, the RH was 100 %, the anode flow rate was 0.075 l/min, the cathode flow rate was 0.32 l/min, the temperature was 55 °C and the backpressure was 1.5 atm. The current density was held constant at 0.673 A/ cm^2.

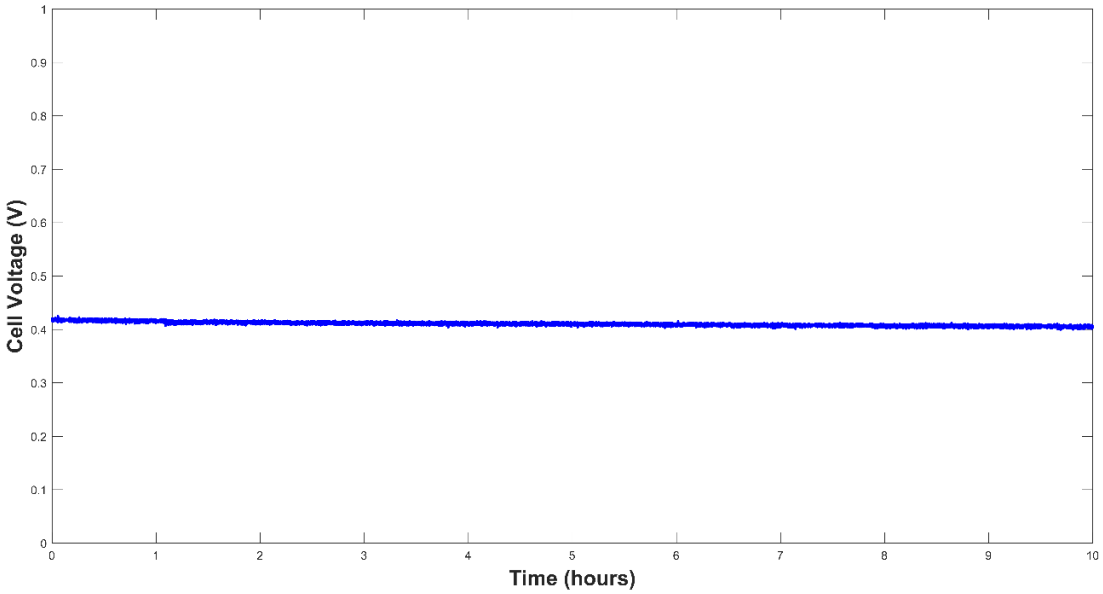

Figure 4.24: First 10 hours of the FT mode for the commercial 8.17 cm^2 MEA

For the ULF mode, the same parameters were used except for the anode RH, which was 25 %. The constant flow rate was 30 µl/min. The ultra-low flow was started after three hours which is why the voltage recovers in Figure 4.25.

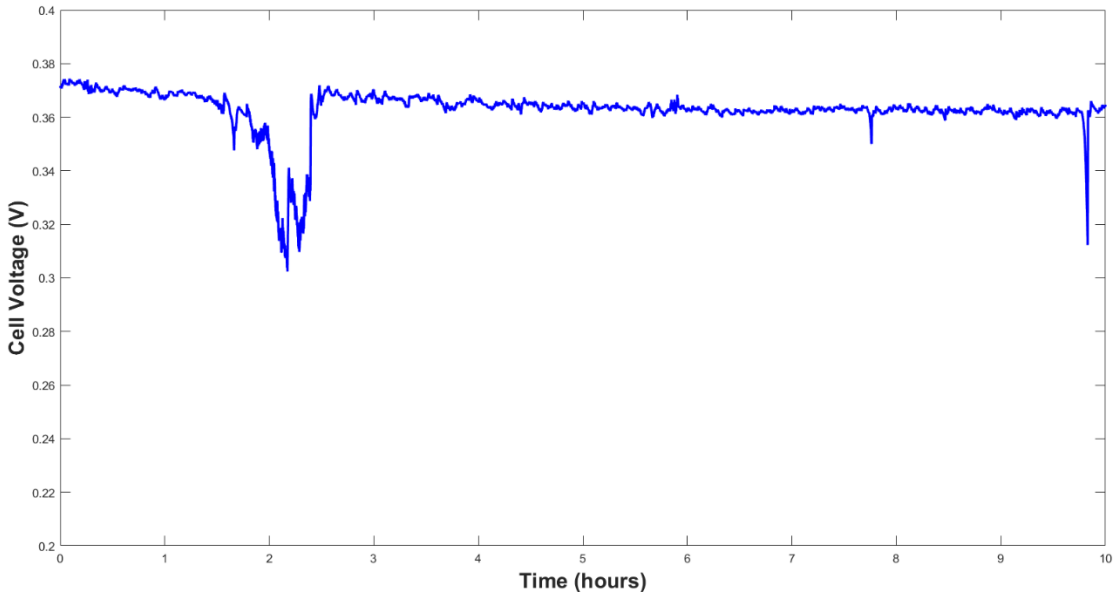

Figure 4.25: First 10 hours of the ULF mode for the commercial 8.17 cm^2 MEA

For the DEA mode, the same parameters with the ULF mode were used. The only difference was the absence of the constant flow. The purging of the anode was performed by

the Arduino controlled syringe pump. The pump was programmed to start when the voltage drops to 0.25 V and stop at 0.45 V.

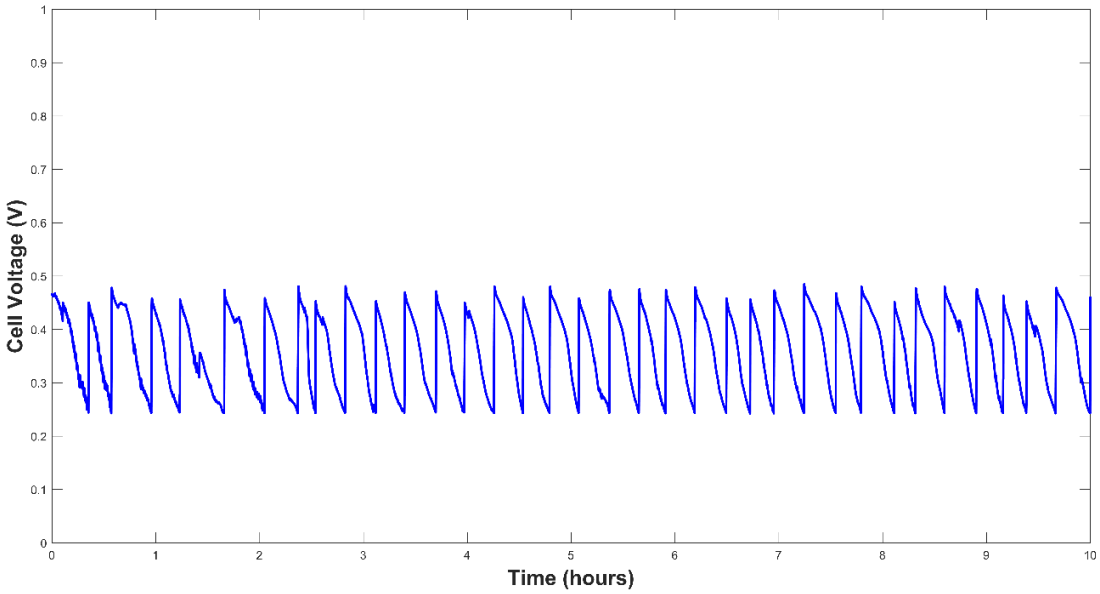

Figure 4.26: First 10 hours of the DEA mode for the 8.17 cm^2 MEA with commercial catalyst support

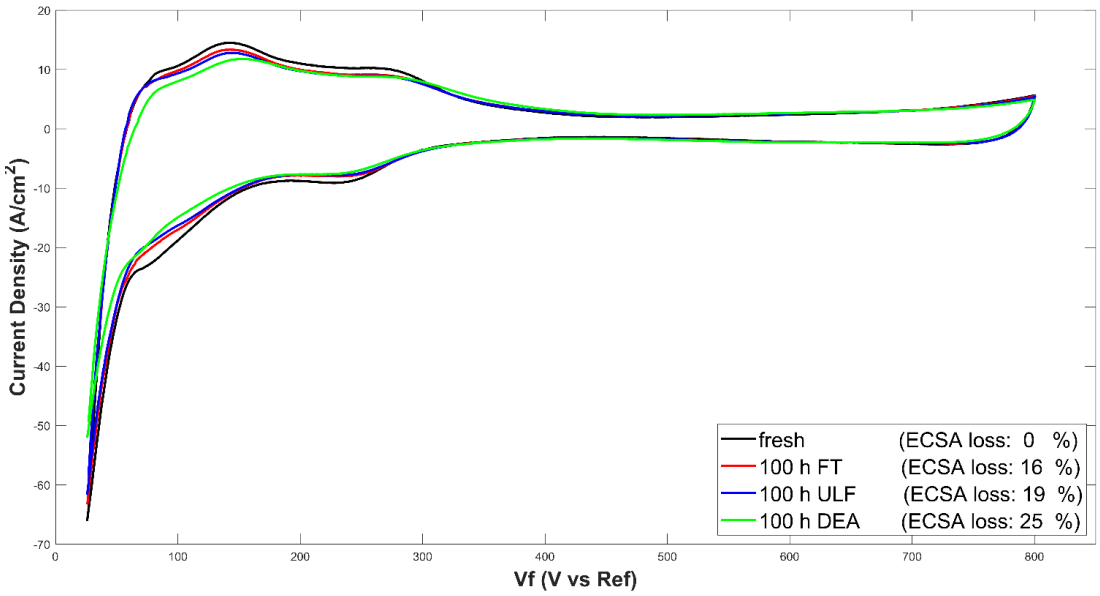

Figure 4.27: Cyclic voltammograms after 100 hours of FT, ULF and DEA operation for the 8.17 cm^2 MEA with commercial catalyst support

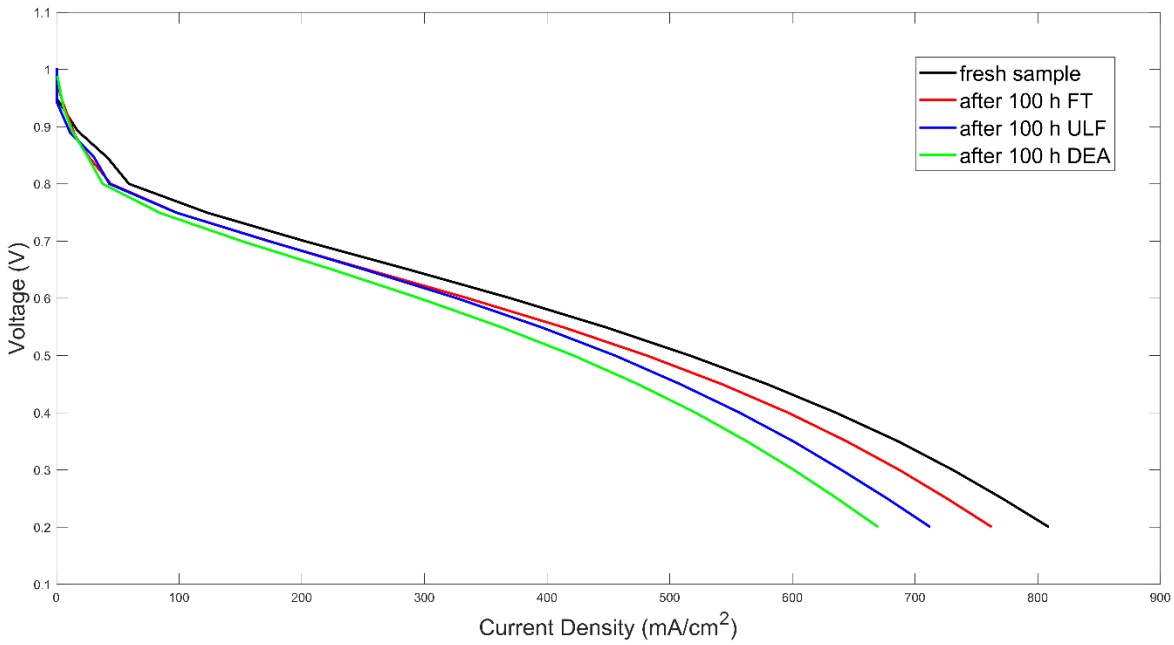

Figure 4.28: I-V curves taken after each modes of operation for the 8.17 cm^2 MEA with commercial catalyst support

As seen in Figure 4.27, ULF mode does not induce an ECSA loss as big as DEA mode. The I-V curves (Figure 4.28) taken after each 100 hours of operation also confirm the performance loss.

4.2.2 72 hours of Flow-through, Ultra-low Flow and Dead-ended Operation for MEA with Carbon Fiber Catalyst Support

The experiment was repeated with another type of MEA. This time, the carbon support is composed of carbon fibers and the Pt nanoparticles are buried onto these fibers. The networking between the Pt nanoparticles and the Nafion™ ionomer was low. As a result, a higher Pt loading (0.8 mg/cm^2) was used.

For the FT, ULF and DEA modes of operation, the same parameters as the previous experiment were employed. Due to the time constraint, the duration for each mode was limited to 72 hours.

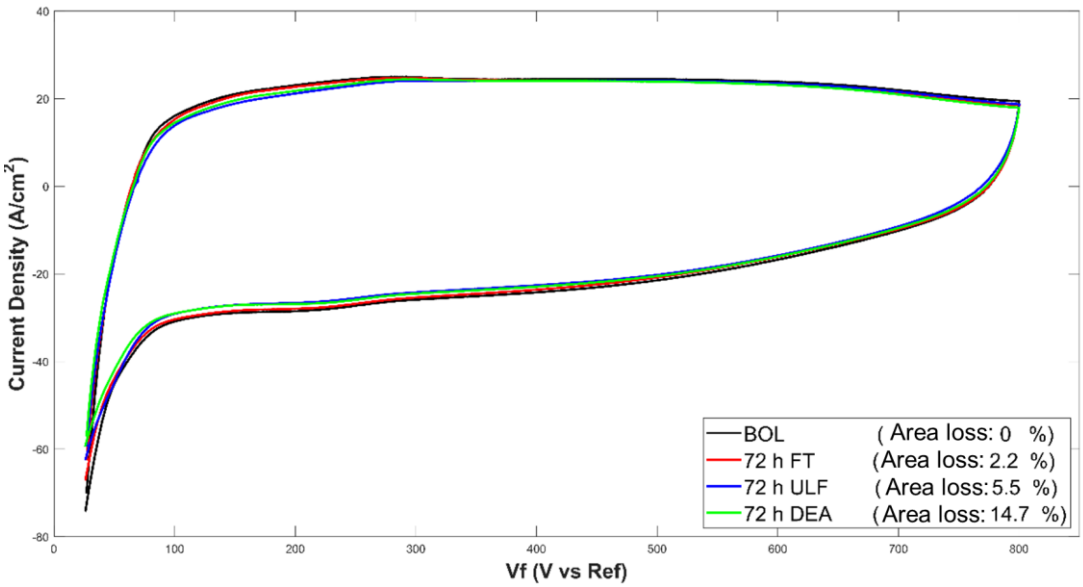

Figure 4.29: Cyclic voltammograms after 72 hours of FT, ULF and DEA operation for the 8.17 cm^2 MEA with carbon fiber carbon support

The cyclic voltammograms (Figure 4.29) look different from that of the MEA prepared with the commercial Vulcan carbon support. The structure is highly capacitive, and the hydrogen adsorption peaks are hidden in this capacitive behavior. Therefore the usual ECSA calculation was not possible for this sample. The areas between the 0 V and 0.4 V are calculated and the area losses are compared.

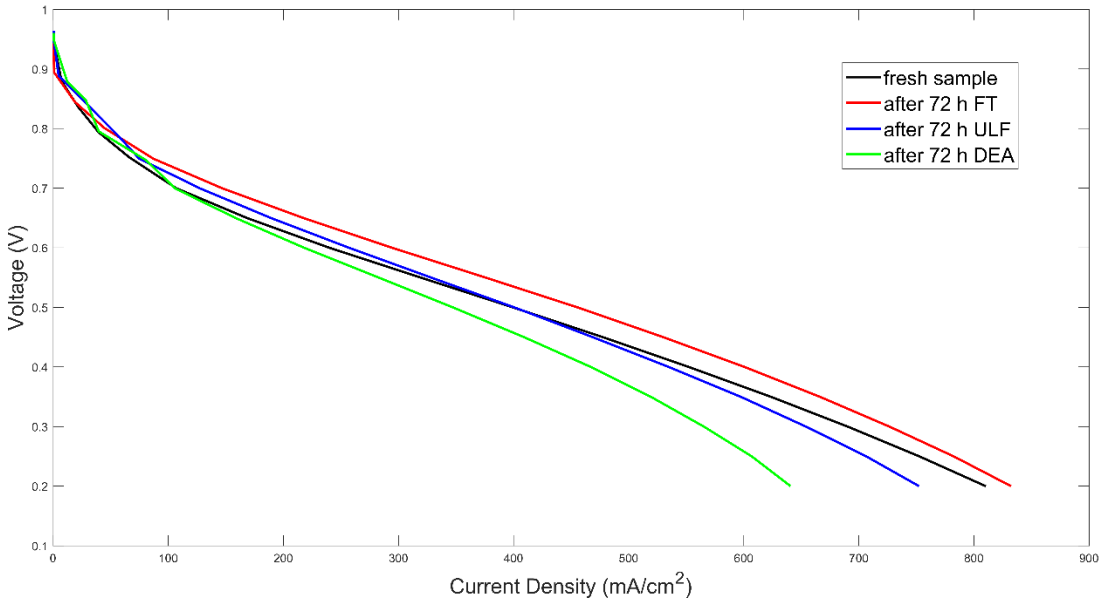

Figure 4.30: I-V curves taken after each modes of operation for the 8.17 cm^2 MEA with carbon fiber carbon support

In Figure 4.30, the I-V curve after 72 hours of operation is better than the beginning-of-life I-V curve. This might be because the conditioning was not finished before the operation.

4.2.3 Discussions

The effect of ULF vs DEA is more pronounced in the MEA with carbon fiber carbon support. The extra loss that was induced by the ULF mode is nearly the same as the FT mode. However, the DEA mode contributes almost 3 times more to the carbon corrosion. Another conclusion could be that the carbon fiber carbon support is more durable than the commercial supports against carbon corrosion.

The I-V curves also confirm the degradation, except for FT performance's being better than the fresh sample. It might be because of the insufficient purging performed before taking the I-V curve for the fresh MEA.

5 CONCLUSION

In the first part of this thesis, a new AST protocol was designed to promote a faster carbon corrosion in real operating conditions. The current ASTs that were recommended for fast carbon corrosion are either simulating a fuel starvation regime in the cathode by flowing nitrogen instead of air, or by building an artificial start up/shut down environment.

In the AST proposed in this thesis, the cell is forced to work at a continuous local fuel starvation mode. The anode exit is dead-ended with a connection to a high precision ultra-low flow control set up. This set up was developed by integrating an Arduino controller onto a high precision syringe pump which makes it possible to maintain flows as low as 10 µl/hour and can start/stop upon voltage feedback. The current drawn must be small enough to maintain a voltage around 0.7 V. When the ULF control set up is not working, the region close to the anode exit is accumulated with water and nitrogen, inducing a local fuel starvation in the cathode. This causes the cathodic potential to increase with respect to the electrolyte potential which is high enough to completely oxidize the Pt surface because Pt oxidizes at voltages above 0.98 V. When the voltage starts to decrease because of this nitrogen and water blanketing in the anode, the ULF set up is triggered to start at 0.7 V and withdraws with 50 µl/min until the voltage is recovered to 0.75 V. This enables the evacuation of the accumulated water and nitrogen. The cathodic potential decreases to the normal voltages which is 0.75 V. Due to the lower voltage, the PtO blanket on the Pt surface disappears. When water and nitrogen accumulate, the same process takes place again and again, causing the instantaneous restructuring of the Pt surface. This repeated reduction and oxidation of Pt nanoparticles, catalyzes the process of carbon corrosion.

Employing an ULF control set up is necessary. Because, if a regular purge was performed, the cell would not work at a continuous fuel starvation mode. The developed setup makes it possible to evacuate only the amount of water which is necessary to decrease the cathodic potential for a while and maintain a potential cycling between 0.7 V and a potential bigger than 1 V.

The ECSA and SEM data confirms the carbon corrosion. The SEM images showed that the MPL is also oxidized and delaminated from the GDL. This is probably due to using a catalyst coated GDL because the carbon support is closely in contact with the carbon of the MPL.

In the second part of the thesis, two different MEAs were used to evaluate and compare the degree of damage induced by ULF and DEA. The first MEA was composed of GDLs coated with commercial catalyst layer. The ECSA loss caused by the ULF mode was half of the DEA mode.

The second MEA employed a carbon fiber carbon support. The structure appears to be highly capacitive as seen in cyclic voltammograms. Looking at the area losses, the contribution of the ULF mode to the ECSA loss appears to be 3 times less than that of the DEA mode.

As a result, ultra-low-flow mode seems to be a promising operation mode for high hydrogen utilization and therefore high efficiency. New materials that are more durable to carbon corrosion may perform better and longer under this mode. To test the durability of these materials, the proposed AST test can be used to save time and money.

6 FUTURE WORK

The proposed AST will be performed on the mentioned carbon fiber carbon support MEA to evaluate the durability of this new material against carbon corrosion. The preliminary results suggest that due to the poor networking in the carbon fiber structure, the current collection is difficult which necessitates a higher Pt loading for good performance. However, the carbon fiber network might be more resistant to carbon corrosion as the ECSA results imply.

Another interesting experiment planned is the behavior of DEA under magnetic field. Nitrogen, water and hydrogen is diamagnetic, meaning that they will be repelled by a magnetic field. The oxygen is paramagnetic, and it will be attracted by the magnetic field. It might be possible to manipulate the diffusion pathways of nitrogen, water, oxygen and hydrogen such that the irreversible damages induced by the DEA mode can be mitigated and the performance might be improved.

7 APPENDIX

7.1 The program uploaded to the syringe pump

```
;       To generate pumping program file:
;       Select from the above menu:  File, Save As…
;       Select "Save as type" "Text (Tab Delimited) (*.txt)"
;       Select folder to save in, then name the file "nnnnn.PPL", where nnnn is a 8 character abbreviation for your project name
;       Answer YES/OK to any warnings.  Exit spreadsheet without re-saving.
;*****************************************************************



DIA28.9
VOL     ML
TRGFT
AL      0
PF      0
BP      0
;*****************************************************************
PHN     1                       ;       1               3
FUN     OUT     0


;*****************************************************************
PHN     2                       ;       2               3
FUN     EVN     5


;*****************************************************************
PHN     3                       ;       3               3
FUN     PAS     0


;*****************************************************************
PHN     4                       ;       4               3
FUN     JMP     3


;*****************************************************************
PHN     5                       ;       5               3
FUN     OUT     1


;*****************************************************************
PHN     6                       ;       6               3
FUN     EVN     1


;*****************************************************************
PHN     7                       ;       7               3
FUN     RAT
RAT     50      UM
VOL     0
DIR     WDR
;*****************************************************************
```

7.2 The program uploaded to the Arduino

main §

```
// Pins
const int eventPin = 12;  // -> Event Pin - TLL 4
const int analogPin = A0; // -> Analog Voltage Read
const int statePin = 11;  // -> Ouput Pin - TLL 5
// Variables
int analogValue = 0;
double voltage = 0.0f;
// STATE// 0 - Not working//1 - Working
bool state = false;
//Prototype Functions
void sendTrigger(void);
void setup() {
  Serial.begin(9600);
  pinMode(eventPin, OUTPUT);
  pinMode(statePin, INPUT);
  digitalWrite(eventPin, HIGH);
}
void loop() {
  analogValue = analogRead(analogPin);
  voltage = (analogValue*5.0f/1023.0f);
  Serial.println(voltage);
  state = digitalRead(statePin);
  // Run
  // (Voltage below 0.4V) and (pump is not running)
  if((voltage <= 0.4f) && (state == 0)){
    sendTrigger();
  }
  // Stop
  // (Voltage above 0.6V) and (pump is running)
  else if(voltage >= 0.6f && (state == 1)){
    sendTrigger();
  }
}
void sendTrigger(void){
  digitalWrite(eventPin, HIGH);
  delay(100);
  digitalWrite(eventPin, LOW);
  delay(100);
  digitalWrite(eventPin, HIGH);
}
```

8 REFERENCES

[1] C. E. Thomas, "Fuel cell and battery electric vehicles compared," *Int. J. Hydrogen Energy*, vol. 34, no. 15, pp. 6005–6020, 2009.

[2] T. Yoshida and K. Kojima, "Toyota MIRAI Fuel Cell Vehicle and Progress Toward a Future Hydrogen Society," *Interface magazine*, vol. 24, no. 2, pp. 45–49, 2015.

[3] F. Barbir, "PEM Fuel Cells," *Fuel Cell Technol.*, pp. 27–51, 2006.

[4] E. W. Washburn, Ed., *International Critical Tables of Numerical Data, Physics, Chemistry and Technology*, 1st Electr. New York, 2003.

[5] K. R. Cooper, V. Ramani, J. M. Fenton, and H. R. Kunz, *Experimental methods and data analyses for polymer electrolyte fuel cells*, 1.11. Southern Pines: Scribner Associates Inc., 2012.

[6] A. J. Bard and L. R. Faulkner, *Fundamentals and Fundamentals and Applications*, vol. 8, no. c. 2015.

[7] F. R. Castanheira, "Corrosion of high surface area carbon supports used in proton-exchange membrane fuel cell electrodes," 2014.

[8] W. Vielstich, *Handbook of Fuel Cells - Fundamentals, Technology and Applications*. 2010.

[9] J. Xie, K. L. More, T. A. Zawodzinski, and W. H. Smith, "Porosimetry of MEAs Made by 'Thin Film Decal' Method and Its Effect on Performance of PEFCs," *J. Electrochem. Soc.*, vol. 151, no. 11, p. A1841, 2004.

[10] R.-B. Lin and S.-M. Shih, "Kinetic analysis of the hydrogen oxidation reaction on Pt-black/Nafion electrode," *J. Solid State Electrochem.*, vol. 10, no. 4, pp. 243–249, 2006.

[11] H. W. X.-Z. Yu. H. Li, *PEM Fuel Cell Diagnostic Tools*. 2012.

[12] K. Cooper, "In Situ PEM Fuel Cell Electrochemical Surface Area and Catalyst Utilization Measurement," *Fuel Cell Magazine*, pp. 1–3, 2009.

[13] F. Gloaguen, J. M. Leger, and C. Lamy, "Electrocatalytic oxidation of methanol on platinum nanoparticles electrodeposited onto porous carbon substrates," *J. Appl. Electrochem.*, vol. 27, no. 9, pp. 1052–1060, 1997.

[14] R. Borup *et al.*, "Scientific aspects of polymer electrolyte fuel cell durability and degradation," *Chem. Rev.*, vol. 107, no. 10, pp. 3904–3951, 2007.

[15] A. Collier, H. Wang, X. Zi Yuan, J. Zhang, and D. P. Wilkinson, "Degradation of polymer electrolyte membranes," *Int. J. Hydrogen Energy*, vol. 31, no. 13, pp. 1838–1854, 2006.

[16] Y. Tang, M. H. Santare, A. M. Karlsson, S. Cleghorn, and W. B. Johnson, "Stresses in Proton Exchange Membranes Due to Hygro-Thermal Loading," *J. Fuel Cell Sci. Technol.*, vol. 3, no. 2, p. 119, 2006.

[17] F. A. De Bruijn, V. A. T. Dam, and G. J. M. Janssen, “Review: Durability and degradation issues of PEM fuel cell components,” *Fuel Cells*, vol. 8, no. 1, pp. 3–22, 2008.

[18] X. Erler, “In-situ investigation of metal nanoparticle stability during electrocatalysis,” 2012.

[19] Y. Shao-Horn, W. C. Sheng, S. Chen, P. J. Ferreira, E. F. Holby, and D. Morgan, “Instability of supported platinum nanoparticles in low-temperature fuel cells,” *Top. Catal.*, vol. 46, no. 3–4, pp. 285–305, 2007.

[20] V. A. T. Dam and F. A. de Bruijn, “The Stability of PEMFC Electrodes,” *J. Electrochem. Soc.*, vol. 154, no. 5, p. B494, 2007.

[21] E. Guilminot, A. Corcella, F. Charlot, F. Maillard, and M. Chatenet, “Detection of Ptz+ Ions and Pt Nanoparticles Inside the Membrane of a Used PEMFC,” *J. Electrochem. Soc.*, vol. 154, no. 1, p. B96, 2007.

[22] K. Kinoshita and J. Bett, “Electrochemical oxidation of carbon black in concentrated phosphoric acid at 135°C,” *Carbon*, vol. 11, no. 3. pp. 237–247, 1973.

[23] K. H. Kangasniemi, D. A. Condit, and T. D. Jarvi, “Characterization of Vulcan Electrochemically Oxidized under Simulated PEM Fuel Cell Conditions,” *J. Electrochem. Soc.*, vol. 151, no. 4, p. E125, 2004.

[24] L. M. Roen, C. H. Paik, and T. D. Jarvi, “Electrocatalytic Corrosion of Carbon Support in PEMFC Cathodes,” *Electrochem. Solid-State Lett.*, vol. 7, no. 1, p. A19, 2004.

[25] J. Willsau and J. Heitbaum, “The influence of Pt-activation on the corrosion of carbon in gas diffusion electrodes-A dems study,” *J. Electroanal. Chem.*, vol. 161, no. 1, pp. 93–101, 1984.

[26] S. Maass, F. Finsterwalder, G. Frank, R. Hartmann, and C. Merten, “Carbon support oxidation in PEM fuel cell cathodes,” *J. Power Sources*, vol. 176, no. 2, pp. 444–451, 2008.

[27] W. Li and A. M. Lane, “Investigation of Pt catalytic effects on carbon support corrosion of the cathode catalyst in PEM fuel cells using DEMS spectra,” *Electrochem. commun.*, vol. 11, no. 6, pp. 1187–1190, 2009.

[28] F. Maillard, A. Bonnefont, and F. Micoud, “An EC-FTIR study on the catalytic role of Pt in carbon corrosion,” *Electrochem. commun.*, vol. 13, no. 10, pp. 1109–1111, 2011.

[29] S. C. Ball, S. L. Hudson, B. Theobald, and D. Thompsett, “The Effect of Dynamic and Steady State Voltage Excursions on the Stability of Carbon Supported Pt and PtCo Catalysts,” *ECS Trans.*, vol. 3, no. 1, pp. 595–605, 2006.

[30] W. R. Baumgartner, P. Parz, S. D. Fraser, E. Wallnöfer, and V. Hacker, “Polarization study of a PEMFC with four reference electrodes at hydrogen starvation conditions,” *J. Power Sources*, vol. 182, no. 2, pp. 413–421, 2008.

[31] C. A. Reiser *et al.*, "A Reverse-Current Decay Mechanism for Fuel Cells," *Electrochem. Solid-State Lett.*, vol. 8, no. 6, p. A273, 2005.

[32] N. Yousfi-Steiner, P. Moçotéguy, D. Candusso, and D. Hissel, "A review on polymer electrolyte membrane fuel cell catalyst degradation and starvation issues: Causes, consequences and diagnostic for mitigation," *J. Power Sources*, vol. 194, no. 1, pp. 130–145, 2009.

[33] S. Abbou, J. Dillet, G. Maranzana, S. Didierjean, and O. Lottin, "Local potential evolutions during proton exchange membrane fuel cell operation with dead-ended anode – Part I: Impact of water diffusion and nitrogen crossover," *J. Power Sources*, vol. 340, pp. 337–346, 2017.

[34] D. A. Stevens, M. T. Hicks, G. M. Haugen, and J. R. Dahn, "Ex Situ and In Situ Stability Studies of PEMFC Catalysts," *J. Electrochem. Soc.*, vol. 152, no. 12, p. A2309, 2005.

[35] M. Cai, M. S. Ruthkosky, B. Merzougui, S. Swathirajan, M. P. Balogh, and S. H. Oh, "Investigation of thermal and electrochemical degradation of fuel cell catalysts," *J. Power Sources*, vol. 160, no. 2 SPEC. ISS., pp. 977–986, 2006.

[36] Q. Yan, H. Toghiani, Y. W. Lee, K. Liang, and H. Causey, "Effect of sub-freezing temperatures on a PEM fuel cell performance, startup and fuel cell components," *J. Power Sources*, vol. 160, no. 2 SPEC. ISS., pp. 1242–1250, 2006.

[37] J. Hou *et al.*, "Analysis of PEMFC freeze degradation at -20 °C after gas purging," *J. Power Sources*, vol. 162, no. 1, pp. 513–520, 2006.

[38] N. Garland, T. Benjamin, and J. Kopasz, "DOE Fuel Cell Program: Durability Technical Targets and Testing Protocols," *ECS Trans.*, vol. 11, no. 1, pp. 923–931, 2007.

[39] D. A. Ohma Atsushi, Shinohara Kazuhiko, Iiyama Akihiro, Yoshida Toshihiko, "Membrane and Catalyst Performance Targets for Automotive Fuel Cells by FCCJ Membrane, Catalyst, MEA WG," *ECS Trans.*, vol. 41, no. 1, pp. 775–784, 2011.

[40] X. Z. Yuan, H. Li, S. Zhang, J. Martin, and H. Wang, "A review of polymer electrolyte membrane fuel cell durability test protocols," *J. Power Sources*, vol. 196, no. 22, pp. 9107–9116, 2011.

[41] The United States Council for Automotive Research, "USCAR Fuel cell tech team cell component accelerated stress test protocols - Revised May 26, 2010," 2010.

[42] S. Kundu, L. C. Simon, and M. W. Fowler, "Comparison of two accelerated Nafion degradation experiments," *Polymer Degradation and Stability*, vol. 93, no. 1. pp. 214–224, 2008.

[43] M. F. Mathias *et al.*, "Two Fuel Cell Cars in Every Garage?," *The Electrochemical Society Interface*, vol. 14. pp. 24–35, 2005.

[44] M. T. Huang Xinyu, Solasi Roham, Zou Yue, Feshler Matthew, Reifsnider Kenneth, Condit David, Burlatsky Sergei, "Mechanical Endurance of Polymer

ElectrolyteMembrane and PEMFuel Cell Durability," *J. Polym. Sci. Part B Polym. Phys.*, vol. 44, pp. 2346–2357, 2006.

[45] M. Inaba, T. Kinumoto, M. Kiriake, R. Umebayashi, A. Tasaka, and Z. Ogumi, "Gas crossover and membrane degradation in polymer electrolyte fuel cells," *Electrochim. Acta*, vol. 51, no. 26, pp. 5746–5753, 2006.

[46] Y. Jeon, S. M. Juon, H. Hwang, J. Park, and Y. G. Shul, "Accelerated life-time tests including different load cycling protocols for high temperature polymer electrolyte membrane fuel cells," *Electrochim. Acta*, vol. 148, pp. 15–25, 2014.

[47] R. Petrone, D. Hissel, M. C. Péra, D. Chamagne, and R. Gouriveau, "Accelerated stress test procedures for PEM fuel cells under actual load constraints: State-of-art and proposals," *Int. J. Hydrogen Energy*, vol. 40, no. 36, pp. 12489–12505, 2015.

[48] de B. F. A. Dam V. A. T., "The Stability of PEMFC Electrodes Platinum Dissolution vs Potential and Temperature Investigated by Quartz Crystal Microbalance," *J. Electrochem. Soc.*, vol. 154, no. 5, pp. B494–B499, 2007.

[49] S. P. Shao Yuyan, Yin Geping, Gao Yunzhi, "Durability Study of Pt/C and Pt/CNTs Catalysts under Simulated PEM Fuel Cell Conditions," *J. Electrochem. Soc.*, vol. 153, no. 6, pp. A1093–A1097, 2006.

[50] R. L. Borup, J. R. Davey, F. H. Garzon, D. L. Wood, and M. A. Inbody, "PEM fuel cell electrocatalyst durability measurements," *Journal of Power Sources*, vol. 163, no. 1 SPEC. ISS. pp. 76–81, 2006.

[51] R. Makharia *et al.*, "Durable PEM Fuel Cell Electrode Materials: Requirements and Benchmarking Methodologies," in *ECS Transactions*, 2006, vol. 1, no. 8, pp. 3–18.

[52] D. A. Stevens and J. R. Dahn, "Thermal degradation of the support in carbon-supported platinum electrocatalysts for PEM fuel cells," *Carbon N. Y.*, vol. 43, no. 1, pp. 179–188, 2005.

[53] P. T. Yu, W. Gu, R. Makharia, F. T. Wagner, and H. A. Gasteiger, "The Impact of Carbon Stability on PEM Fuel Cell Startup and Shutdown Voltage Degradation," *ECS Trans.*, vol. 3, no. 1, pp. 797–809, 2006.

[54] U.S. DRIVE Fuel Cell Tech Team, "Cell Component Accelerated Stress Test and Polarization Curve Protocols for PEM Fuel Cells," 2013.

[55] N. Macauley *et al.*, "Carbon Corrosion in PEM Fuel Cells and the Development of Accelerated Stress Tests," *J. Electrochem. Soc.*, vol. 165, no. 6, pp. F3148–F3160, 2018.

[56] W. Wagner, H.-J. Kretzschmar, and W. Wagner, *International steam tables : properties of water and steam based on the industrial formulation IAPWS-IF97*. Springer, 2008.

[57] M. Brodt, R. Wycisk, and P. N. Pintauro, "Nanofiber Electrodes with Low Platinum Loading for High Power Hydrogen/Air PEM Fuel Cells," *J. Electrochem. Soc.*, vol. 160, no. 8, pp. F744–F749, 2013.

[58] E. M. Niroumand Amir, Olfert Mark, “Hydrogen Crossover Leak Rate.”

[59] K. R. Cooper, “In Situ PEMFC Fuel Crossover & Electrical Short Circuit Measurement,” *Fuel Cell Mag.*, vol. Aug/Sep, pp. 1–2, 2008.

[60] H. Wang, X. Yuan, and H. Li, *PEM Fuel Cell Diagnostic*. 2012.

[61] M. Zhiani and S. Majidi, “Effect of MEA conditioning on PEMFC performance and EIS response under steady state condition,” *Int. J. Hydrogen Energy*, vol. 38, no. 23, pp. 9819–9825, 2013.